THE UNIVERSITY OF CALGARY

Analysis and filtering of near-surface effects in land multicomponent seismic data

by

Saul Ernesto Guevara

A THESIS

SUBMITTED TO THE FACULTY OF GRADUATE STUDIES

IN PARTIAL FULFILLMENT OF THE REQUIREMENTS FOR THE

DEGREE OF MASTER OF SCIENCE

DEPARTMENT OF GEOLOGY AND GEOPHYSICS

CALGARY, ALBERTA

NOVEMBER, 2000

ABSTRACT

Multicomponent seismic data recorded on the earth's surface provide geologic information useful for natural resource exploration. However, this information is usually altered by propagation through the near-surface layers. In this thesis, effects of the near-surface layer in multicomponent data are investigated and methods to overcome them are studied. The main effects studied are the free-surface effect, mode-leakage, ray bending, polarization change and statics.

Ray tracing and finite-difference modeling were conducted on basic geologic models and polarization analysis is applied to the results. From this analysis, the free-surface effect appears to have a larger effect at longer offsets, high dips and very high near-surface V_P/V_S values. Polarization analysis is also carried out on real data obtained from the Blackfoot oil field, Alberta. Horizontally polarized events generated in the near-surface layer are identified. Their polarization direction corresponds well to the actual shot-receiver geometry and, hence, can be used to improve geophone orientation. A method to separate *P*-*P* and *P*-*S* wave modes taking into account *P*- and *S*- wave statics is tested, resulting in improved seismic sections from the Blackfoot survey.

ACKNOWLEDGEMENTS

I am thankful and indebted to many people and institutions, which have made possible this thesis and my graduate studies, even if I do not mention all of them here.

Dr. Ariel Solano and Geol. Kurt Bayer, from Ecopetrol (Colombia), encouraged me to pursue graduate studies, and throughout these studies I received the valuable institutional and financial support of Ecopetrol.

My supervisor, Dr. Robert R. Stewart, simultaneously encouraged, challenged and guided me, greatly enhancing the results presented here. Dr. Peter W. Cary, who was my advisor on chapter five, gave me access to his valuable experience and knowledge. Dr. Gary Margrave and Dr. Edward Krebes, from the Geology and Geophysics Department, furnished me with insights into the meanings of important seismological concepts.

The CREWES personnel provided expert support, especially Hanxing Lu on processing and seismic data handling, and Henry Bland, who besides computer assistance gave me important geophysical suggestions. Special thanks to Louise Forgues, for all her administrative support, and her ability to help in critical moments. Also I had valuable editing assistance from many people, including Emily Cargan and Dr. Len Hills. The CREWES sponsors and the Department of Geology and Geophysics also provided me with financial support during the last part of my studies.

Besides that, I counted on the friendship, support and criticism of my partners at the Geophysics Laboratory of Ecopetrol-ICP, and also of the friends I found in Calgary, such as Carlos Rodriguez, Chanpen Silawongsawat, Graziella Kirtland Grech, and Xinxiang Li.

The quiet support of my wife, Maria Clemencia, and my son, Lino Julian, encouraged me to surmount the more arduous obstacles. I hope to reward them for their patience and compensate for the family time we lost.

DEDICATION

To my father. Saúl Guevara J.. and my mother. Blanca Ochoa de Guevara.

who taught me the fundamental principles.

TABLE OF CONTENTS

Approval page ii
Abstract iii
Acknowledgements iv
Dedication v
Table of Contents vi
List of Tables viii
List of Figures ix

CHAPTER ONE: INTRODUCTION 1
1.1. Overview 1
1.2. Background 3
1.2.1. On elastic waves 3
1.2.2. Anisotropy and anelasticity 5
1.2.3. Multicomponent seismic exploration 6
1.2.4. Converted wave summary 8
1.3. Near surface effects on multicomponent data 9
1.3.1. Characteristics of the NSL 9
1.3.2. A velocity model for the NSL 10
1.3.3. The free surface effect 12
1.3.4. Wavelength and the NSL 14
1.3.5. Statics correction 15
1.3.6. NSL effects summary 15
1.4. Scope of the thesis 16
1.5. Methodology 17
1.6. Software tools 18

CHAPTER TWO: SYNTHETIC DATA ANALYSIS 19
2.1. Introduction 19
2.2. Finite Difference modeling 19
2.3. Ray tracing modeling 22
2.4. Geological Models analysis 22
2.4.1. Model 1: Horizontal reflector 23
2.4.2. Model 2: NSL 32
2.4.3. Model 3: High velocity NSL 39
2.4.4. Model 4: Dipping reflector 43
2.4.5. Model 5: Dipping reflector and NSL 47
2.5. Some conclusions 51

CHAPTER THREE: POLARIZATION ANALYSIS APPLIED 54
3.1. Introduction 54
3.2. Wave polarization and the seismic method 54
3.3. Overview of polarization analysis techniques 56
3.4. Methods applied 57
3.4.1. Hodograms 58
3.4.2. Histogram algorithm 59
3.4.3. Covariance matrix algorithm 59
3.5. Polarization analysis on windows of events 61
3.5.1. Synthetic data 62
3.5.2. Real data 68
3.6. Polarization analysis and filtering of shot gathers 73
3.7. Conclusions 79

CHAPTER FOUR: GEOPHONE ORIENTATION VIA POLARIZATION ANALYSIS 80
4.1. Introduction 80
4.2. Method 82
4.3. Polarization and geophone orientation in Blackfoot III 82
4.3.1. Description 83
4.3.2. Results 90
4.4. Discussion and conclusions 93

CHAPTER FIVE: MODE SEPARATION AND STATICS 95
5.1. Introduction 95
5.2. Theory 96
5.3. Application to synthetic data 101
5.4. Application to real data 106
5.4.1. The real data set 106
5.4.2. Application to prestack data 110
5.4.3. Application to poststack data 114
5.5. Discussion and Conclusion 117

CHAPTER SIX: SUMMARY AND FUTURE WORK 119

REFERENCES 123

APPENDIX A: ELASTIC WAVES OVERVIEW AND NOMENCLATURE 128
APPENDIX B: MATHEMATICAL ASPECTS OF POLARIZATION 133
APPENDIX C: THE FREE SURFACE EFFECT 138

LIST OF TABLES

Table 4.1. Azimuths according to the acquisition geometry in Blackfoot III data 84
Table 4.2. Azimuth Source-Receiver versus polarization angle 90
Table C.1. Angles of propagation direction and particles displacement 140

LIST OF FIGURES

Figure 1.1. Schematic diagram of the two multicomponent seismic methods on land..... 6
Figure 1.2. Top view and polarity of the elements of a Cartesian 3-C geophone..... 8
Figure 1.3. Schematic diagram of some near-surface layer effects in elastic wave propagation..... 11
Figure 1.4. Two examples of the free surface response as a function of the angle of incidence and the Vp/Vs ratio. 13
Figure 1.5. Examples of the free-surface effect on surface particle motion for an incident *S* wave..... 14
Figure 2.1. Ricker wavelet source used in FD modeling. 21
Figure 2.2. Model 1: a single reflector. 23
Figure 2.3. Model 1 components from FD modeling. 26
Figure 2.4. Model 1: Snapshots of the two components. 27
Figure 2.5. Model 1 components from ray tracing modeling..... 28
Figure 2.6. Reflection coefficients and phase rotation at the reflector of Model 1..... 30
Figure 2.7. Angle of Incidence to the reflector as a function of offset in Model 1. 31
Figure 2.8. Amplitude of PS and SP wave modes 31
Figure 2.9. Model 2: single reflector and complex near-surface layer. 32
Figure 2.10. Model 2 components from FD modeling. 34
Figure 2.11. Snapshots of Model 2 35
Figure 2.12. Model 2 ray tracing components separated in *P* and *S* wave modes 36
Figure 2.13. Model 2: analysis of PS mode angle of incidence and amplitude 38
Figure 2.14. Model 3: high-velocity near-surface layer..... 39
Figure 2.15. Model 3 vertical and horizontal components from FD modeling..... 41
Figure 2.16. Model 3 ray tracing components separated in *P* and *S* wave modes 42
Figure 2.17. Model 3:angle of incidence to the surface of PS mode 43
Figure 2.18. Model 4: dipping reflector without NSL 44
Figure 2.19. Model 4 vertical and horizontal components from FD modeling..... 45
Figure 2.20. Model 4 ray tracing components separated in *P* and *S* wave modes 46
Figure 2.21. Model 5: dipping reflector with NSL 47

Figure 2.22. Model 5 vertical and horizontal components from FD modeling 49
Figure 2.23. Model 5 ray tracing components separated in *P* and *S* wave modes 50
Figure 2.24. Angle of incidence of PS wave on dipping layers 51
Figure 3.1. Hodograms and the histogram method to analyse polarization 58
Figure 3.2. Model 1 synthetic data with the polarisation analysis windows 62
Figure 3.3. Polarization analysis of Model 1 window 1 64
Figure 3.4. Polarization analysis of Model 1window 2. 65
Figure 3.5. Polarization analysis of Model 1 window 3 66
Figure 3.6. Polarizacion analysis of converted waves. Model 2 67
Figure 3.7. Real data components with the polarisation analysis windows 69
Figure 3.8. Polarization analysis of real data window 1. 71
Figure 3.9. Polarization analysis of real data window 2 72
Figure 3.10. Polarization analysis of real data window 3 73
Figure 3.11. Polarization analysis of the complete synthetic gather 75
Figure 3.12. Polarization analysis of the complete real gather 76
Figure 3.13. Polarization filtering of *PP* reflection from Model 1 77
Figure 3.14. Polarization filtering of event2. real data 78
Figure 3.15. Polarization filtering of event 3. real data 78
Figure 4.1. Schema of the relation between polarization and source-receiver direction .. 81
Figure 4.2. Field layout of the Blackfoot III data used in the test 83
Figure 4.3. Data components from Blackfoot III used in the test 85
Figure 4.4. Event 1 polarization analysis 86
Figure 4.5. Event 2 polarization analysis 87
Figure 4.6. Event 3 polarization analysis 88
Figure 4.7. Event 4 polarization analysis 89
Figure 4.8. Event 3 polarization analysis covariance matrix method 91
Figure 4.9. Event 2 polarization covariance matrix method 92
Figure 4.10. Event 4 polarization analysis covariance matrix method 92
Figure 4.11. Event 4 analysis using the covariance matrix method 92
Figure 5.1. Flow chart of the method for mode separation in the presence of statics..... 100

Figure 5.2. Synthetic data used to test the method with seismic events 101
Figure 5.3. First test synthetic data: simple trace shifting statics..... 103
Figure 5.4. First synthetic data test result..... 104
Figure 5.5. Second test synthetic data: random statics applied..... 105
Figure 5.6. Second synthetic data test result..... 106
Figure 5.7. Raw data from Blackfoot III used to test..... 107
Figure 5.8. Near surface velocities V_P and V_S in the Blackfoot III survey..... 109
Figure 5.9. Incidence angle of two real-data events as a function of the offset..... 110
Figure 5.10. Spectral analysis of an event in the radial-component 112
Figure 5.11. Real-data shot-gather after mode separation method applied..... 113
Figure 5.12. Real-data shot-gather after method applied without mode separation 114
Figure 5.13. Processing sequence for *PS* – wave..... 115
Figure 5.14. Comparison of *PS*- stacked sections after application of the method..... 116
Figure 5.15. Close-up of the *PS* stacked sections comparison..... 117
Figure A.1. The plane wave approximation..... 131
Figure B.1. Polarization ellipse..... 134
Figure B.2. Phase differences and ellipticity..... 134
Figure C.1. Incidence of P and S waves to the free surface..... 139
Figure C.2. Free surface displacement and incidence vectors 141

CHAPTER 1

INTRODUCTION

1.1. Overview

The seismic exploration method uses propagation of elastic energy to obtain information about the geologic characteristics inside the earth. This method is a well-proven tool in the exploration for natural resources, largely hydrocarbons, since the early years of the 20^{th} century.

Surface-recorded seismic reflection data is the chief seismic exploration method. This time-honoured practice, named the *conventional method* in this thesis, uses seismic sensors or *geophones* to record *compressional* or *P* waves reflected from the deep layers. To that end, one-component geophones are deployed with vertical orientation on the land surface, and, in an analogous manner, hydrophones are towed just under marine surface. In that way, compressional waves with encoded geologic information are detected as vertical vibrations on land and pressure changes in the sea. With the conventional seismic method, geological features of many places have been successfully mapped. This method has been strengthened more recently by three-dimensional (3D) seismic technology, where measurements are taken across an area of the surface.

The *multicomponent seismic method* uses sensors that can detect all the directions of the wave vibration. The detectors on land are usually *three-component* (*3-C*) geophones. In principle, with this method it is possible to record the complete wavefield, including the *shear* or *S* waves and the particle displacement or *polarization* of the wave modes. The recorded *S*-wave characteristics can be correlated with rock properties e.g. lithology, fluid content and anisotropy and consequently contribute to the improved knowledge of the geology (Tatham and McCormack, 1991).

However, the results obtained on land with the multicomponent seismic method are frequently compromised by the near-surface layer (NSL). This shortcoming of the land-surface multicomponent method can be noted when the resulting data are compared with

multicomponent marine or borehole (*VSP* or *Vertical Seismic Profiling*) data, which are less affected by the near surface. More investigation in this direction is needed to overcome these surface effects.

In this thesis, some characteristics of the free-surface and near-surface effects on land multicomponent data are analyzed and methods to handle them are tested. Factors such as the water table effect, the dissimilar behaviour of *P* and *S* waves in the NSL, the free-surface effect on body wave propagation, and statics correction are examined. Seismic modelling is used to help understand the image of deeper reflectors carried by the waves to the surface. Polarization methods and a method to separate wave modes in the presence of statics are tested on synthetic and real data. Practical issues considered are acquisition procedures, mode filtering, and statics.

In Chapter 1 theoretical concepts about elastic-wave propagation are introduced, multicomponent seismic exploration and the effects of the near-surface layer in land data. In the second chapter numerical modelling of wave propagation is applied to analyze near-surface effects on simplified geological models. In the third chapter, polarization analysis methods are presented and applied to synthetic seismograms of typical geologic models and real multi-component seismic data. In Chapter 4, orientation of geophones using polarization is studied in real data. In Chapter 5, wave modes are separated using an algorithm that employs the free-surface response and takes into account the *P*- and *S*-wave statics. Final remarks and ideas about future work follow in Chapter 6. For the sake of completeness, appendices set out the theoretical basis, emphasizing the physical meaning instead of being mathematically rigorous.

This chapter states the general framework of the thesis. In the following, there is an overview of the theoretical basis and the multicomponent method. After that, the near-surface characteristics and their effects on multicomponent data are considered. Finally, general aspects of the thesis such as the scope and the analysis methods used are presented.

1.2. Background

1.2.1. On elastic waves

The basic framework of this thesis is the theory of elastic wave propagation through isotropic homogeneous media on land. This is a highly developed theory, from which some relevant aspects are introduced in the next section. More details and nomenclature definitions are in Appendix A, as are primary references.

An elastic material deforms under the action of an external force and, once the load is removed, recovers its original shape, which generates a disturbance that propagates throughout the medium. This recovery is the origin of *elastic waves*. Wave propagation is described mathematically by the *wave equation* and depends on the properties of the medium, described by the *elastic constants* (Appendix A). Assuming a *homogeneous* and *isotropic medium*, there are two elastic constants, which can be expressed in many ways. Perhaps the most common expression, are the parameters μ and λ (*Lamé parameters*). Equivalently, μ and k can be used, where μ is the *shear modulus* or *rigidity*, and k is the *incompressibility modulus*.

From the wave equation for an isotropic homogeneous material two wave modes propagate through an unbounded medium: the *primary* or *P*-wave (compressional wave) and the *secondary* or *S*-wave (shear wave). Their respective velocities (using the elastic constants μ and k for reason of their physical meaning) are

$$P\text{-wave velocity} \equiv V_P = \sqrt{\frac{k + 4\mu/3}{\rho}} \qquad (1.1)$$

and

$$S\text{- wave velocity} \equiv V_S = \sqrt{\frac{\mu}{\rho}} \,. \qquad (1.2)$$

where ρ is the mass density.

Some remarks about these wave modes are:

* *S* waves do not propagate in fluids, since fluids are not resistant to change in shape (their rigidity μ is zero).

* The V_P/V_S value has a lithological meaning, since even though many types of rock can have a similar *P* or *S* wave velocity, they do not commonly have the same *Vp/Vs* ratio.

* A frequently used elastic parameter in relation to rock properties is *Poisson's ratio*, σ, which is the relation between transverse and longitudinal deformations. Poisson's ratio can be expressed as a monotonically increasing function of the V_P/V_S ratio.

The *P* and *S* modes travel through the medium and usually are referred to as *body waves*. These wave modes eventually carry information from deeper layers to the surface. Other basic wave modes are the *surface* or *Rayleigh waves*, known as *ground-roll* in seismic exploration, which are generated at or near to the free-surface. At the receivers, surface waves usually interfere with the body waves carrying information from deeper layers.

A property of elastic waves is the motion of the particles of the medium or *polarization* (Sheriff, 1991), which can be registered with the multicomponent method. Polarization is characterized by direction and shape. In a homogeneous, isotropic medium, *P*-wave polarization shape is linear and direction is in-line with the direction of wave propagation. *S*-wave polarization is linear and perpendicular to the wave propagation direction. Rayleigh-wave polarization is elliptical, with retrograde movement and its major axis is perpendicular to the wave propagation direction.

Two types of *S* waves are defined according to the relation between the direction of polarization and the plane of propagation: the Vertical *S* wave (*SV*), and the Horizontal *S* wave (*SH*). The *SV* polarization is in the plane of trajectory and the *SH* polarization is perpendicular to the plane of trajectory (see Figure 1.1). With non-vertical incidence to a plane horizontal seismic reflector, *SV* waves are generated by *P* waves and viceversa, and the waves generated by this way are known as *converted waves*. In this case, *P* and *SV* waves are a coupled pair, and *SH* waves are independent from them. Figure 1.1 illustrates wave modes and coupling in an isotropic homogeneous medium with parallel layers (Tatham and McCormack, 1991).

1.2.2. Anisotropy and anelasticity

The homogeneous and isotropic elastic model has been essential to describe wave propagation in the earth. However it has proved insufficient in some real cases. Wave behaviour at some locations can be better explained using *anisotropic theory* or *anelastic theory*.

In the anisotropic model, the elastic properties change according to the direction: this model is more appropriate, for example, to describe fractured rocks and layering. Attenuation, explained by the anelastic model, is related to loss of energy, first in the high frequency components, and eventually causing the complete wave to vanish. Attenuation effect is higher in less-consolidated materials. However all the real media are, at least somewhat, anelastic. Cieslewicz (1999) analyze attenuation in the near-surface layer, using real data experiments.

In both models, anisotropic and anelastic, polarization is different with respect to the isotropic model: from anisotropy the direction of polarization can change, and from anelasticity can change the shape (Tatham and McCormack, 1991; Buchen, 1971). These two theoretical models, especially anisotropy, are currently of interest in relation to multicomponent wave technology; however, as a first approximation, they are not of concern in this thesis. Attenuation is not critical for the test carried out and the isotropic model should be required for more complicate future developments or explanations.

Nevertheless it is important to keep in mind the isotropic model limitations, especially when dealing with real data: the near-surface layer is usually composed of heterogeneous and non-consolidated material. As such, it may have noticeable anisotropic and anelastic properties.

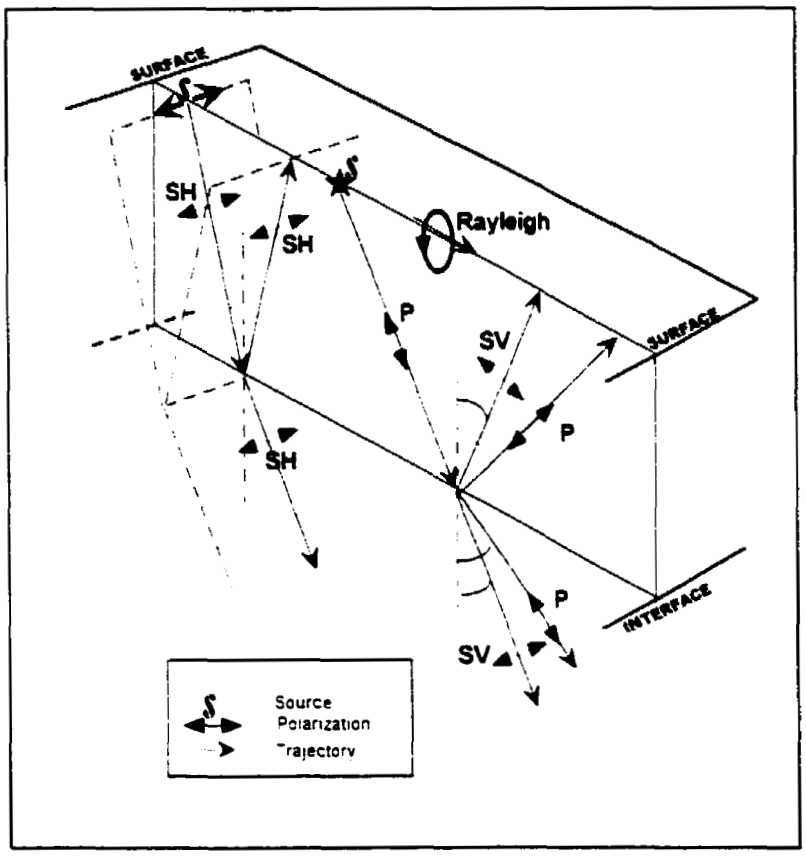

Figure 1.1. Schematic diagram of the two multicomponent seismic methods on land. On the left, pure *S* waves (*SH*) and on the right, a converted *S* wave (*SV*). The energy source is different in each case (an *SH* source in the first case and a standard P wave source in the second). The path of the trajectory is symmetrical for *SH* waves and asymmetrical for converted waves. (Modified after Tatham and McCormack, 1991).

1.2.3. Multicomponent seismic exploration

The seismic method of exploration takes advantage of the propagation of waves to obtain information about the earth's subsurface. In the land surface method, sensors (*seismometers* or *geophones*) of the earth movement are deployed over the ground surface. A controlled source of energy creates elastic waves that propagate and are eventually reflected by geologic interfaces and detected by the sensors. These waves acquire and carry data along their trajectory concerning the geologic characteristics of the

earth. These seismic recordings are processed and interpreted to produce geologic information.

The sensors of seismic energy on land, usually called *geophones*, have a movable part, the *element* or *component*, that includes a coil, which detects motion along its axis. The conventional method uses one-component geophones that are deployed vertically. Therefore mainly *P* waves are recorded, since they usually arrive almost perpendicular to the earth surface. In the multicomponent land method, geophones with three components (*3-C*) are used. Thus, in principle, the full vector wave displacement can be detected.

A number of configurations for 3-C geophones have been developed: the most commonly used being the *Cartesian* or orthogonal *XYZ* system. In this configuration, one component is vertical and the other two are horizontal. Figure 1.2 illustrates a Cartesian 3-C geophone, where the horizontal components are labelled with *H1* and *H2* and the vertical component with *V*.

Two main multicomponent methods have been developed, using either converted *S* waves (*SV*) or pure *S* waves (*SH*) as illustrated in Figure 1.1. A usual denotation in this case is *PS* for converted waves and *SS* for pure *S* waves. As converted *PS* waves are generated by *P* waves impinging non-vertically over an interface, conventional sources of energy may be used. On the other hand, *SS* waves require a special *S*-wave source of energy. Because of its logistical and data quality advantages, the *converted (PS) wave* technique is more commonly used and has been the object of increasing interest in seismic exploration. In this thesis characteristics and applications to the converted *PS* wave method are emphasised.

S waves have been used to detect fractures, to obtain the V_P/V_S ratio of geologic formations, to differentiate fluids and lithologies, and especially where the conventional method fails (Helbig, 1987; Stewart and Lawton, 1996). The converted-wave method final product are two seismic images of the earth, one with *P* wave reflections and the other one with *PS* wave reflections.

1.2.4. Converted-wave summary

Aspects of the converted-wave (*PS*) method are summarized in the following points, emphasizing the differences with the conventional method:

(1) The design for the data acquisition should take into account the ray asymmetry of the converted wave trajectory.

(2) During acquisition, the direction of the components must be carefully controlled to accurately reconstruct the incident wave. A *tap test* (a little directed hit on the geophone case) is carried out to obtain the polarity of the components.

(3) The components must be rotated about a vertical axis to compensate for the effect of different relative source and receiver locations corresponding to the same geologic event.

(4) Special methods should be used to correct the receiver statics caused by the near-surface layer effect on the *S* wave (e. g. Anno, 1987).

(5) Techniques to separate wave modes can be used, since *P* and *S* waves can be recorded by any component (e.g. Dankbaar, 1985).

(6) Instead of the common midpoint (CMP) stack of the conventional method, converted waves are stacked by common conversion points (CCP).

(7) Anisotropy analysis for fractures is performed by *S* wave rotations to detect splitting angles and velocities caused by birefringence (e.g. Alford, 1986).

(8) Specific algorithms for DMO and migration have been developed for imaging of converted waves (Stewart and Lawton, 1996).

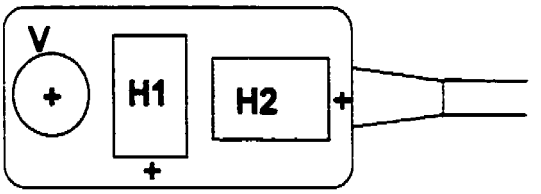

Figure 1.2. Top view of the elements of a Cartesian 3-C geophone. *V* indicates the vertical element, and *H1* and *H2* the two horizontal elements. The polarity is marked by the *plus* sign, which indicates the tap location that causes a positive value in the geophone's voltage output.

1.3. Near-surface effects on multicomponent data

The *near-surface layer* (NSL) of the earth originates from the weathering of in-situ rocks and other environmental processes, such as transport and deposition of sediments. Its thickness is often a few tens of metres, although frequently its interface with the intact rock is not clearly defined. The NSL is usually less compacted, more heterogeneous, geometrically more complicated, and more porous than the consolidated rock below it.

Due to these singular characteristics, the near-surface layer generates unique changes in the seismic waves coming from deeper layers. These changes affect the information from geologic targets carried by propagating waves, sometimes in a very detrimental way. In some technical fields, such as environmental, hydrogeologic or engineering studies, information about this layer is needed and multicomponent methods have been applied with promising results (Dasios *et al.*, 1999; Stümpel *et al.*, 1984). Studies in this direction could contribute in the future to understand and overcome the near-surface effects in exploration.

1.3.1. Characteristics of the near-surface layer

From geological studies the near-surface layer is identified with the *soil* or *regolith*, which is the material on top of the intact rock, the *parental rock* or *bedrock* (Bates and Jackson, 1984). The soil can be *residual* if it originated in the same place where it lays or *transported* if it was carried from another place by any natural means. The residual soil results from the environmental effect on rocks or *weathering*, which can be chemical or mechanical. Water leaches from the surface yielding a saturated zone whose upper limit is known as the *water table*. These characteristics and processes depend on external conditions like geographical latitude or time of the year.

In the conventional exploration method the uppermost near-surface layer is known as the *weathering* or *low-velocity layer* (LVL). The first term emphasises the effect of the environment and the last term originates in the effect that this layer has over the velocity of *P*-waves, related to the marked change in velocity usually presented at the water-table level.

The terms used in the conventional exploration method correspond more to the effect on *P*- wave seismic data than to a geological property. In this thesis, this layer will be identified by NSL, in general, or by LV-NSL, Low velocity-NSL, or HV-NSL, high-velocity NSL, when needed.

Sheriff and Geldart (1995) indicate five effects of the LVL on seismic waves:
(1) high absorption of seismic energy; (2) traveltimes affected by the low velocity and the rapid space variation of the LVL properties; (3) shorter wavelengths, hence smaller features produce significant scattering; (4) the marked change in velocity at the base of the LVL results in wave propagation being nearly vertical (small range of values), regardless of its travel direction beneath the LVL; (5) the high impedance contrast at the base of the LVL makes it an excellent reflector, and produces multiple reflections and mode conversions. Besides these effects, some other aspects are to be considered in the multicomponent method, mainly related with the characteristics of the *S* waves behaviour. The next sections consider the more salient of these differences, such as the velocities model, the wavelength characteristics, the free-surface effect, and the statics correction.

1.3.2. A velocity model for the NSL

Molotova and Vassil'ev (1960) analyze the V_P/V_S ratio variations from data collected at many places throughout the world. Very close to the surface, they found both velocities usually very low, often less than 100 m/s to 200 m/s, with V_P/V_S ratios between 2 and 4. At deeper levels the highest V_P/V_S ratios are found, reaching values of eight or even 14, corresponding to completely saturated porous media with V_P around 1500 to 2000 m/s and low V_S. Finally, the variability of V_P/V_S is lower for consolidated rocks, being from about 1.5 to 3.0.

An interpretation of this velocity model is that in the dry, porous media near the surface both velocities are low, then V_P/V_S is nearly normal; at the water table there is an abrupt increase in V_P but V_S is not affected, then V_P/V_S becomes very high; finally, in consolidated rocks the V_P/V_S is a normal value for solids, since the waves propagate through the solid matrix.

The previous explanation agrees with Wiest and Edelmann (1984), who created a model of *P* and *S* wave velocities for the near-surface layer in northern Germany. For *P* waves a two-layer model inside the unconsolidated sediments was considered appropriate, with an abrupt change in velocity caused by the water table (from about 600 to 1800 m/s). For *S* waves the sequence is more complicated in that more layers can be identified, with a gradual increase in the velocity (from 100 to 400 m/s). They conclude that the increase in velocity is related to an increase in compaction of the solid material.

Thus, an appropriate model would be a progressive increase in the S wave velocity up to the consolidated rock velocities, and an abrupt increase in velocity of the P wave at the water table. This velocity model is illustrated in Model 2 of Chapter 2.

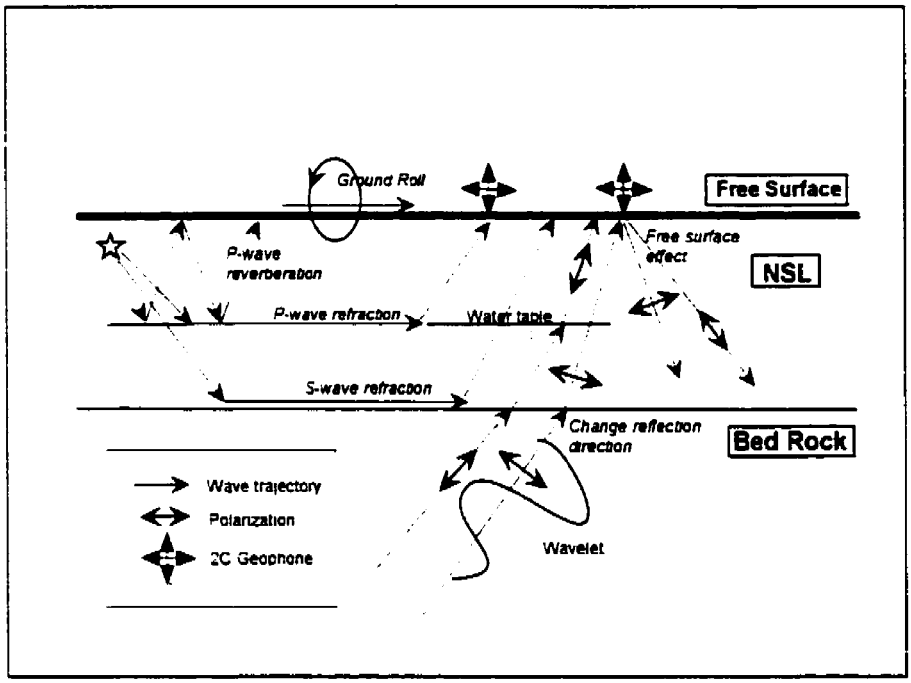

Figure 1.3. Schematic diagram of some near-surface layer effects in elastic wave propagation. There are included the change in direction of the wavefront, the free-surface and water table effects, and interfering events like surface waves, reverberations, and refractions. *P* waves are more affected by the water table while *S* waves by the solid component.

Some of the effects of the NSL in elastic waves are illustrated in Figure 1.3. The model represents an elastic solid limited above by the free-surface. The solid is composed of two parts: the near-surface layer with relatively low wave velocity and including the water table, and a half-space with higher velocity corresponding to the bedrock.

1.3.3. The free-surface effect

Waves travelling upwards in the earth's interior are reflected and converted at the free-surface. The conversions generated there depend on the incident-wave mode, on the elastic properties of the solid and on the angle of incidence of the wave. The resultant wave movement is known as the *free-surface effect*, which has been object of many studies (e. g. Knopoff, et al., 1957; Meissner, 1965; Evans, 1984). Eaton (1989) analyzes the free-surface effect on the AVO (Amplitude Versus Offset) method.

The free-surface effect can be expressed as vertical and horizontal displacements, which are of considerable interest in exploration, since these displacements correspond to the components of displacement of a Cartesian geophone deployed on the land surface. Mathematical expressions may be derived for relative amplitudes as a function of the angle of incidence and the elastic parameters, as shown in Appendix C for the 2-D case. These expressions are a particular case of the Zoeppritz equations (without a transmission medium) and are also known as the *geophone response*.

To illustrate the geophone response, examples of two V_P/V_S ratio are in Figure 1.4. Incident P wave and S wave cases are shown. The curves labeled with an R represent the response to a unit incident wave, for horizontal (h) and vertical (v) responses. Notice (equations C.14 and C.15) that the curves depend only on the V_P/V_S value.

Due to these interactions between P and S wave, the motion detected by the geophone can be very different from the incident body-wave motion, depending on the angle of incidence. In the case of an incident S wave, a critical angle of incidence is defined, beyond which phase rotation modifies the shape of the wave. The critical angle depends on the elastic properties, as illustrated in Figure 1.4: it is 15° for a V_P/V_S of 3.75 and 30° for a V_P/V_S of 2. Figure 1.5, after Meissner (1965), illustrates this waveform change. This

phase change has implications in exploration methods. (e. g. Crampin. 1985. noted in section 3.2).

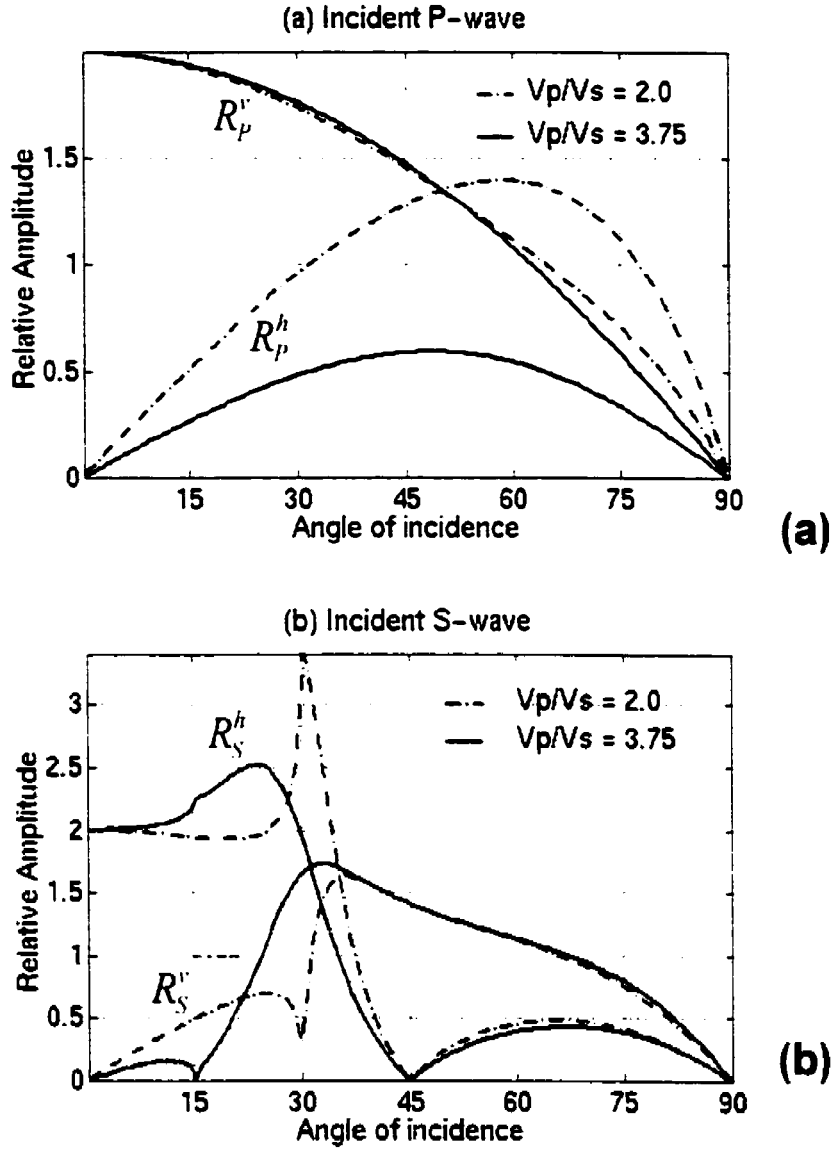

Figure 1.4. The free-surface response as a function of the angle of incidence and the Vp/Vs ratio. Two Vp/Vs ratios are considered in this example. The coefficients R_M^d are the ratio between the amplitude of the incident mode M (P wave or S wave), and the resultant amplitude in each of the two directions d (v for Vertical and h for Horizontal). (a) Incidence of a P wave. (b) Incidence of an S wave.

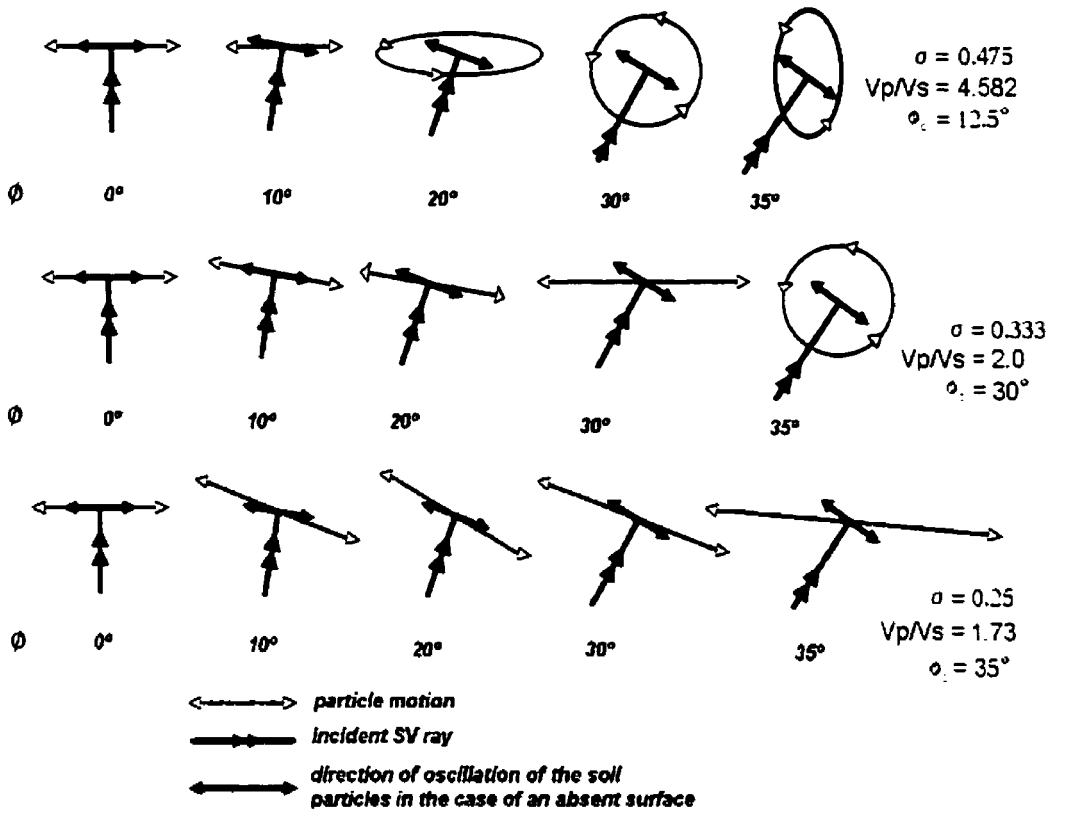

Figure 1.5. Examples of the free-surface effect on surface particle motion for an incident *S* wave. The surface particle polarization characteristics, direction and linearity, change upon arriving at the free surface of an *S* wave, depending on the angle of incidence ϕ and the V_P/V_S ratio (or equivalently, the Poisson ratio σ). In these examples, each row corresponds to a V_P/V_S ratio with five angles of incidence. The critical angle is ϕ_c (after Meissner, 1965).

1.3.4. Wavelength and the NSL

Since the propagating seismic perturbation has a *waveform*, it is useful to consider the relationship between its characteristics and the NSL thickness. One characteristic of the waveform is the *dominant frequency*, whose wavelength can be considered as a "yard-stick" in seismic exploration, since the size of features that can be observed (*seismic resolution*) is related to this length.

To illustrate this relationship numerical examples are considered. A dominant frequency of 20 Hz and a velocity between 200 m/s and 400 m/s can be considered typical for *S* waves in the near surface. In this case, the wavelength would be between 10 and 20 m. In the case of *P* waves, assuming a velocity of 600 m/s and a frequency of 25 Hz, the wavelength would be 24 m.

Therefore two conclusions arise: these wavelengths are comparable to typical NSL thickness, and, as the *S* wavelength is shorter, smaller geological features affect *S* waves.

1.3.5. Statics correction

Due to the horizontal variations in the NSL properties, the arrival time of events with information from deeper layers is relatively delayed between geophones. To recover reflection time independent on NSL characteristics, the traces are shifted towards a reference level or *datum*, in a procedure known as *statics correction* in the seismic exploration industry. More details are in Cox (1999).

Statics correction has been long studied and often well handled for *P* waves in the conventional seismic method. Because the lower *S*-wave velocities, *S*-wave statics are usually much larger than their co-located *P*-wave statics. In addition, *S* waves are more affected by the NSL heterogeneity, since they have shorter wavelength and, as less affected by the water table, are more affected by the more variable properties of the solid matrix. Therefore, the statics corrections for *S* waves are usually larger and not necessarily correlated with the statics correction of *P* waves.

Methods for *S* wave statics correction have been developed, and are currently being applied (e.g Anno, 1984; Wiest and Edelmann, 1984; Tatham and McCormack, 1991; Cary and Eaton, 1993), however with some limitations compared with the statics correction methods applied to *P* waves

1.3.6. NSL effects summary

For purposes of this thesis, NSL effects can be separated into three groups:
(1) Influence of the free surface on wave propagation (whose theoretical model is the boundary between an elastic half-space and the vacuum), such as the free-surface effect (see section 1.3.4) and surface waves.
(2) Effects related to the vertical structure of the near-surface layer, such as the change in direction of waves propagating from deeper layers, reverberations and refractions, the water table effect in P-wave propagation and the relationship between the layer thickness and the wavelength.
(3) Effects related to the horizontal changes in the NSL like the surface and the bed-rock geometry, and the heterogeneity of elastic properties. These characteristics are the main causes of the statics lateral variation (section 1.3.5).
Effects that are not considered by the theoretical model assumed in this thesis, such as anelasticity and anisotropy, may be important and apply to (1) through (3) mentioned above.

Modelling (Chapter 2) and polarization analysis (Chapter 3 and 4) assume a model affected by (1) and (2), the free-surface effects and the effects related with the vertical structure of the NSL. Chapter 5 is related to the effects in (1) and (3), which are basically related with the statics correction in the seismic method. Anelasticity and anisotropy involve more complicated theoretical models.

1.4. Scope of the thesis

The main purpose of this thesis is to contribute to the identification and understanding of NSL effects on multicomponent land data in land and to assist in overcoming them. Some non-conventional methods and problems are attempted. Synthetic and real data are tested.

The theoretical model corresponds to elastic, homogeneous, isotropic media, excluding anisotropic or anelastic effects. Lateral variations of the NSL are excluded in synthetic data analysis and considered as time shifts in the mode separation algorithm.

Characteristics tested on geologic models are the Low velocity-NSL. High velocity-NSL. and dipping reflectors.

Polarization is a property of seismic data affected by the NSL. Besides that. this property has an information content not greatly used in seismic exploration at present. Polarization analysis. filtering and recovering of information are targeted in this study.

The NSL generates many events. which can be detected with the multicomponent method. Use of near-surface generated events for geophone orientation is studied. taking advantage of the polarization information.

Practical applications considered are analysis of multicomponent data using multiple parameters (direction of propagation. polarization angle. polarization linearity. and amplitude): geophone orientation in multicomponent acquisition: and mode wave separation affected by statics.

1.5. Methodology

The analyzes were performed mostly in the shot domain. In synthetic data. a two-component two-dimension (2C-2D) model was used. Real data came from an experimental 3C-2D seismic survey. In addition to pre-stack data the algorithm for mode separation in the presence of statics was tested on poststack data.

Elastic modelling was used to generate synthetic data (Chapter 2). Two modelling methods were employed. Finite Differences and Ray Tracing. They are complementary to one another for analysis purposes.

Polarization data were analyzed using a graphical method. hodograms. and statistical methods. covariance matrix and histograms (Chapter 3 and 4). These methods can be considered complementary to one another. and using them allows the results to be confirmed or rejected.

Fourier transform, τ-p transform, and least-squares inversion are used in the wave mode separation algorithm (Chapter 5). The resulting mode separated data were processed up to stack section.

1.6. Software tools

Algorithms for polarization analysis, for mode separation and for graphical output were coded in Matlab™ , a facility for matrix calculation. Real data were processed using the commercial software ProMAX™, which also was used to generate graphical output. The program xv, shareware by GNU for graphic output was also used.

For Finite Difference modelling, a code in Fortran 77 from the Tomography group at the University of Utah (USA) was used. Ray tracing modelling was performed with the software GX-II™ and Norsar2D™. Another commercial modelling package, Osiris™, was used to create synthetic seismograms for wave mode separation with statics. The figures were prepared in CANVAS™, and the complete thesis was written and assembled in Microsoft Word™

CHAPTER 2

SYNTHETIC DATA ANALYSIS

2.1. Introduction

Propagation of seismic waves through elastic solids can become very complex, and consequently difficult to analyze or visualise. Numerical simulation of seismic waves, usually called *modelling*, is a useful tool to understand the complexity of the wavefield. According to Sheriff and Geldart (1990), "modelling is important as an aid to understand how various types of possible features might appear in seismic data " (p. 390). The results obtained are *synthetic seismic data* or *synthetic seismograms*. Modelling is used in this chapter to illustrate the effect of the NSL and the behaviour of elastic waves in a number of geological cases.

There are many algorithms to create synthetic seismic data, distinguished by the grade of accuracy and computational efficiency. Two methods are used here: *Finite difference* and *Ray tracing*. The finite difference method (FDM) is a simulation of the complete wavefield while, with ray tracing only traveltimes are obtained. Both methods can be considered complementary, since FDM is a more accurate representation, whereas RT allows the identification and analysis of specific properties.

2.2 The finite difference method

FDM is a general technique used to solve any physical problem expressed by partial differential equations. The equation that represents the physical problem is solved numerically using small finite steps or *finite differences*, instead of the infinitesimal partial differentials. Since this method generates the complete wavefield, it has been an active research field since introduced in seismology (e. g. Boore, 1972; Levander, 1988). It enables studies that are difficult or impossible with other methods. For example to generate *snapshots* (instantaneous views of the wavefield), to examine all the events, to

establish complex geometrical layouts, and to implement different wave equation approaches.

FD modelling involves a discrete version of the wave equation, propagating by time steps through a discrete geological model. An approach to wave propagation is selected, in principle with no limit to the complexity of the mathematical model, even if that complexity can affect its practical implementation. To obtain the discrete representation, the mathematical model, which contains partial differentials, is approximated to a differences equation. The difference approximation to the differentials in the equation is usually based in the truncation of the Taylor series representation. A *calculation scheme*, sometimes called "stencil" or "computational star", is defined based on that finite difference equation.

The geometry and the elastic properties of the medium define the geological model, which is represented as a grid of squares. The source of energy is included in the initial conditions. After all these parameters are defined, the entire wavefield can be calculated throughout the geological model sequentially by time steps.

Two potential numerical problems, namely *stability* and *dispersion*, have to be taken into account to define the grid size and time step properly. If the grid size does not take into account the velocity field, the calculations can become unstable. Insufficient sampling of short wavelength components causes numerical dispersion, that is, non-physical dependence of velocity on frequency. The stability and dispersion criteria should be satisfied by the wavelengths and the calculation grid to reduce numerical dispersion and make the model stable (Karl, 1989). These requirements define a relationship amongst the space grid, the time step and the frequency content of the source of energy. On the other hand, the computational efficiency is very sensitive to the size of the space grid matrix and to the number of time steps, which introduces a limitation to the practical accuracy of the method.

Another artificial event is the reflection from the boundaries, created by the finite size of the model. Methods to reduce these spurious reflections have been developed and should be applied in order to obtain a more accurate result.

The algorithm used in this work, derived by Levander (1988), solves for the elastic (*P-SV*) wavefield in two dimensions, horizontal and vertical. It uses the coupled first-order differential equations of motion expressed as particle velocities and stresses (equations A.1 and A.2 in Appendix A). The finite difference approximations are derived from the Taylor series, with an approximation fourth order in space and second order in time. The scheme for calculation is a *staggered grid*, which is advantageous under some boundary conditions. The stability criterion is $0.606 > V_{max} * \Delta t / \Delta h$, and the dispersion criterion is $\lambda_{min} > 5 * \Delta h$, where Δh is the grid size, Δt is the time step, λ_{min} is the minimum wavelength, and Vmax is the maximum velocity.

As for the initial conditions, a point source perpendicular to the free surface was used. Such a source will generate both *P* and *S* waves. The waveform was a zero-phase *Ricker wavelet*. A dominant frequency of 15 Hz was used in most cases, whose time representation and amplitude spectrum are illustrated in Figure 2.1. To reduce the boundary reflections two methods were used simultaneously, an absorbing boundaries method and a damping area applied to lateral and bottom boundaries.

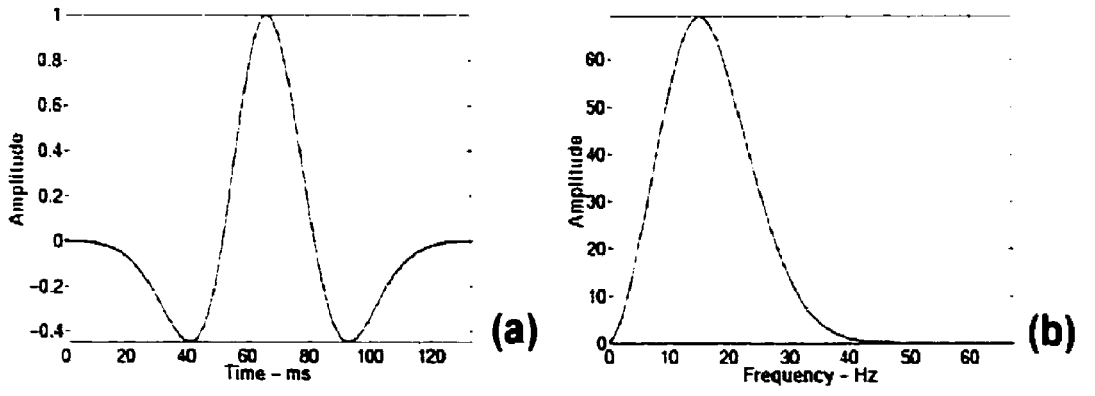

Figure 2.1. Ricker wavelet source used for FD modelling, (a) time domain representation, (b) amplitude spectrum.

2.3. Ray tracing modelling

A *raypath* describes the propagation direction of the energy, which in an isotropic medium is normal to the wavefront. The ray tracing method calculates the traveltime for a raypath between source and receiver, based on the application of Snell's law. Other properties of the wavefield such as amplitudes can be calculated based on approximate solutions and a waveform can be convolved with the resulting traveltimes to obtain traces. This method is considered a high frequency approximation

The ray tracing software programs used were GX-II™ and Norsar2D™. The last one allows the analysis of attributes such as amplitudes and angles of incidence. A vertical source of energy was used, with similar characteristics to the source used with FDM.

Some relevant differences of ray tracing with respect to the FDM are:
(1) It is possible to separate seismic events and to analyze their characteristics.
(2) No Fresnel zone effect is considered.
(3) A plane wave approximation is used.
(3) Attenuation and any other effects on amplitude are not implicit in the model, therefore are calculated specifically.
(4) It is efficient computationally.

2.4. Geologic models analyzed

The geological models are intended to test the NSL effect in simplified typical exploration targets. Computational restrictions are a limit for their characteristics. The NSL is assumed a layer with thickness around 100 m and typically with low wave propagation velocities. However a high velocity NSL is also considered in one model. Only one shot was generated in each case. The exploration target is assumed as a deeper flat reflector. Only vertical variations in the NSL are considered. The following five geological models are studied:
(1) Single horizontal reflector, without NSL.
(2) Horizontal reflector and complex low-velocity NSL.

(3) Horizontal reflector and high-velocity NSL.

(4) Dipping reflector (without NSL).

(5) Dipping reflector with low-velocity-NSL.

2.4.1. Model 1: A horizontal reflector

The first model, illustrated in Figure 2.2, is a single horizontal reflector without a NSL. This simple model enables analysis of the characteristics of the response to a reflector and the effect of the free-surface. This model was used to test polarization methods (Chapter 3) and also the algorithm of wave mode separation in the presence of statics (Chapter 5). Figure 2.3 shows the resulting shot gathers from FDM for vertical and horizontal components. Figure 2.4 shows *snapshots* corresponding to 400, 800 and 1200 ms. Figure 2.5 shows the results of ray trace modelling.

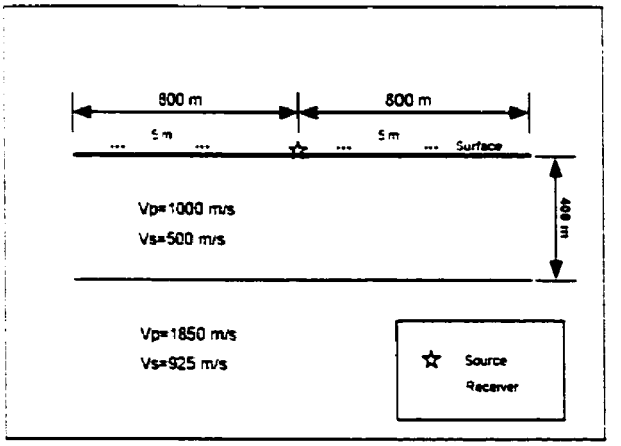

Figure 2.2. Model 1: a single reflector. The receivers are located over a 1600 m spread, separated 5 m from each other. The shot point is located in the middle of them, forming a *split-spread* design. This receivers' spread is the same along all the examples.

Taking advantage of the option to wave modes separation in ray tracing, Figure 2.5c shows the *P* wave field recorded in the vertical component and Figure 2.5d the *S* wave field recorded in the horizontal component. This type of display allows an easier analysis and is also used in the other models.

From the ray tracing results (Fig. 2.5) and from velocities and snapshots analysis (Fig. 2.4). the seismic events are

1. Direct arrival.
2. Surface (or Rayleigh) waves.
3. P wave reflection.
4. Converted wave reflections (P to S and S to P)
5. Pure S wave reflection.

Labels in Figure 2.3 identify these seismic events. Note that the two components show *P* and *S* waves. (Fig. 2.3). and that the direct arrivals and ground-roll are present in FD results (Fig. 2.3) and not present in ray tracing results (Fig. 2.5). Changes in the waveform related to offset are apparent in the ray tracing results (Figure 2.5) and to a subtle extent in FD (Fig. 2.3). FD may be a more accurate description because. as a difference to ray tracing. spherical wave fronts and realistic frequencies are implicit in it.

An analysis based in the Zoeppritz Equations. which relate amplitude and phase variations with offset (or. equivalently. with angle of incidence). was carried out to investigate the characteristics of the events reflected at the interface. Figure 2.6a illustrates amplitude versus angle of incidence to the reflector. Figure 2.6b presents phase versus angle of incidence to the reflector. The relationship between angle of incidence and offset source-receiver is illustrated in Figure 2.7. Zoeppritz equations define the *critical angle*. beyond which the waveforms change because of the phase shift among the frequency components. From Fig. 2.7 the approximate offsets corresponding to the critical angle for each seismic event are:

PP wave: 460 m.
Converted PS wave: 370 m.
Converted SP wave 380 m.
SS wave: 210 m.

A similar analysis of the critical angle and phase changes can be performed on the waves impinging to the free-surface. The free-surface effect (section 1.3.3. and Appendix C) determines amplitude and phase after the incidence of seismic events. and from Figure

1.4 the critical angle for *S*-wave incidence with a V_P/V_S of 2 is 30°. The relation between critical angle and the corresponding offset for *PS* wave mode can be obtained from Figures 2.7 and 1.4. As observed, the converted *PS* event does not reach the free-surface critical angle of 30° along the offsets considered.

On the other hand, *SS*-wave offset corresponding to the free-surface critical angle is 460 m (see Fig. 2.7). From the ray tracing results (Figs. 2.5), a phase change at the *SS* event near to 500 m offset can be caused by this effect. In the FD results (Fig. 2.3) a waveform change in shape can be noticed at farther offset. This shape change can be caused by the free-surface effect.

Figure 2.8 presents the amplitude for converted events, *P*-*S* and *S*-*P*, including effects of geometrical spread, reflection coefficients, and transmission loses. This information is useful in the polarization analysis of chapter 3, since both wave modes arrive simultaneously.

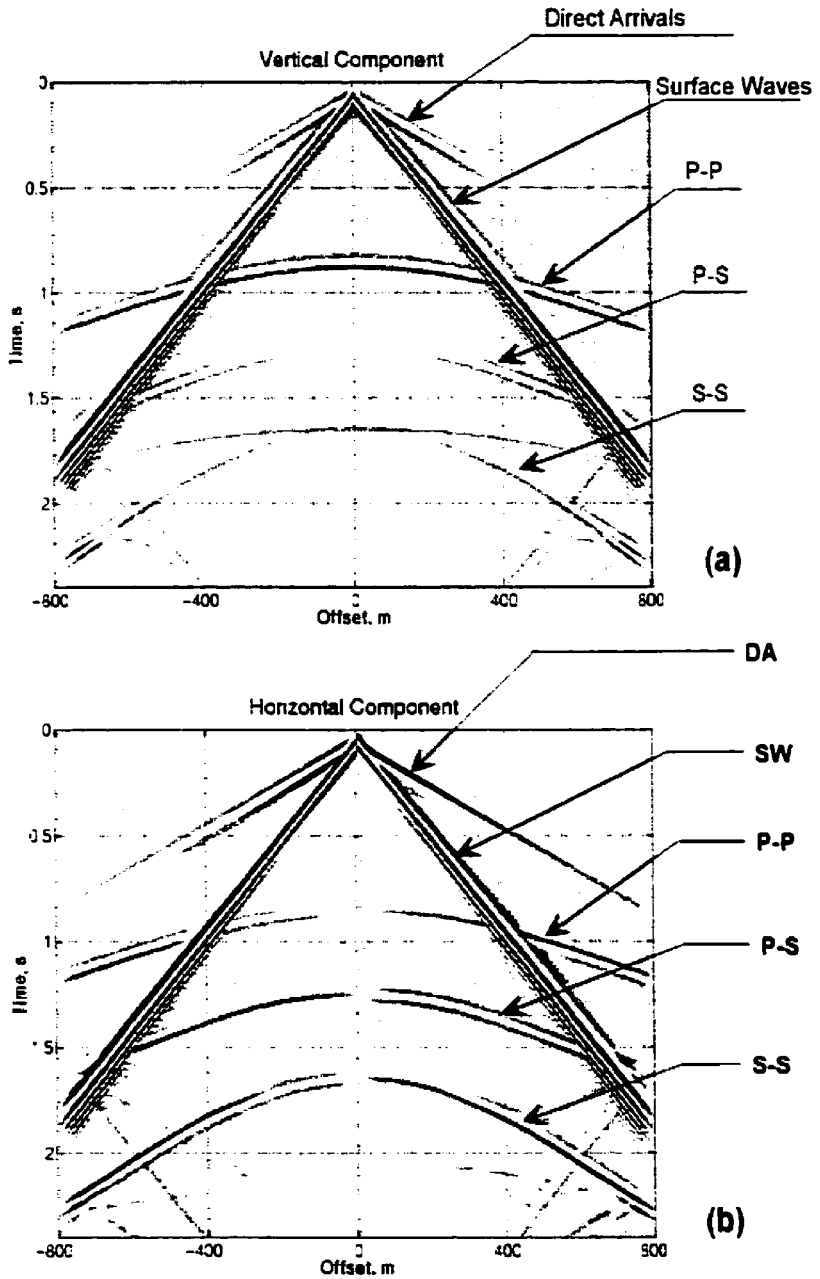

Figure 2.3. Model 1 components after FD modelling. (a) Vertical component. (b) Horizontal component. The events are labeled with a number and the mode identification in (a). A corresponding numerical identification is in (b).

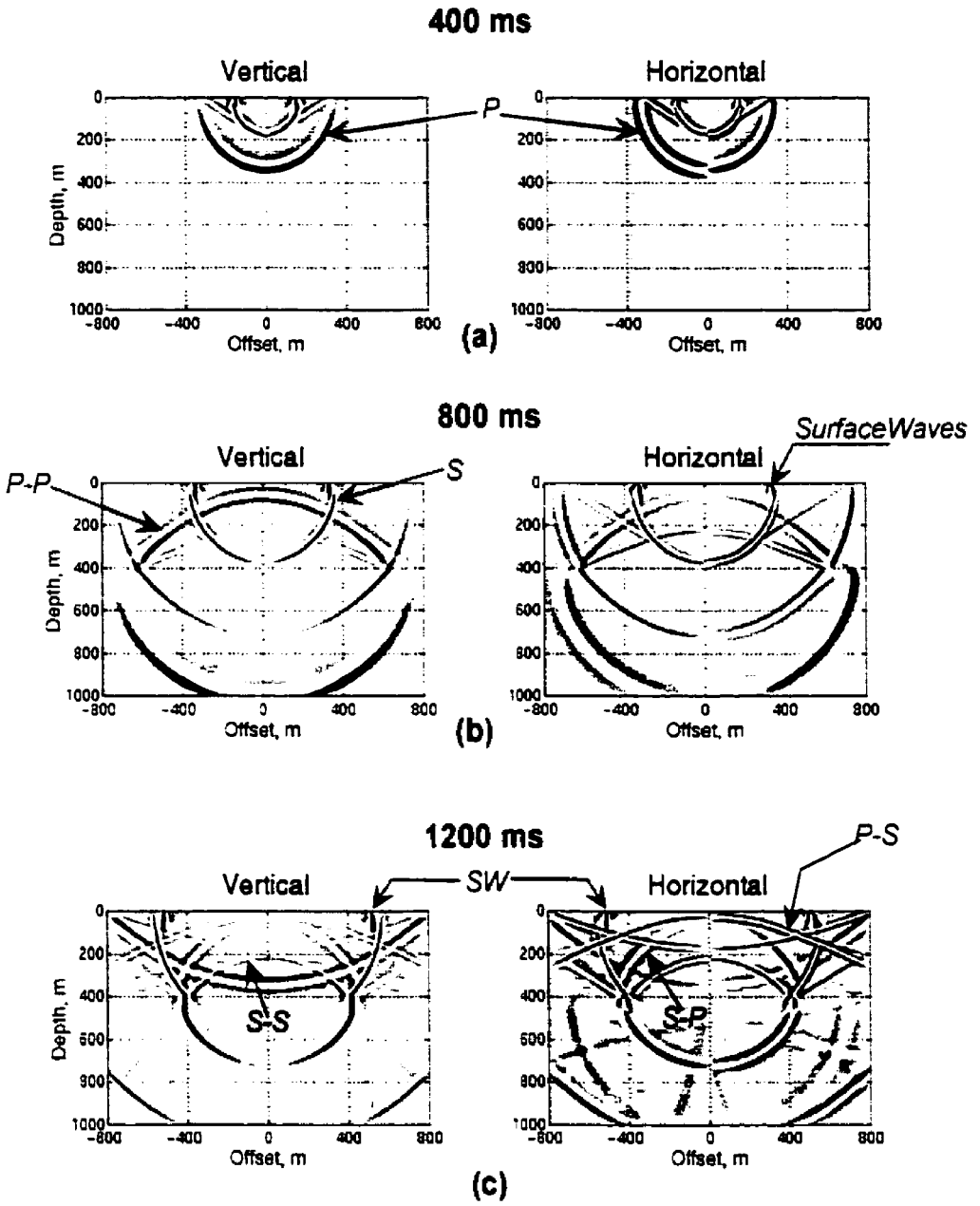

Figure 2.4. Model 1: Snapshots of the two components. The numbers correspond to the identification of seismic events in Figure 2.3.

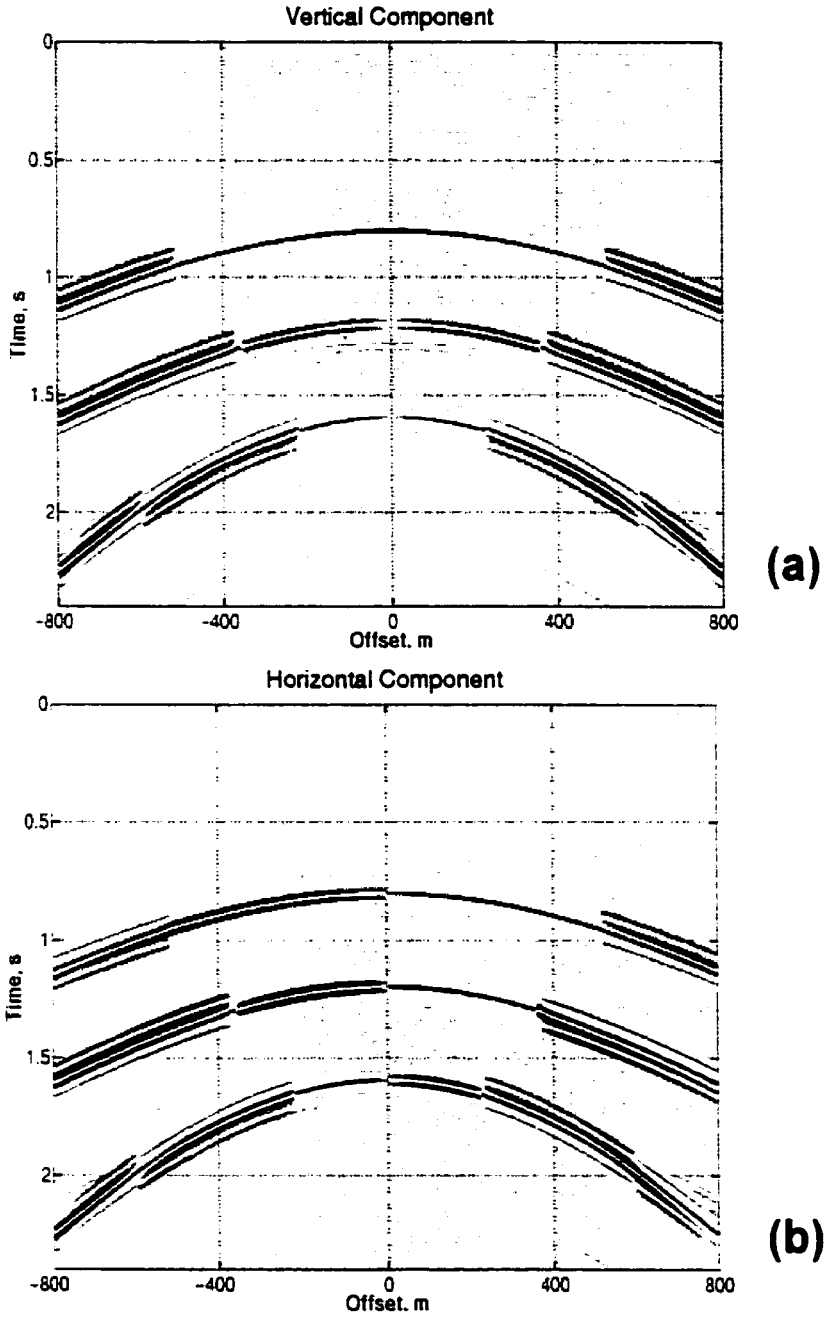

Figure 2.5. Model I components from ray tracing modelling. (a) Vertical component. (b) horizontal component. The waveform changes with the angle of incidence (Continues).

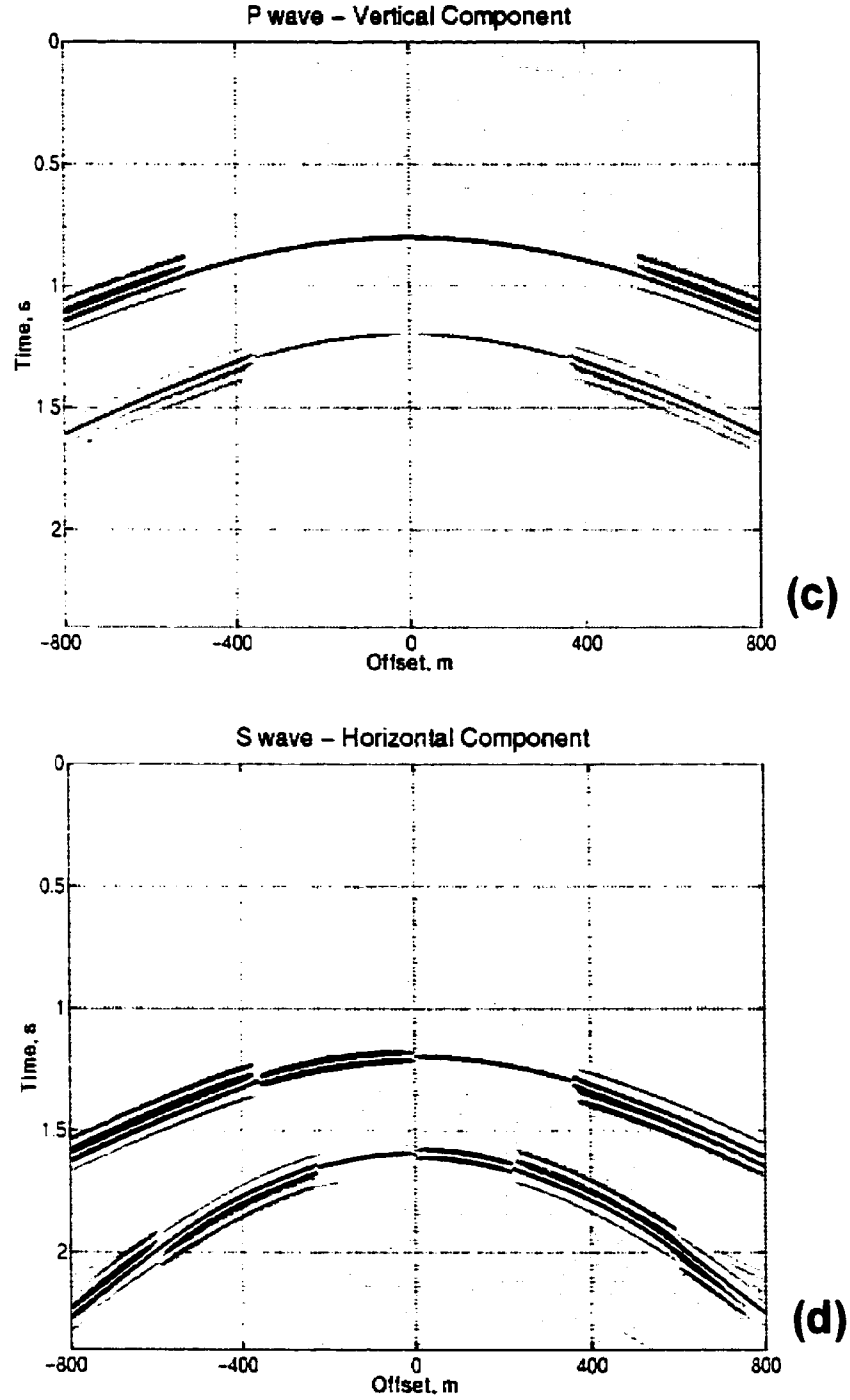

Figure 2.5. (Continued) Model 1 ray tracing components, with separated *P* and *S* modes. (c) *P* wave in the vertical component and (d) *S*-wave in the horizontal component. Note a polarity change at offset 350 m in converted waves (*PS* and *SP*) and at offset 200 m in pure *S* wave (*SS*).

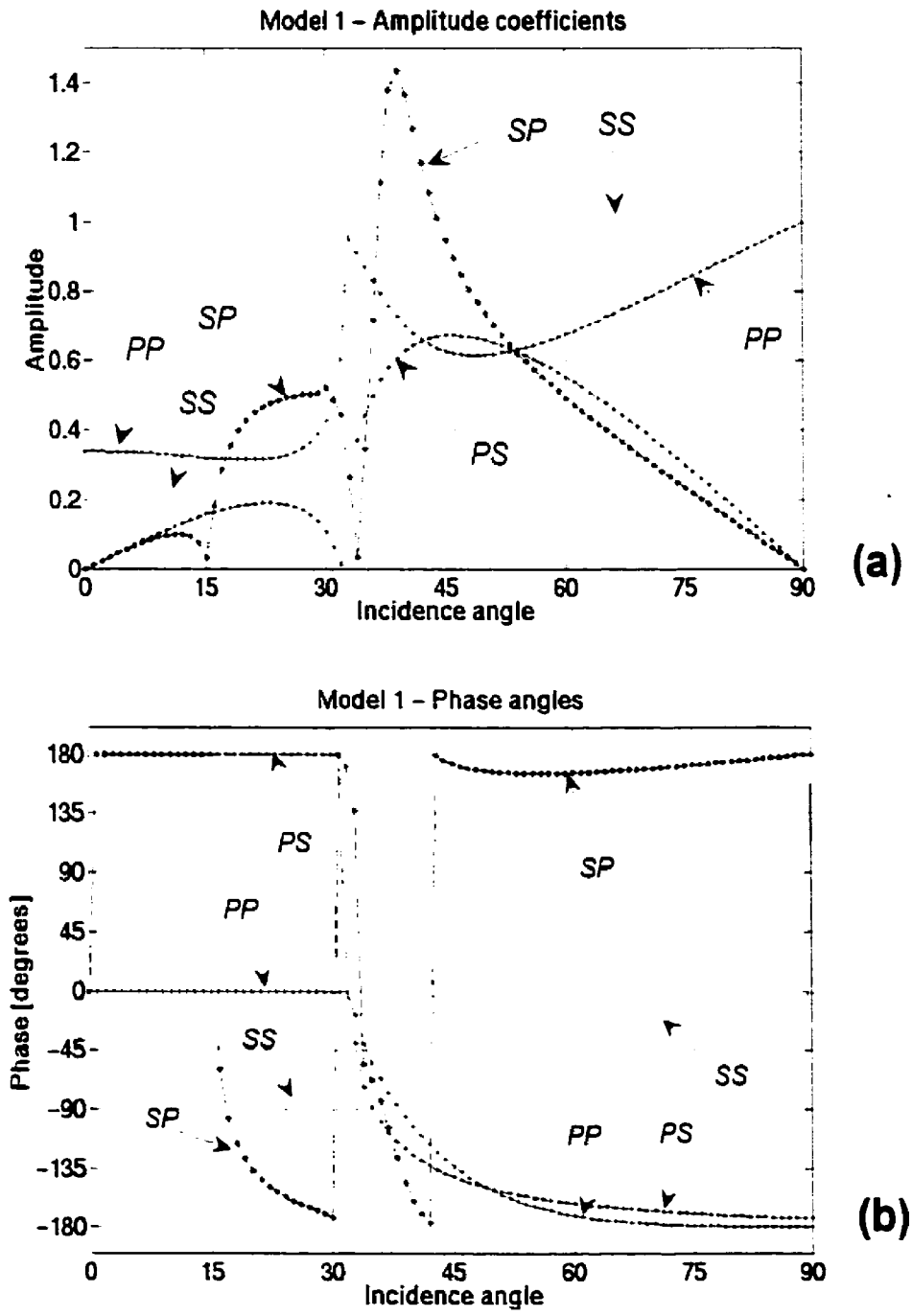

Figure 2.6. Amplitude reflection coefficients and phase angles at the reflector of Model 1. The wave modes are abbreviated as follows: *PP*, pure *P* wave; *SS*, pure *S* wave; *PS*, converted from *P* to *S*; *SP*, converted from *S* to *P*. The critical angles are 32° for incident *P* wave and 15° for incident *S* wave. (a) Amplitude. (b) phase angle.

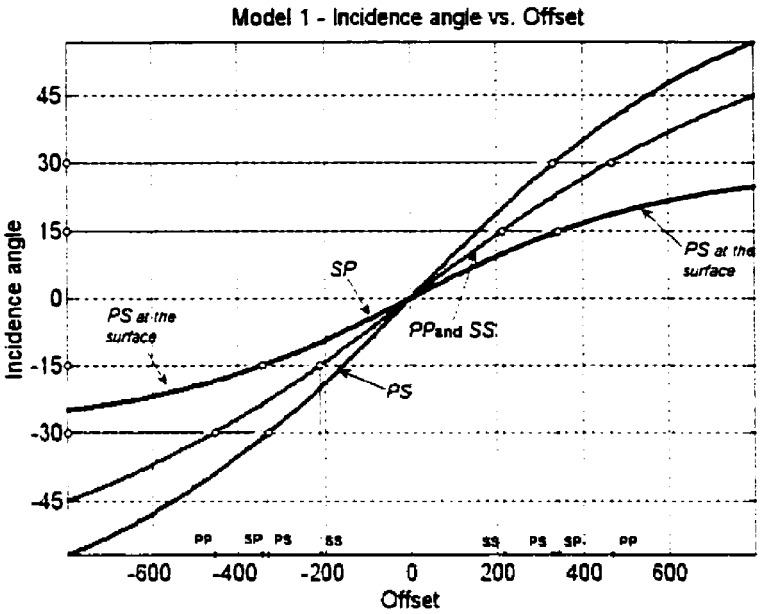

Figure 2.7. Model 1: angle of Incidence to the reflector as a function of offset. The arrows on the offset indicate distances corresponding to critical angles. The angle of incidence of *PS* mode to the surface (equivalent to *SP*) is also indicated.

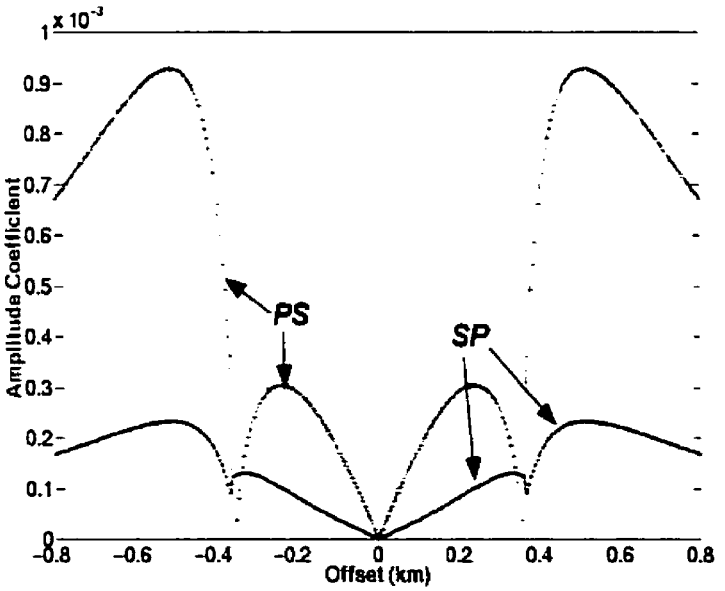

Figure 2.8. Amplitude for PS and SP wave modes as a function of offset.

2.4.2. Model 2: Reflector with a low-velocity NSL

This model is based on the NSL velocities considered in section 1.3.2, as illustrated by the close-up in Figure 2.9b. Its noticeable characteristics are:

1. There are differences in the velocity models of *P*-wave and *S*-wave.
2. The water table defines a dramatic change in *P* wave velocity.
3. *S*-wave velocity change is gradual, since it is less affected by the water table.
4. The V_P/V_S value oscillates before reaching a value typical of consolidated rocks.

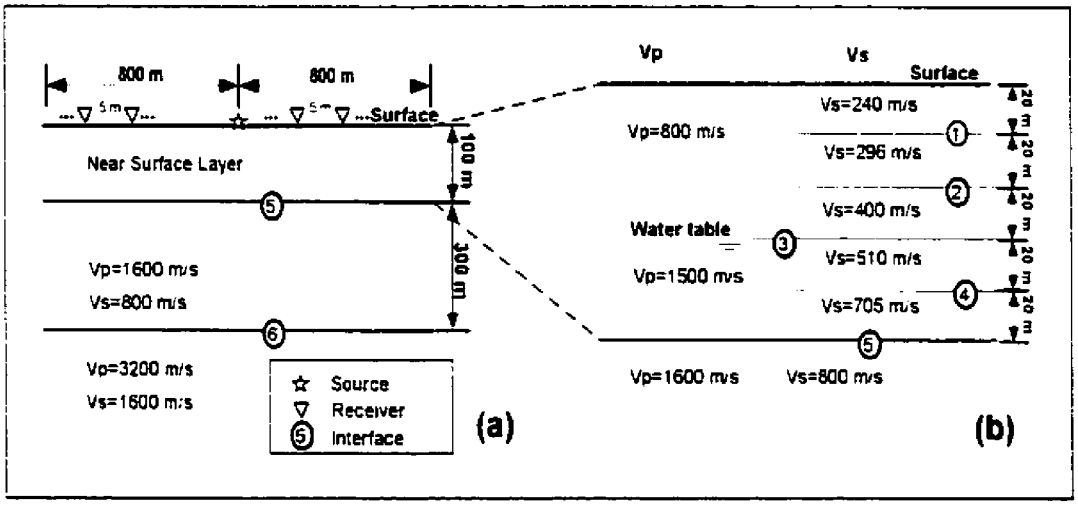

Figure 2.9. Model 2: single reflector and complex near-surface layer. NSL velocity models are different for *P* and *S* waves. (a) General view, (b) close-up of the NSL.

The computational cost of FDM in this case is high, since to satisfy the stability and dispersion criteria, due to the low *S* wave velocity in the NSL, the grid size should be finer and the time step shorter. Compared with Model 1, in this case the distance step is half and the time step four times smaller, which means sixteen times more operations. A space matrix with 2560x1601 nodes result, and have to be calculated for 24000 time steps. Indeed, a Sun Ultra-Enterprise 450™ machine, with 450 MHz CPU speed, 4 GB memory and 4 CPUs, spent around two weeks to obtain these results.

To differentiate amongst the events and facilitate the analysis, the waveform applied to ray tracing had a dominant frequency of 45 Hz.

FDM results are shown in Figure 2.10. Figure 2.10.a illustrates the data recorded in the vertical component and Fig. 2.10.b in the horizontal component. Figure 2.11 shows the snapshots, and Figure 2.12 shows the result of ray tracing. Figure 2.12.a presents *P* wave in the vertical component and Figure 2.12.b presents *S* wave in the horizontal component. Figure 2.12c shows the complete vertical gather, with all the events (i. e. it is the ray-tracing equivalent to Figure 2.10.a, the vertical gather from FD).

The *noticeable* events are identified in Figure 2.12 as follows:

1. *PP* reflection from the water table.
2. *SP* converted from the water table.
3. *PP* reflected from the deeper layer.
4. *SP* converted from the deeper layer.
5. *PS* converted from the bed rock.
6. *PS* from the water table.
7. *PS* conversions from reflector 6.
8. *SS* reflections from reflector 6.
9. *SS* reflections originated at *S*-wave interfaces of sub-layers inside the NSL.

FD modelling shows events not present in ray tracing results, the principal of them identified by numbers in Figure 2.10, as follows:

10. Rayleigh or Surface waves.
11. Possibly reverberations from the water layer.
12. Possibly dispersed S-waves from the NSL and/or guided waves.
13. Artefact caused by remaining boundary reflections.

Comparing with the seismogram of Model 1 (Fig. 2.3), events related to the near surface interferes with the up-going events from the reflectors. The event identified as guided waves or dispersive *S*-reflections, which forms a cone, can be related to the source frequency content and the corresponding wavelengths, since the *S*-wave wavelength corresponding to 15 Hz (the dominant frequency), is larger than the thickness of some of the near-surface layers, therefore dispersion can be generated.

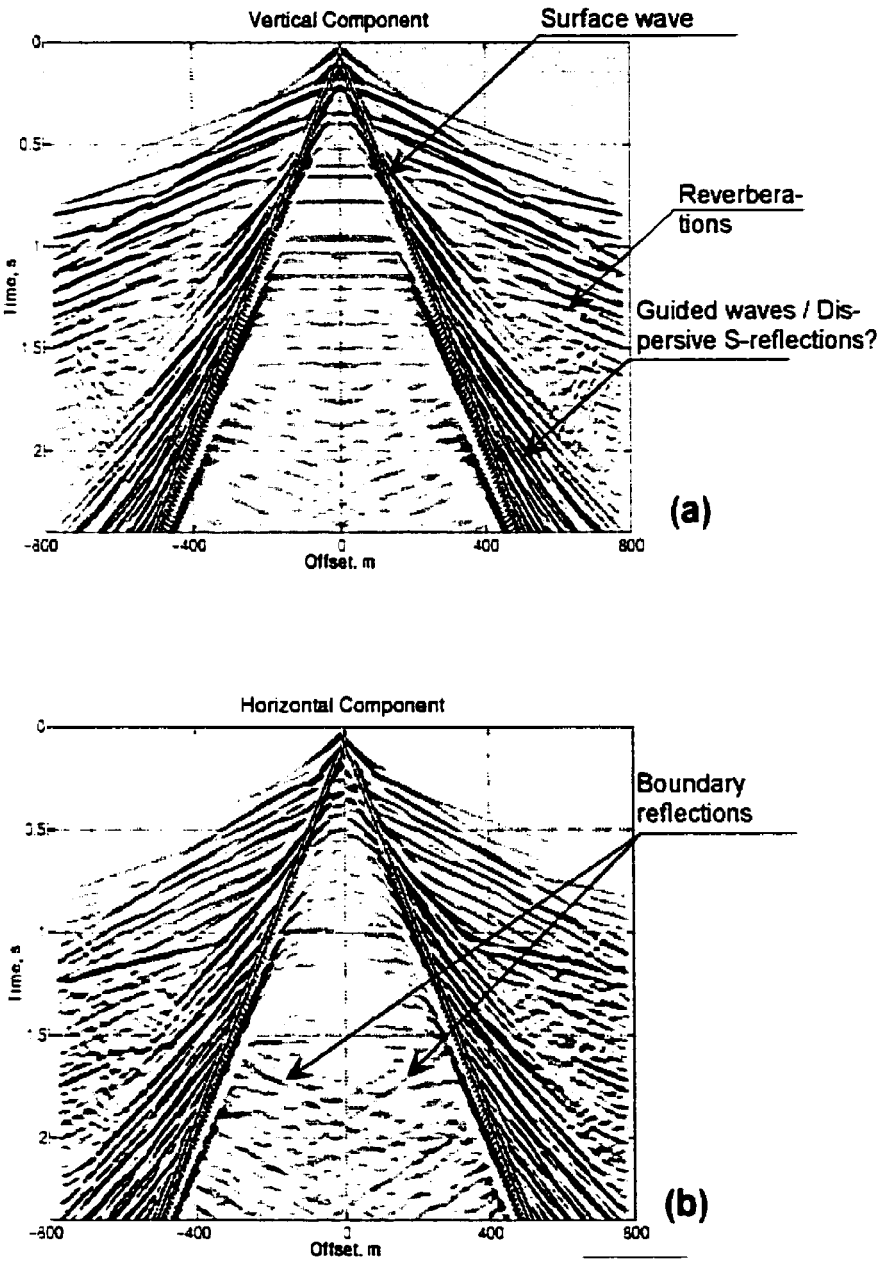

Figure 2.10. Model 2 components from FD modelling. (a) vertical and (b) horizontal. Events not shown by ray tracing modelling, are labeled here.

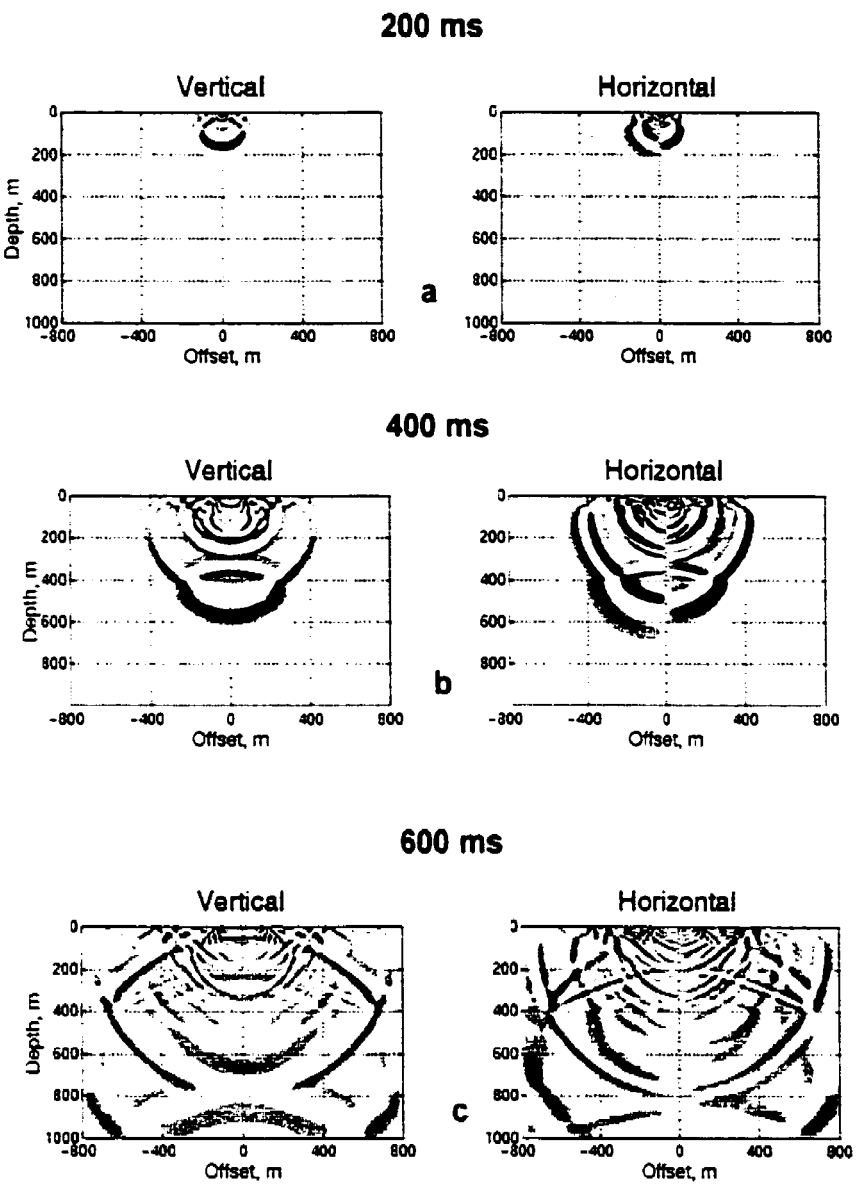

Figure 2.11. Snapshots of Model 2. Many seismic events and much of the energy is concentrated in the NSL layer.

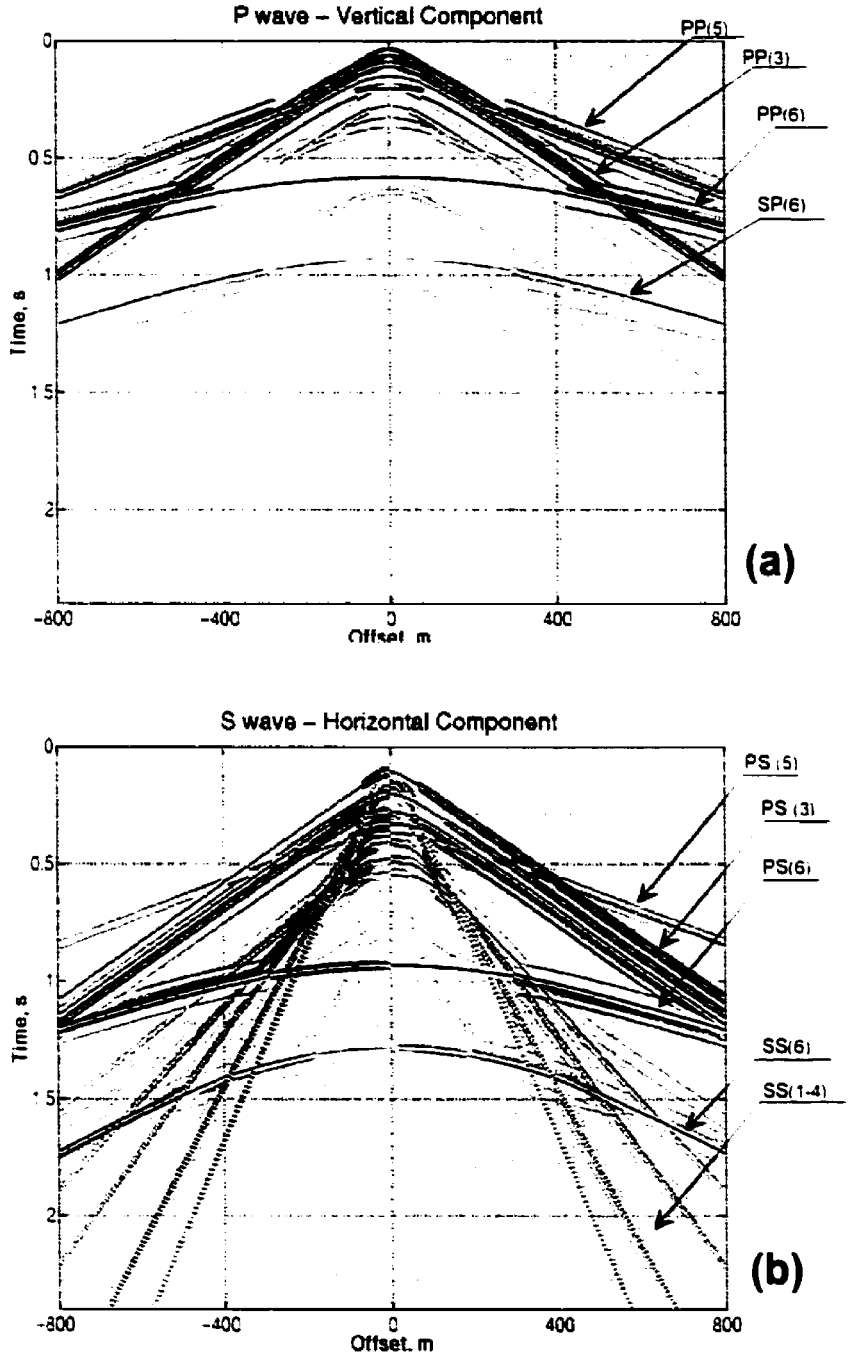

Figure 2.12. Model 2 ray tracing components separated in *P*- and *S*-wave modes. (a) Only *P* wave in the vertical component and (b) only *S* wave in the horizontal component. (c) vertical component including all the events. The events identified are labeled with the type of event and, between brackets, the number of the interface where originated.

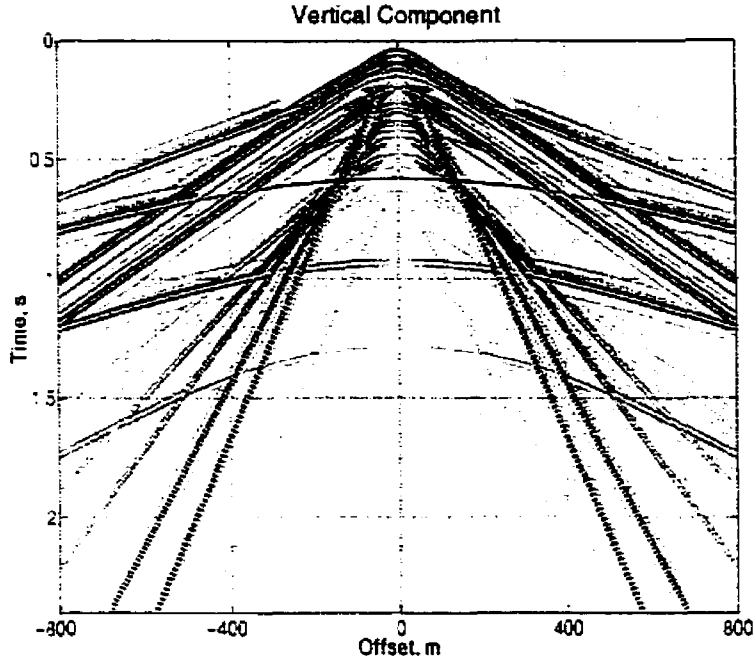

Figure 2.12 (continued). Model 2 ray tracing components separated in *P*- and *S*-wave modes. (c) vertical component including all the events.

Figure 2.13 shows attributes of converted *PS* mode. Figure 2.13a compares the angles of incidence to the surface as a function of offset without and with a NSL, that is for Model 1 and Model 2. Figure 2.13b compares the amplitudes for converted waves (*PS* and *SP*) at interface 6. Since *PS* and *SP* modes generated at interface 6 arrive simultaneously, as shown in 2.12a and 2.12b, these amplitudes are useful to analyze the polarization of the resultant.

The presence of *P*-wave in the horizontal component and *S*-wave in the vertical (known as *leakage*) seems low compared with Model 1, as expected because of the incidence angle close to the vertical of the reflectors caused by impedance change in the low velocity –NSL. This angle is less than 10° for the *PS* reflection coming from interface 6 (Figure 2.13.a), then no phase change caused by the free surface is expected, since is lower the critical angle (which is 20° for a V_P/V_S value of three).

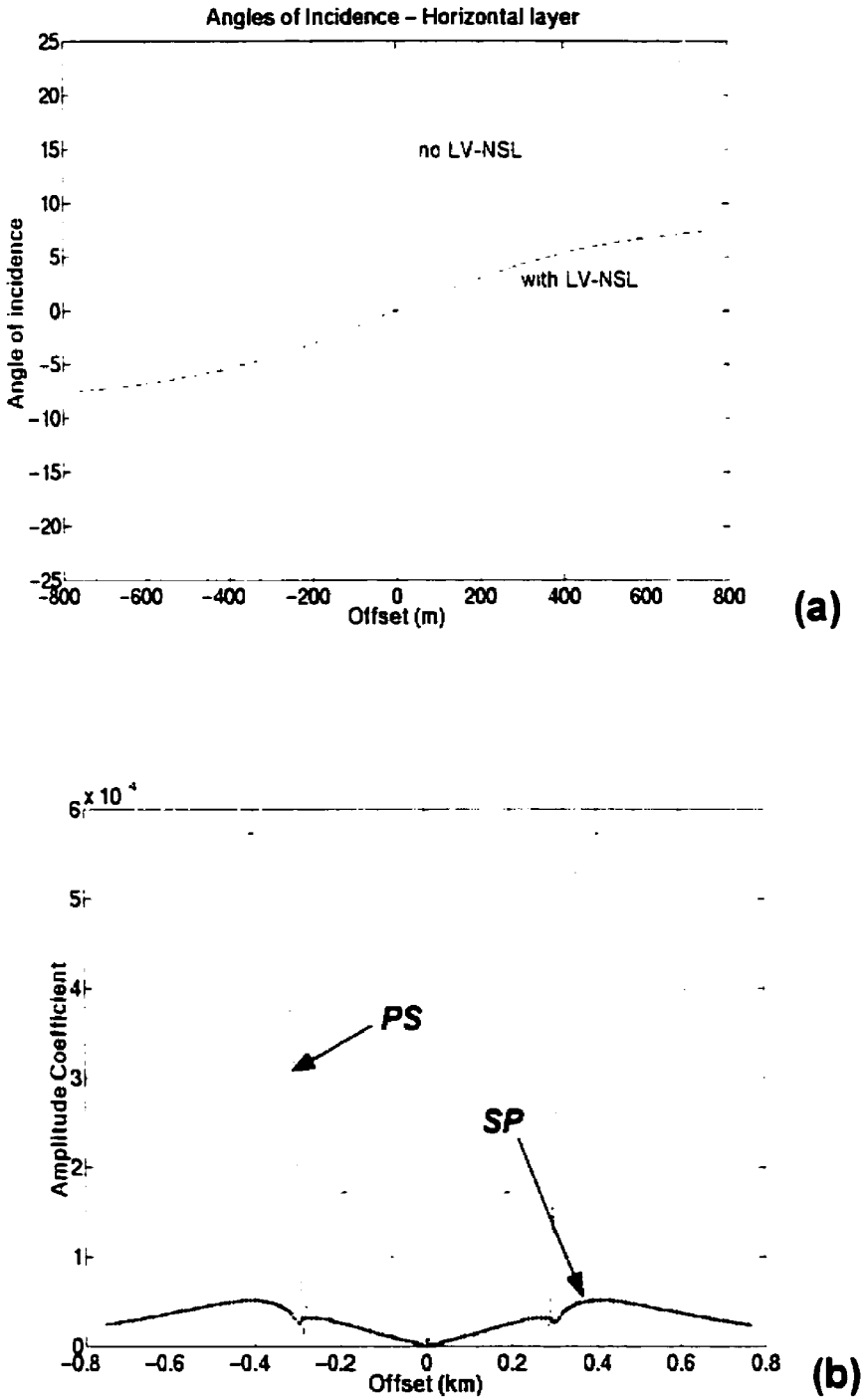

Figure 2.13. Analysis of PS mode angle of incidence and amplitude. (a) comparison of angle of incidence to the surface with (Model 2) and without (Model 1) a LV-NSL. (b) comparison of amplitude for *PS* and *SP* reflections from interface 6 for model 2.

2.4.3. Model 3: High-velocity near-surface layer.

Model 3, illustrated in Figure 2.14, includes a High-Velocity NSL (HV-NSL). This kind of geological setting can be present in certain places, e. g. volcanic rocks on the surface or carbonate outcrops. Since the high velocity increases the wavelength, the dominant frequency of the source of energy is 20 Hz, instead of the 15 Hz used in the other models. For 4000 m/s the wavelength corresponding to the dominant frequency of 20 Hz is 200 m, i. e. twice the thickness of the layer. The dominant frequency of the ray tracing wavelet is 30 Hz, the wavelength of which in the HV-NSL is 150 m, i. e. again larger than the thickness of this layer.

Figure 2.15 shows the vertical and horizontal components resulting from FD modelling. Figure 2.16 shows comparable results obtained using ray tracing. To make the analysis easier, the wave modes are separated, only *P* waves in the vertical component and *S* waves in the horizontal.

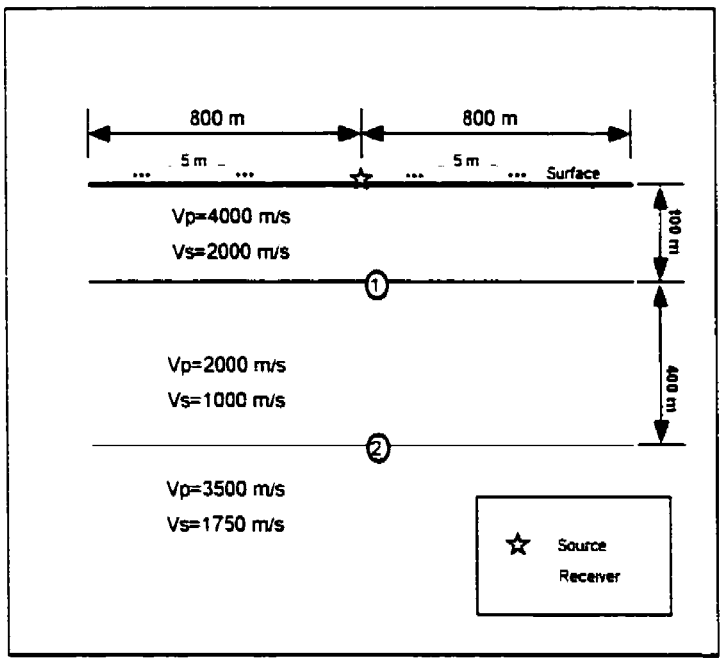

2.14. Model 3: High-velocity near-surface layer.

Ray tracing enables the differentiation of events, which are identified in Figure 2.16, as follows:

1. *PP* and *SP* reflections from the first interface.
2. *PP* reflections from the reflector
3. *SP* (converted) reflections.
4. *PS* (converted) waves from the first interface.
5. *SS* waves from the first interface.
6. *PS* waves from the reflector.
7. *SS* waves from the reflector.

Phase change occurs in *SS* reflections. The offset corresponding to these phase change is approximately 115 m in *SS* reflection from interface 1, and larger than 450 m in *SS* reflection from interface 6. These offset values agree with the critical distance that correspond to a V_P/V_S ratio of 2, and to the deep of the two reflectors. Figure 2.17 shows the angle of incidence to the surface of the *PS* converted wave. Although this angle is close to 30° (the critical angle) at far offset, it is still under the critical angle and no phase change can be expected.

Some events in Figure 2.15 (from FD) do not have a corresponding one in Figure 2.16 (from ray tracing), since some of them are mode conversions such as *PSSP*, *SPPS*, or PSSS , which, to be calculated with ray tracing , have to be specified.

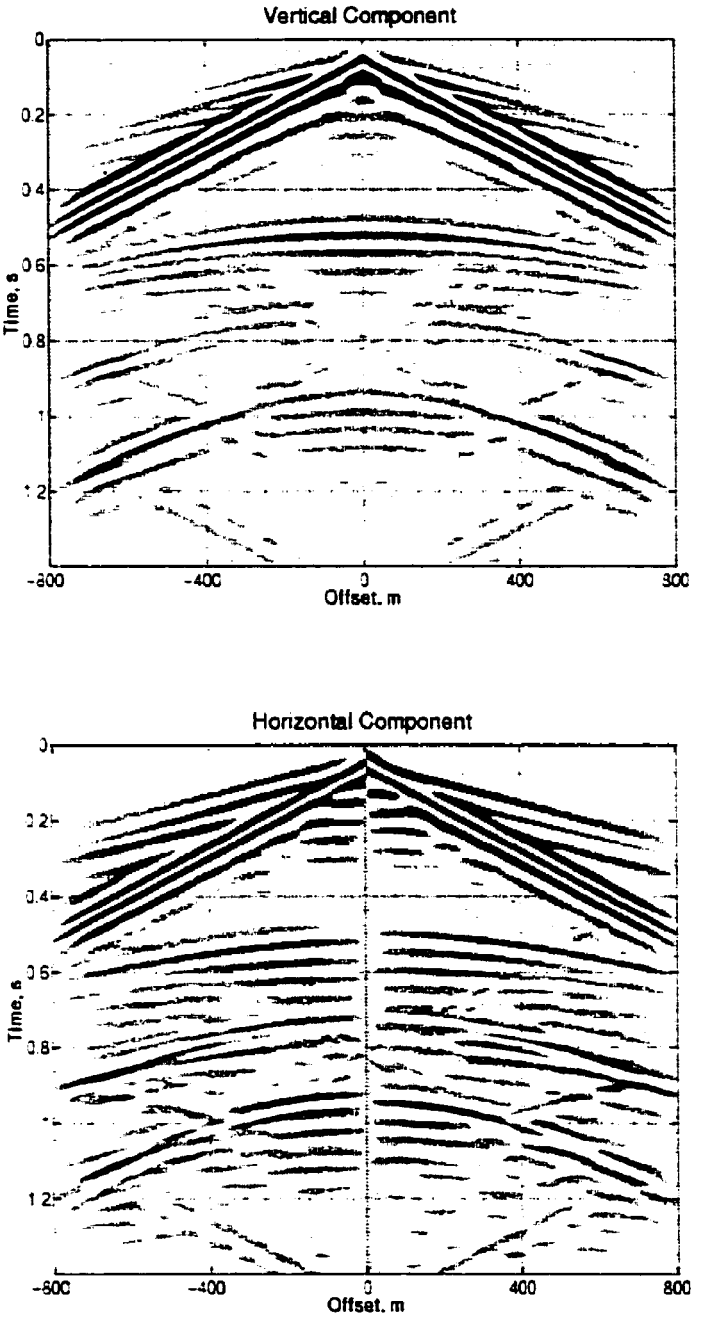

Figure 2.15. Model 3 vertical and horizontal components calculated with FD modelling.

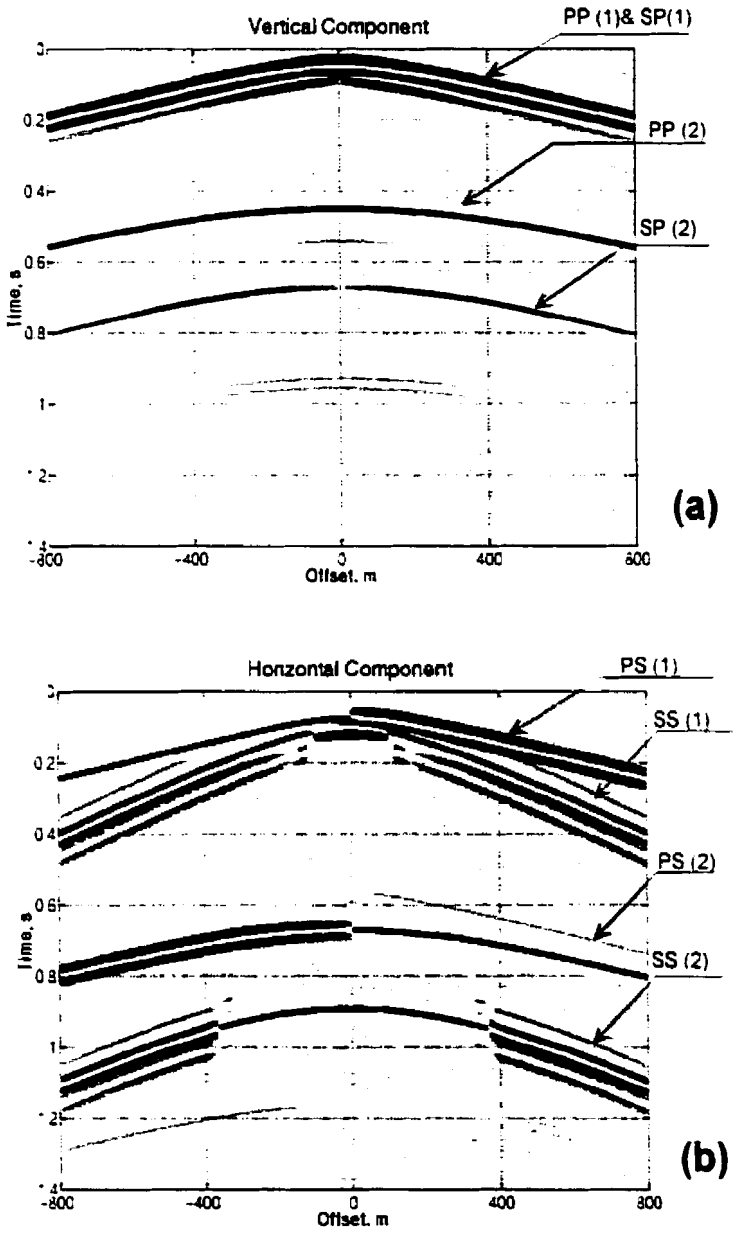

Figure 2.16. Model 3 components using ray tracing, separated in *P* and *S* wave modes. The events are identified with the wave-mode label and the interface number of Fig. 2.14. (a) *P* waves on the vertical component. (b) *S* waves on the horizontal component. Phase change can be only noticed in the *SS* reflections.

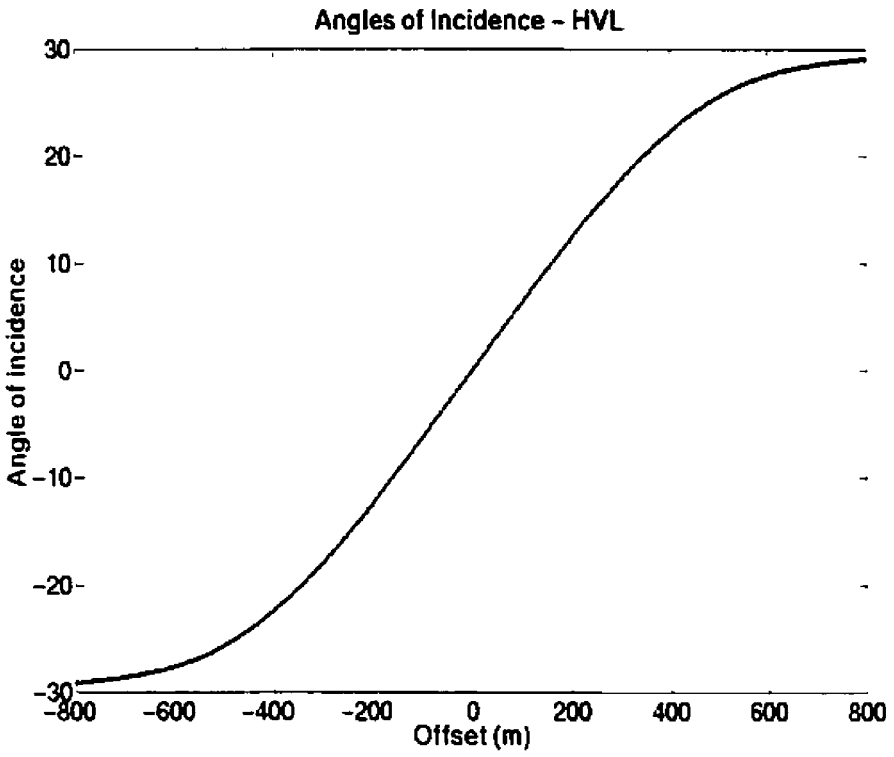

Figure 2.17. Model 3 angles of incidence to the surface for *PS* mode as a function of offset.

2.4.4. Model 4: Dipping reflector without NSL

Dipping geological events are common in settings that have been affected by active tectonics. The geologic model in this case is a dipping reflector without a NSL, illustrated in Figure 2.18. Figure 2.19 illustrates the results of FD modelling and Figure 2.20 shows the result of ray tracing.

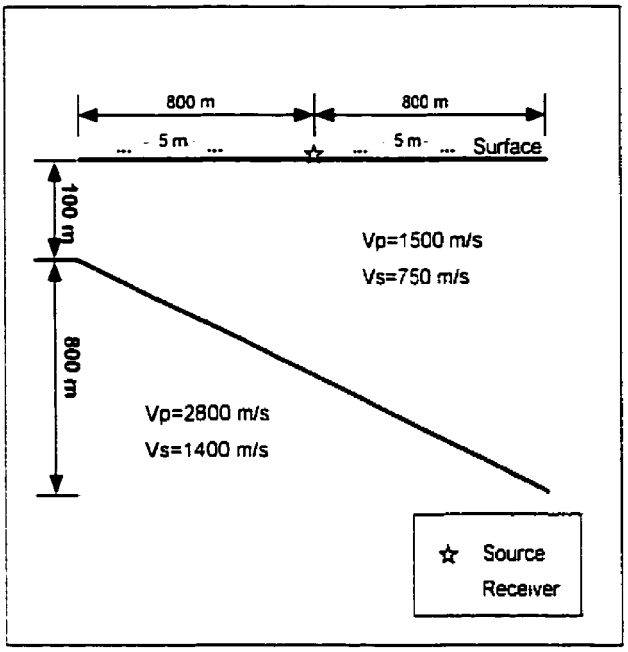

Figure 2.18. Model 4: dipping reflector without a NSL.

Four events result from the dipping reflector, which are labeled in Figure 2.20, as follows:

1. *PP* reflection
2. *SP* converted wave.
3. *PS* converted wave.
4. *SS* reflection.

Phase rotation including polarity change occurs in events related to the *S* wave (Fig. 2.20). Although event 1 does not exhibit that polarity change, there is a phase rotation in the larger negative offsets. The corresponding events can be identified in Figure 2.19. From the FD results, the phase change is clearer in event 4 and subtler in the other events. Mode leakage can be observed in the FD results, like in farther positive offsets of the *PP* horizontal component, and in the corresponding farther offsets of the *PS* wave, vertical component.

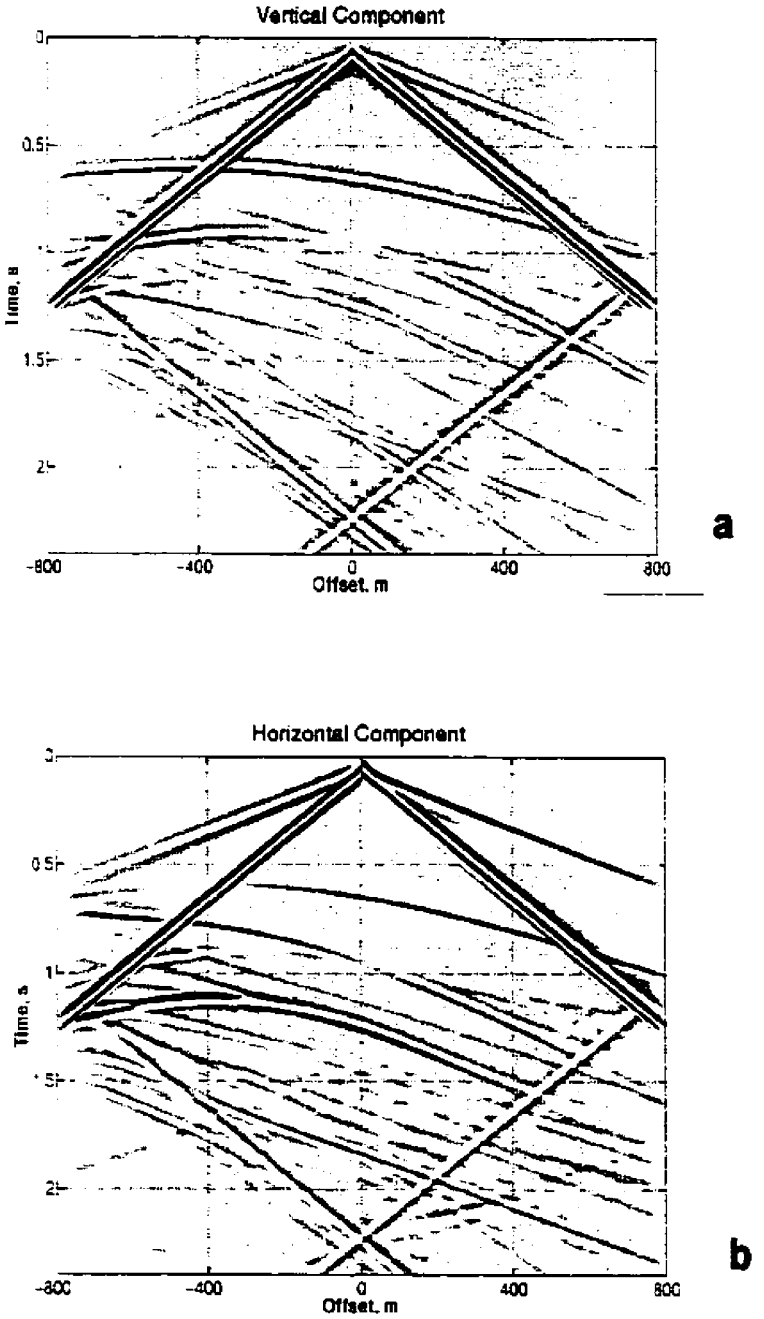

Figure 2.19. Model 4 vertical and horizontal component from FD modelling. (a) Vertical component. (b) horizontal component.

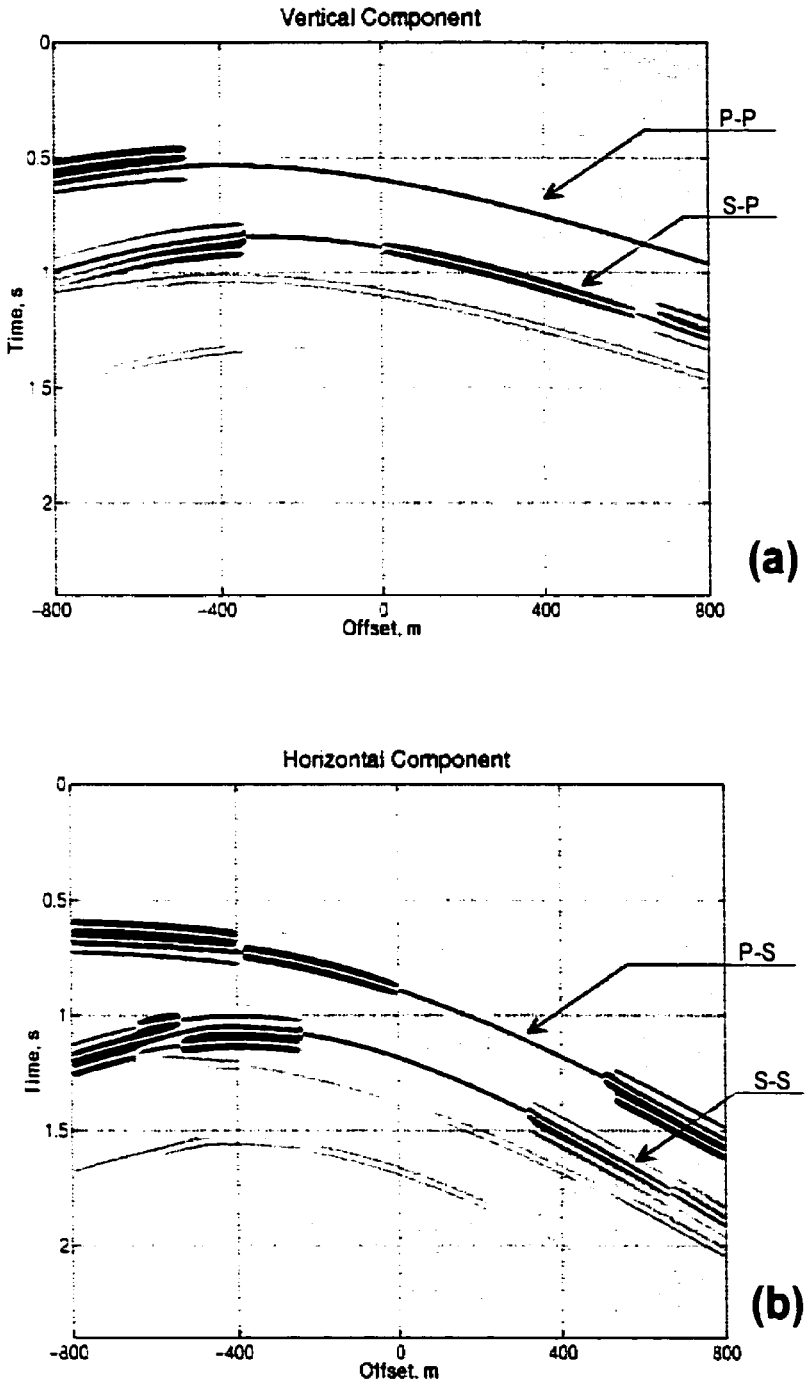

Figure 2.20. Model 4 ray tracing components separated in *P* and *S* wave modes. (a) Vertical component with *P* waves and (b) horizontal components with *S* waves.

2.4.6. Model 5: Dipping reflector with Low Velocity -NSL

This geological model includes a dipping reflector and a LV-NSL, as illustrated in Figure 2.21. Figure 2.22 shows the resulting common shot gathers of the vertical and horizontal components using FD. Figure 2.23 shows the results of ray tracing, separated in *P* waves (vertical component) and *S* waves (horizontal component).

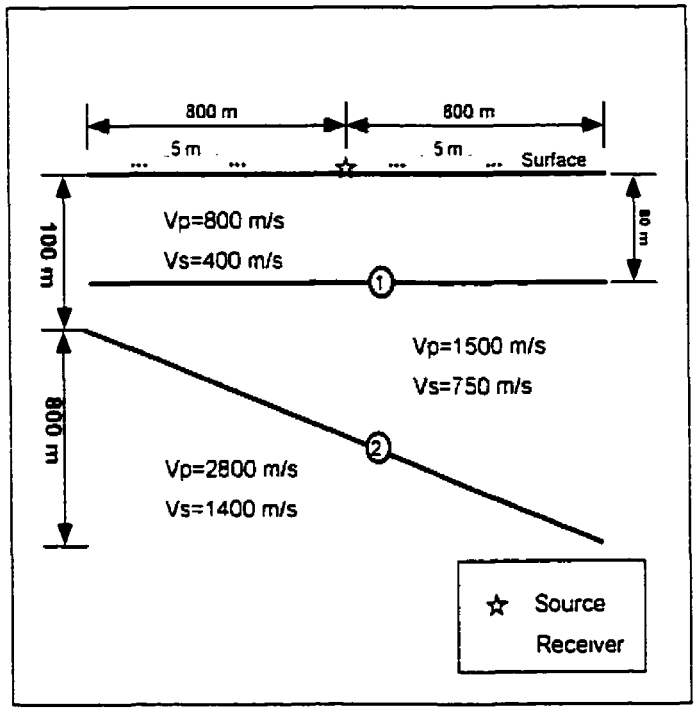

Figure 2.21. Model 5: Dipping reflector with LV-NSL. The reflectors are labeled with numbers.

From the velocities analysis and the arrival times some events are identified and labelled in Figure 2.24, as follows:

1. *PP* reflection from the interface 1.
2. *SP* converted refraction from the interface 1.
3. *PP* from the dipping reflector.
4. *SP* converted reflection from the dipping reflector.
5. *PS* converted wave from the NSL.
6. *SS* refraction from the NSL.

7. *PS* converted reflection from the dipping reflector.

8. *SS* reflection from the dipping reflector.

Events generated at the second interface from ray tracing results (*PP*, *SP*, *PS* and *SS* in Fig. 2.23) resemble the events of Model 4 (Fig. 2.20). From the FD results (Fig. 2.22), there are many events generated by the near-surface layer, which make a difference with model 4 (Fig. 2.19).

Additional events appearing in FD results shown in Figure 2.22 are direct arrivals, refractions, and surface waves. Also strong interfering modes generated at the NSL can be noticed, such as Rayleigh waves, and probably reverberations of refracted *P* and converted waves. Artefacts created by numerical calculations can be observed in Figure 2.22, such as numerical dispersion of surface waves, due to its low apparent velocity, which creates short wavelengths close to the acceptable dispersion limit.

Figure 2.24 illustrates the angles of incidence to the surface for converted *PS* waves generated by the dipping layers of Model 4 and Model 5. In spite of the dipping layer, when a LV-NSL is present the angle of incidence to the surface is less than 25°, then is under the critical angle (Figure 1.4). In a dipping reflector without LV-NSL this angle goes up until 45°, that is, over the critical angle.

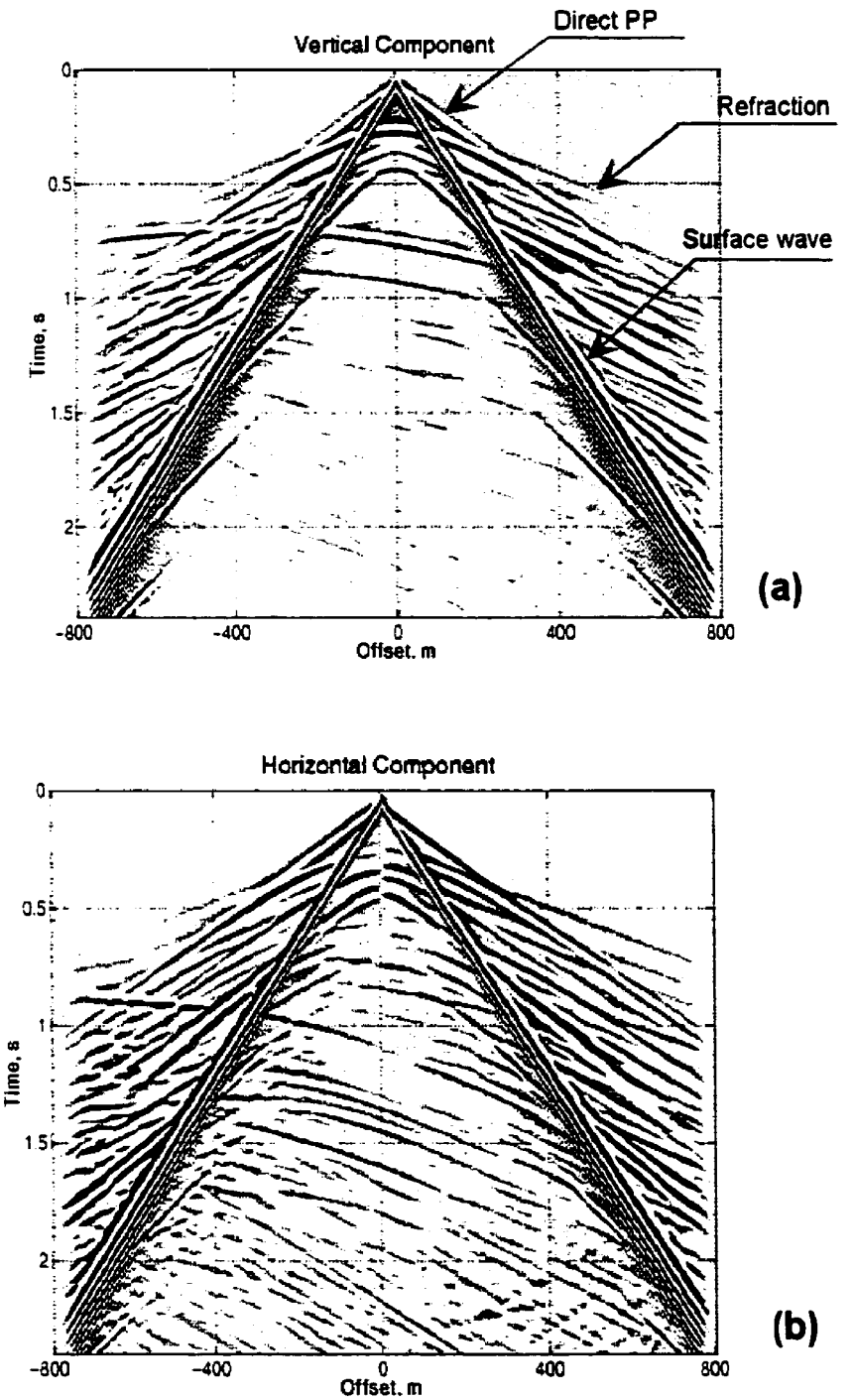

Figure 2.22. Model 5 vertical and horizontal components from FD method modelling. (a) Vertical and (b) horizontal component.

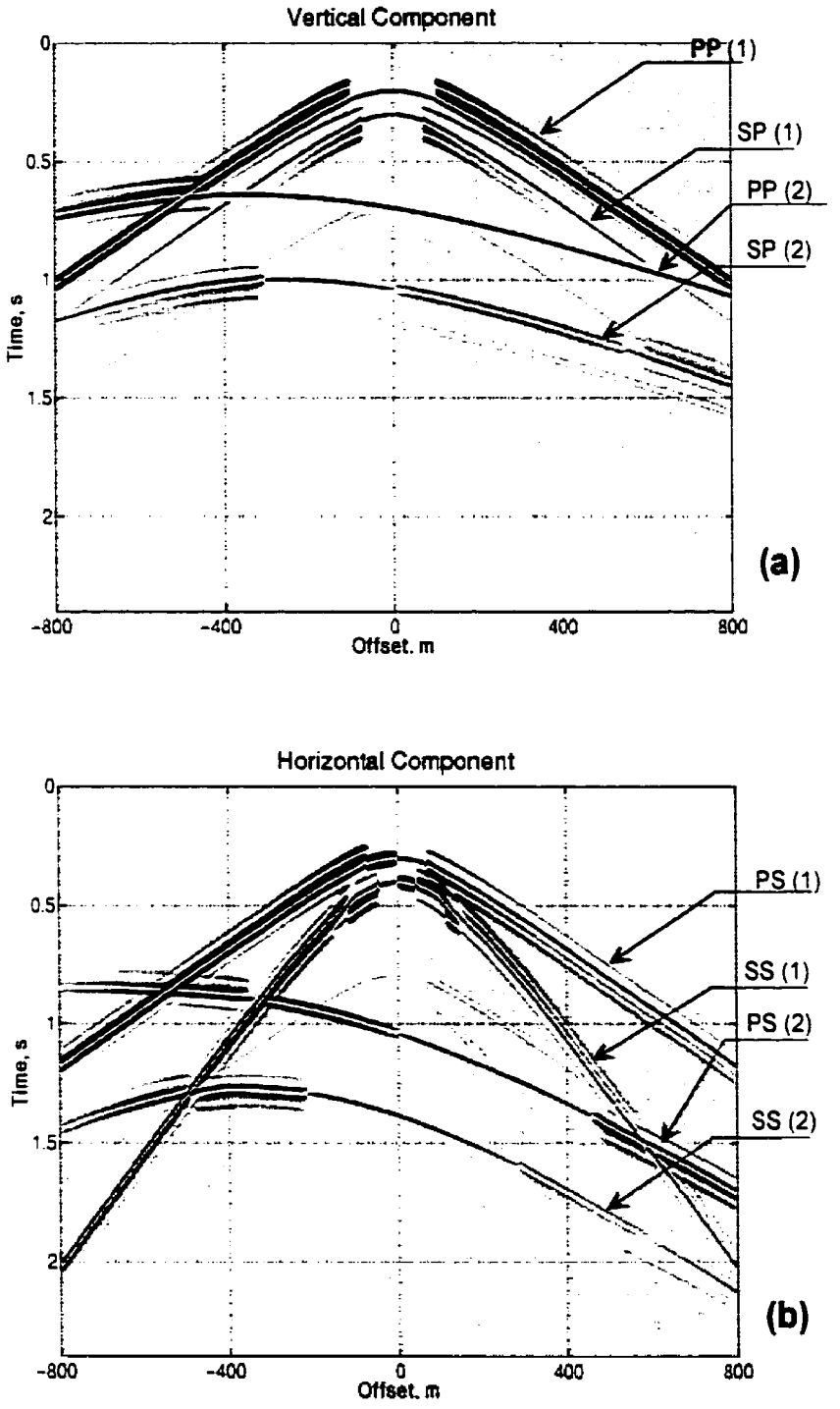

Figure 2.23. Model 5 ray tracing results separated in *P* and *S* wave modes. (a) P waves in the vertical component and (b) S waves in the horizontal component.

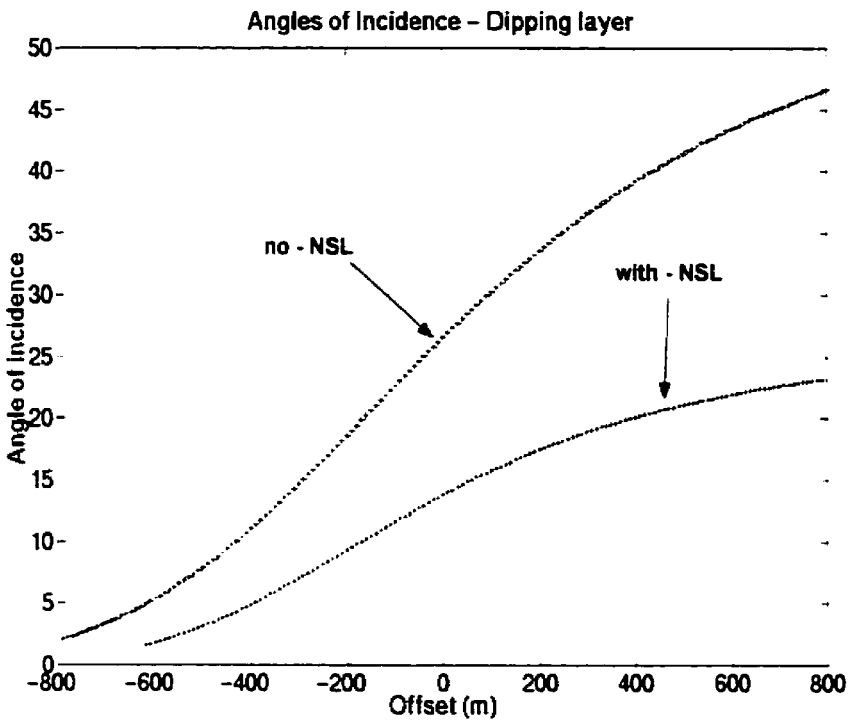

Figure 2.24. Angle of incidence to the surface on dipping layers.

2.5. Discussion and Conclusions

The seismic responses of some simplified geological models of exploration settings were tested in order to study the NSL effect on converted waves. Two seismic modelling methods, namely, finite differencing and ray tracing, were applied to a typical exploration split-spread layout. The geological models basically included plane interfaces, low-velocity NSL's (LV-NSL), high-velocity NSL's (HV-NSL), and dipping interfaces. The main characteristics studied were the free-surface effect, wave-phase changes, events generated at the NSL, and effects of the NSL on amplitude. The following observations are noted:

(1) Phase changes are apparent in ray-tracing results, and more attenuated in finite-difference results, since besides waveform changes as in the later, polarity reversals occur in the former. Phase changes occur at shorter offsets in the presence LV-NSL. These

phase changes appear more related to the critical angle at the reflector than to the free-surface effect. In fact, since the angles of incidence to the surface of *PS* waves were found lower than the critical angle when a LV-NSL is present. Angles of incidence to the surface larger than the critical angle were found only in the case of a dipping layer with no NSL.

(2) In the cases of LV-NSL, the free-surface effect, which includes phase change and mode leakage, is attenuated by the near to vertical incidence of waves. The events generated from Model 2, which includes a complex LV-NSL, appear closer to a real NSL.

(3) In the case of reflections from flat layers, converted *PS* and *SP* waves interfere with one another. In reflections from dipping layers, each mode has different arrival time.

(4) In the case of the HV-NSL (Model 1), the finite-difference result shows mode-converted events and also leakage (both wavemodes in both components). The angles of incidence to the surface of converted waves are relatively high, compared with the LV-NSL or no NSL cases.

(5) In general, at the NSL high-energy events are generated. These events interfere with the reflections of deeper layers and can reduce the amplitudes of these reflections.

The methods and models used have some characteristics and limitations, which have to be taken into account to extrapolate these results to a real setting. The differences in the character of the results obtained from finite differencing and ray tracing are related to the approaches used. Features like spherical spreading and mode conversions after non-vertical incidence, implicit and exact in finite differencing, have to be added in ray tracing. Factors that were not considered in these examples are rough surface, heterogeneous NSL, anisotropic or anelastic properties and higher Vp/Vs ratios.

Low incidences angles to the surface were found associated with LV-NSL's. However, in real data Vp/Vs ratios can be higher than in these examples (section 1.3.2), which implies smaller critical angles. In addition, dipping layer are not rare, offsets are typically larger and targets typically deeper than in the examples herein. Then the resulting polarization

direction and phase can be affected by all these factors and phase changes caused by them cannot be discarded.

CHAPTER 3

POLARIZATION ANALYSIS

3.1. Introduction

As discussed in section 1.2.1. the multicomponent method is able to detect polarization of elastic waves. This property contains potential information about wave modes. anisotropy and. in general. about properties related to the direction. However. the NSL affects polarization and has contributed to prevent a more extended use of this property. In this chapter the general aspects of polarization analysis are presented. The relations between polarization. angle of incidence and amplitude for seismic events on data windows are then analyzed on synthetic and real data. Identification of NSL effects is attempted. A similar analysis is carried out on complete data gathers. where some patterns are identified and polarization filters are tested.

3.2. Wave polarization and the seismic method

Polarization is the path traced by particles under the action of elastic waves. The main attributes of polarization are *shape* and *direction*. The relationship between the angle of incidence and the shape and direction of polarization characterize wave modes (section 1.2.1). In an isotropic homogeneous medium the basic polarization cases are:

1. *P*-wave polarization: linear and in the direction of wave propagation.
2. *S*-wave polarization: linear and perpendicular to wave propagation.
3. Surface (Rayleigh) waves polarization: elliptical and perpendicular to the wave propagation direction.

Considerable research concerning the potential of polarization has been carried out. and methods have been applied principally to earthquake seismology and to VSP (Vertical Seismic Profiling). Significant interest in *S*-wave polarization has increased in exploration. Quoting Douma and Helbig (1987). " *P*-waves are. for all practical purposes. polarised in the direction of the ray. but the shear waves can be polarised in any direction

in the plane that is perpendicular to the direction of the ray. Since information is contained only in non-predictable parameters, it is the shear-wave polarisation information from which we can learn something" (p. 95).

Polarization applications to seismic exploration from the literature are

(1) Separating wave modes (e.g., Flinn, 1965; Esmersoy, 1990).

(2) Obtaining information about anisotropy (e.g., Crampin, 1985)

(3) Filtering of undesired events like ground roll (e.g., Shieh and Herrmann, 1990).

(4) Filtering of out-of-the-plane arrivals (e.g., Perelberg and Hornbostel, 1994; Zheng, 1995).

(5) Obtaining information about the orientation of geophones and the relative location of source and receiver (e.g., DiSiena et al, 1984; Bland and Stewart, 1996).

(6) Obtaining information about the orientation of geologic structures (e.g. Galperin, 1984; Zheng, 1995).

Some drawbacks, in particular the effect of the NSL, have prevented a more extended application of polarization methods to land surface seismic data. The free-surface effect can change the polarity and phase of the events coming from deeper layers (section 1.3.3). Also the typically low velocity of the NSL makes seismic events arrival almost vertical, resulting in a loss of information on direction (Galperin, 1974). An example of these drawbacks, Crampin (1985) considers the free-surface effect a severe limitation for anisotropy analysis using surface data. One explanation for the more effective polarization methods on earthquake seismology and VSP is the reduced effect of the NSL on them: earthquake wavelengths are typically large compared with the NSL thickness, and VSP detects body waves that are affected by the NSL only in the surroundings of the source of energy and not in the receiver.

Another shortcoming founded to use of polarization is the interference between wave modes, which changes the polarization attributes, as illustrated in Esmersoy (1990). Anisotropy and anelasticity, not considered in this thesis, also affects polarization properties, as shown in section 1.2.2.

To highlight the potential application of polarization, two proposed approaches are noted. The first approach is found in Galperin (1984), who developed a *polarization method* for exploration. The other one, a more recent approach, is called *vector processing and interpretation* (e.g., Mueller et al., 1999). Galperin's approach is intended to take advantage simultaneously of the two directivity properties of elastic waves, namely polarization and the direction of propagation, with methods and devices being developed to that end. The *vector processing and interpretation* approach proposes using the complete wavefield, as recorded by the multicomponent method, thereby preserving the directivity properties for interpretation. In this way, benefits could be obtained from all the information pertaining to polarization, notably anisotropy. However Galperin's method is not very popular currently, and very little developments regarding the vector approach has been published yet.

3.3. Overview of polarization analysis techniques

Theoretical work on polarization analysis was first developed for electromagnetic wave theory (e.g. Born and Wolf, 1965). Application of these developments to seismology can be found in Kanasewich (1975) and Samson (1977). Other approaches are intended to solve practical problems, such as polarization filtering and earthquake epicentre location. Some algorithms applied to multicomponent seismic data have been known at least since the 1960's, mainly oriented to earthquake seismology applications.

Macbeth and Crampin (1991) analyze polarization methods applied to anisotropy studies and classify them into four groups: visual inspection methods; particle motion discriminant methods; covariance matrix; and methods that make use of a group of geophones. Hearn and Hendrick (1999) present a review of time-domain single station methods. An overview of the polarization analysis methods roughly based on these works, is presented in the following, and emphasizing among them successful methods or methods that appears to act as meaningful milestones.

Graphical methods are hodograms and stereograms. A hodogram represents particle motion in 2-D. A stereogram is a plane representation of directions in the 3-D space.

Hodograms have been most used in anisotropy analyzes. Galperin (1984) used the stereograms as part of his method.

DiSiena et al. (1984) presented a method based on histograms to extract information about borehole geophones orientation. Alford (1986) introduced a method to analyze anisotropy using polarization of stacked sections and rotating the components to obtain a direction.

Flinn (1965) proposed a covariance matrix algorithm to analyze and filter earthquake multicomponent data in a single-station using a time window. Eigen-analysis of the data in a time window allows obtaining the elipsoid that more closely fits the data. Many variations after this method have been developed. For example. Montalbetti and Kanasewich (1970) propose improvements in the filtering function: Vidale (1988) introduces an instantaneous approach. using the analytic signal: Shieh and Herrmann. (1990) present filtering in the frequency domain. Mercado (1965) proposes a linear polarization filtering method.

The methods listed above assume no interference among seismic events. Some methods directed to this issue have been proposed. such as Esmersoy (1990) and Cho and Spencer (1992).

3.4. Methods applied

Three polarization analysis techniques are used in this thesis. namely the hodograms. the histogram method (DiSiena et al. 1984). and the covariance matrix method (Flinn. 1965). Each one of them is representative of a different approach and is a robust method that has been tested in practical applications. These methods are monochannel. then do not take into account adjacent events. Since each method is independent from another. the results can be validated. Only the covariance matrix method is used in this chapter. and all the three are used in chapter 4. These methods are described in the next section.

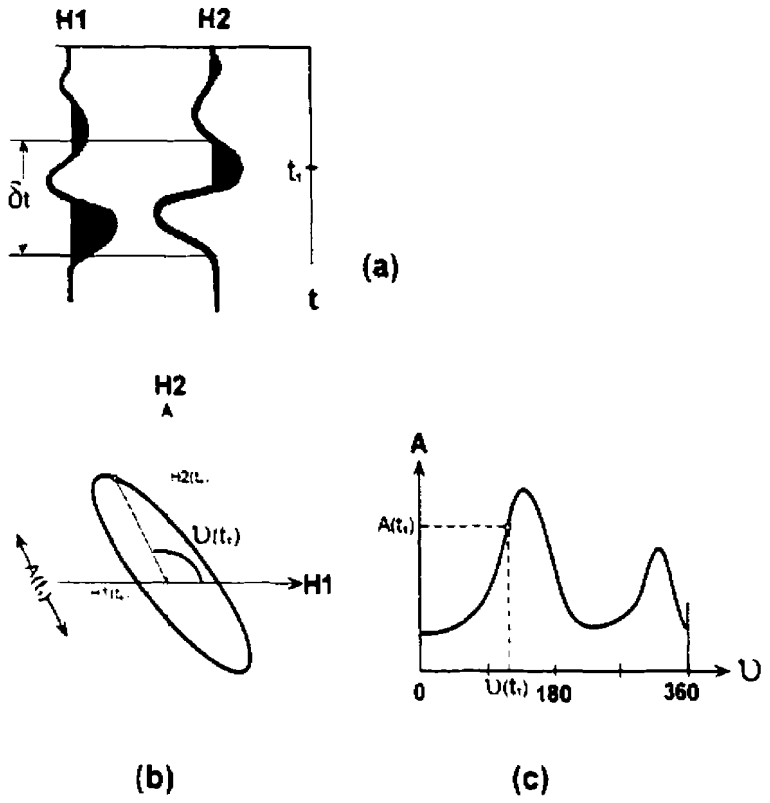

Figure 3.1: Hodogram and histogram polarization analysis methods. (a) A seismic event recorded on two components. H1 and H2: the window used for analysis is δt and an amplitude example is at time t_1. (b) a hodogram plots the trajectory of the particle. which is the resultant of the two components: in this case *H1* is the origin of the angle. *A* is the amplitude and υ is the azimuth: (c) histogram. which has the angle υ in the horizontal axis and the amplitude *A* in the vertical axis.

3.4.1 Hodograms

Winterstein (1990) defines a hodogram as "a graphical display of particle path. often projected into a plane as a crossplot over a chosen time window of two orthogonal components of seismic data". Hodograms. illustrated in Figures 3.1a and 3.1b. are based on the principle that the data recorded by the two orthogonal elements of a multicomponent geophone constitute the components of the particle-trajectory vector. With hodograms it is possible to perform a detailed visual analysis of the polarization

characteristics. better than with other methods. although some subjective judgement is implied.

3.4.2. Histogram algorithm

The particle trajectory on a plane can be represented by the histogram of amplitudes (or energy) as a function of the azimuth. To a certain degree. it is equivalent to a hodogram as illustrated in Figures 3.1b and 3.1c.

The histogram algorithm was developed by DiSiena et al.. (1984) and has been used successfully in VSP to calculate the orientation of geophones. Basically. a calculation of the power as a function of the azimuth angle for a specific time window is carried out. The azimuth origin and direction (clock- or counter-clockwise) may be selected arbitrarily. The hodogram in coordinates H1 and H2 (Figure 3.1(b)) can be written in terms of the amplitude A and the azimuth angle υ as

$$tan(\upsilon(t)) = \frac{H2(t)}{H1(t)} \qquad (3.1)$$

$$A(t) = \sqrt{H1(t)^2 + H2(t)^2} \quad . \qquad (3.2)$$

The angles are then distributed in a number of n bins or *classes*. each one with a width of $360°/n$. From the two components. at each sampling time the angle of the resultant is calculated. according to equation 3.1. Since the angle of the resultant most probably does not coincide with the mean value into a bin. the energy (or amplitude). calculated from equation 3.2. is distributed between the two adjacent bins. proportionally to the difference to the mean value. After the calculation of all the values along the window has been completed. the preferred value of υ defines the angle of direction of the hodogram. υ'.

3.4.3. Covariance matrix algorithm

Flinn (1965) presents a method to analyze and filter polarized waves from earthquakes for single station data. using the covariance matrix. In this method. the trajectory of the particles along a time window is approximated to an ellipsoid. If the ellipticity is high the

ellipsoid is closer to a line, and if the ellipticity is very low the ellipsoid becomes closer to a circle. The orthogonal axes define the shape of the ellipsoid and its direction is the direction of the principal axis. In the simplest case, the components of an ellipse in a 2-D orthogonal coordinate system are two sinusoids and the phase difference between the two sinusoids regulates the grade of ellipticity. Thus if they are in phase, the ellipse is reduced to a line (the highest ellipticity), while if they are 90° out of phase, the ellipse becomes closer to a circle (minimum ellipticity), as illustrated in Figure B.2. More details regarding ellipticity are included in Appendix B. When two or more wave modes interfere, even if the pure modes are linear originally, the shape changes, becoming more or less elliptical, as shown by Zheng (1995).

In two dimensions, given the two components $H_1(t)$, and $H_2(t)$, the covariance matrix is

$$\underline{\underline{C}} = \begin{bmatrix} \mathrm{var}(H_1) & \mathrm{cov}(H_1, H_2) \\ \mathrm{cov}(H_2, H_1) & \mathrm{var}(H_2) \end{bmatrix} \qquad (3.3)$$

where

$$\mathrm{cov}(H_i, H_j) = \frac{1}{N}\sum_{n=1}^{N}[H_i(n) - \mu_i][H_j(n) - \mu_j] \qquad (3.4)$$

$N \equiv$ the number of samples,

$\mu_i \equiv$ the mean of the variable i.

and

$$\mathrm{var}(H_i) = \mathrm{cov}(H_i, H_i) \quad .$$

The diagonalization of the matrix (eigenanalysis) defines the ellipsoid parameters (Appendix B). The ellipticity is given by the eigenvalues, since each one defines one of the main axes of the ellipsoid, and the eigenvectors provide information about the direction of each axis.

If λ_1 is the larger eigenvalue and λ_2 the second larger, the ratio λ_2/λ_1 gives the circularity of the data. The linearity, factor *f1*, can be defined therefore as the inverse of the circularity,

$$f1 = 1 - \frac{\lambda_2}{\lambda_1} \quad . \qquad (3.5)$$

If *f1* is one, the polarization is linear, and if it is zero the polarization is circular.

Flinn (1965) also proposes a filtering method using the covariance matrix approach. If $\vec{d}$ is a vector with a desired direction and $\vec{e}1$ is the eigenvector corresponding to the largest eigenvalue, then a parameter *f2* can be defined,

$$f2 = \vec{e}1 \cdot \vec{d} \qquad (3.6)$$

This parameter measures the difference between the calculated and the desired direction. The gain factor to filter linearly polarized data in the desired direction is

$$f = f1f2 . \qquad (3.7)$$

As indicated in Section 3.3, a variety of methods have been developed after this method.

3.5. Polarization analysis of seismic events

A methodology for the analysis of seismic events using the covariance matrix method is applied in this chapter. This part of the thesis is inspired by Hamarbitan and Margrave (1996). The following analysis, carried out on shot gathers, relates incidence angle, polarization angle and amplitude.

The covariance matrix method is applied to shot gathers of synthetic and real data. Windows for analysis are defined on the shot gathers, with each one tracking a single event that can be recognised visually. Also, the information regarding angle of incidence and the amplitude is used, the angle of incidence having been calculated using the plane wave approximation (Appendix A). The results are presented graphically (e.g. Figure

3.3), which has three parts: (a) the linearity; (b) the incidence and polarization angles; and (c) the amplitudes, all of them as a function of the offset.

The covariance algorithm was adapted to give polarization angles between –90° and 90° with respect to the vertical axis, which makes easier to relate these angles to the incidence angle.

In the following section, a synthetic data set, created with the Finite Difference Method (FDM), and a real shot gather are analyzed using polarization.

3.5.1. Synthetic data analysis

The following analysis uses the two components, vertical and horizontal, that result from Model 1 FD method (chapter 2). Figure 3.2 illustrates the vertical component and includes three windows on the events to be analyzed.

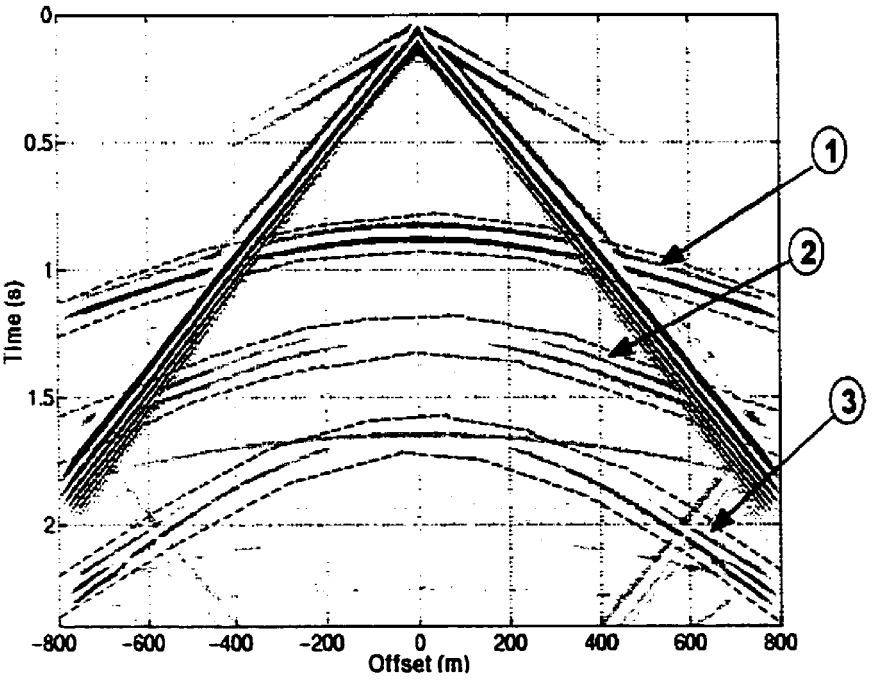

Figure 3.2. Model 1 shot gather with the polarization analysis windows. The gather corresponds to the vertical component. The windows are identified numerically.

Figure 3.3 shows the results for Window 1. Four regions can be identified in this figure: region *A* at an offset lesser than 400 m, region *B* at an offsets 350 to 450 approximately, region *C* at 450 m, and region *D* after 450 m (Fig. 3.3). The linearity of Region *A* is close to one and its angle of polarization coincides with its angle of incidence. These features correspond to a *P*-wave reflection. The parameters that region *B* have linearity close to 0.8, angle of polarization 5°, and an amplitude much larger than in zone *A* (Fig. 3.3c). This event corresponds to Rayleigh waves, (as can be verified in Figures 3.2 and 2.3). Region *C* shows low linearity (around 0.4), and polarization seems with different direction to wave propagation. Most probably the latter is the result of *S* direct waves interfering with surface waves (see snapshot in Fig. 2.4).

Figure 3.4 shows the polarization analysis of Window 2. The two main regions identified are labelled with letters: region *A* from offset 0 to 500 m, and region *B* beyond offset 500 m. The linearity of event *A* is almost one. The polarization angle does not correspond to *P* wave (incidence angle) or *S* wave (90° to incidence angle), however is closer to the later. In fact, this event is a mixing of converted waves, *P* to *S* and *S* to *P*, where *PS* mode prevails, as shown in Figure 2.7c. The change at far offsets in region *A* of the polarization angle and linearity are explained by the critical angles for *SP* and *PS* waves about 375 m (see section 2.4.1 and Figure 2.8). In region *B* linearity around 0.8 and high amplitude correspond to Rayleigh waves, as confirmed by the shot gather (Figure 3.2).

Figure 3.5 shows the polarization analysis of Window 3. Four regions are identified, and also lettered. Region *A* shows characteristics of a *P* wave at zero offset, namely high linearity and polarization in the direction of wave propagation. This corresponds to a multiple of the *P* wave reflection, which is mixed with other events at farther offsets. Region *B* appears to be related to interference between pure shear wave (*SS*) and the *P*-wave multiple, since the linearity is low and the polarization is not in the wave propagation direction or orthogonal to it. A decrease in amplitude near to 200 m offset can be related to the critical angle of the *S* wave (see Fig. 2.8 in section 2.4.1). Region *C* most probably corresponds to a pure *S* wave, since the linearity is one and polarization appears to be perpendicular to the angle of incidence. Region *D* shows variable amplitude

and low linearity. From the free-surface response, the critical angle of incidence to the surface for this event is 30° (see Fig. 1.4), which corresponds to an offset of 462 m. Interfering boundary reflections can be observed at about 600 m (see Fig. 3.2), which relates to the low linearity in Figure 3.5a at the same offset.

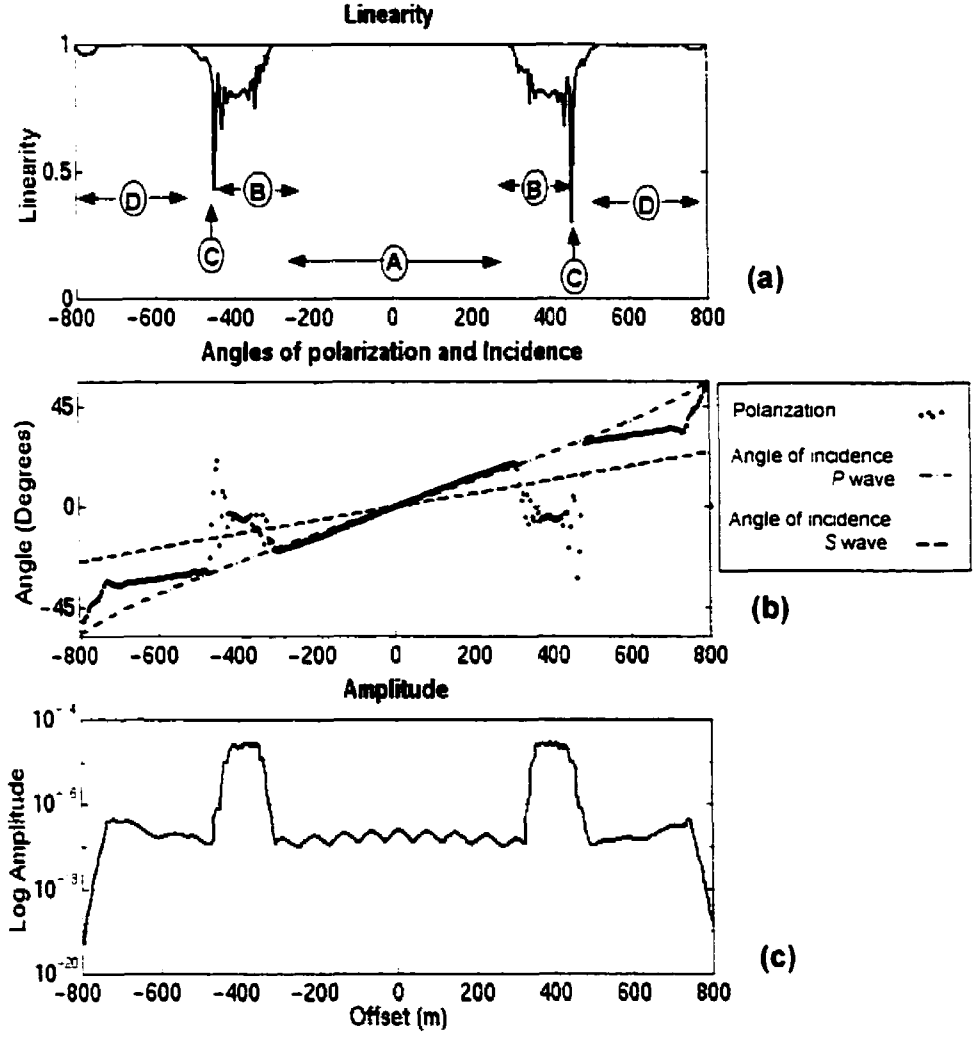

Figure 3.3. Polarization analysis of window 1, Model 1. (a) Linearity, (b) angles of polarization and incidence, (c) amplitude. Four zones can be distinguished: Zone A corresponds to *P* wave, zone B to surface waves, zone C to direct *S* arrival and zone D to *P* wave after the critical angle.

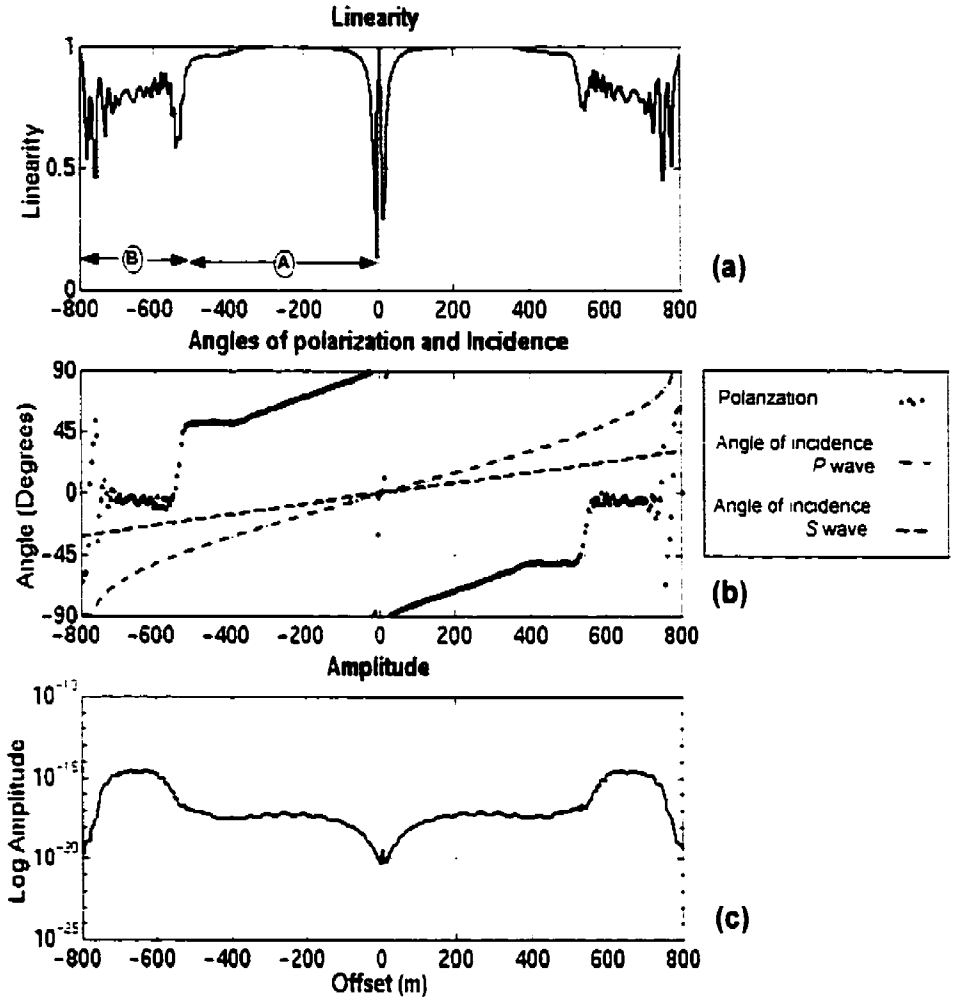

Figure 3.4. Polarization analysis of window 2. Model 1. (a) Linearity: (b) angles of polarization and incidence. (c) amplitude. Two regions can be distinguished: region *A* where a mixture of *PS* and *SP* converted waves predominates. and region *B* which exhibits predominance of Rayleigh waves.

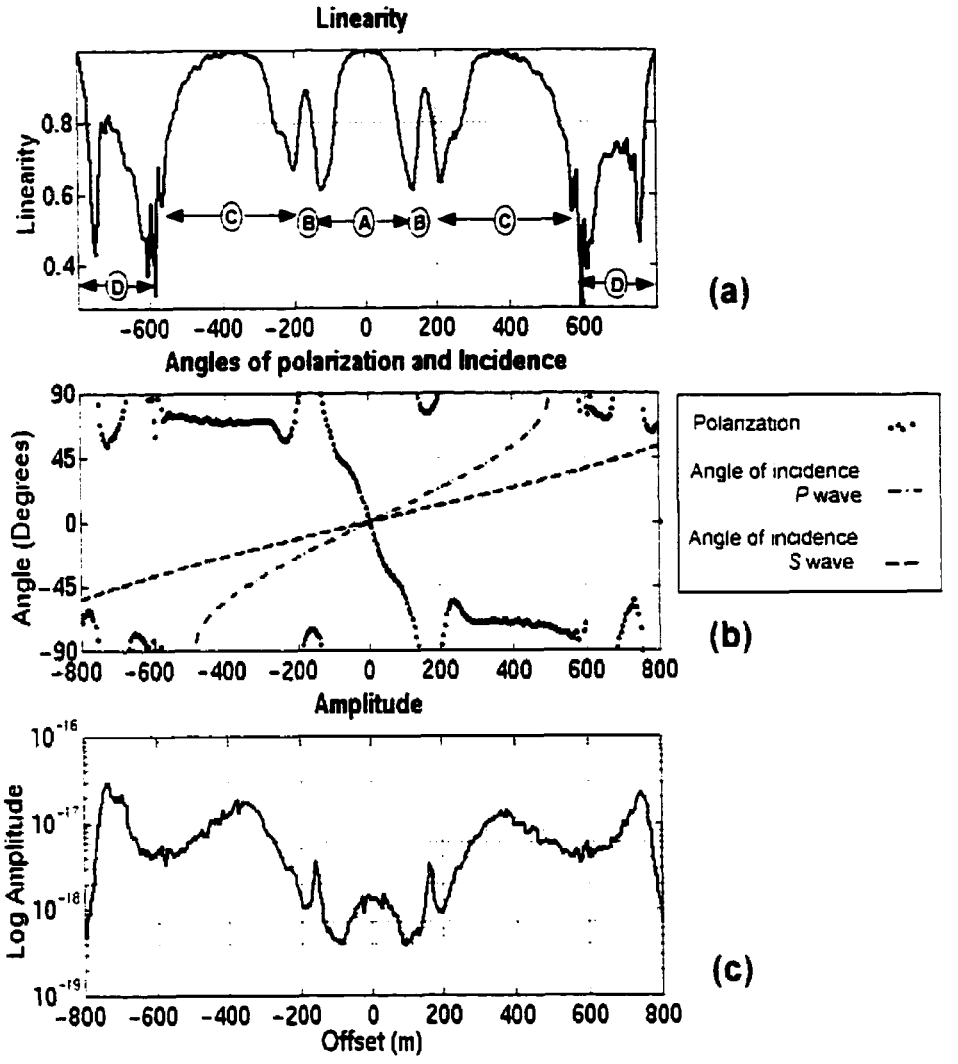

Figure 3.5. Polarization analysis of Window 3, Model 1: (a) Linearity: (b) angles of polarization and incidence: (c) amplitude. Four regions are identified. Region *A* corresponds to a *P*-wave reflection multiple: region *B* to interfering *P* and *S*-waves: region *C* pure *S* wave reflections predominate: in region D there are interfering boundary reflections and probably a free-surface effect.

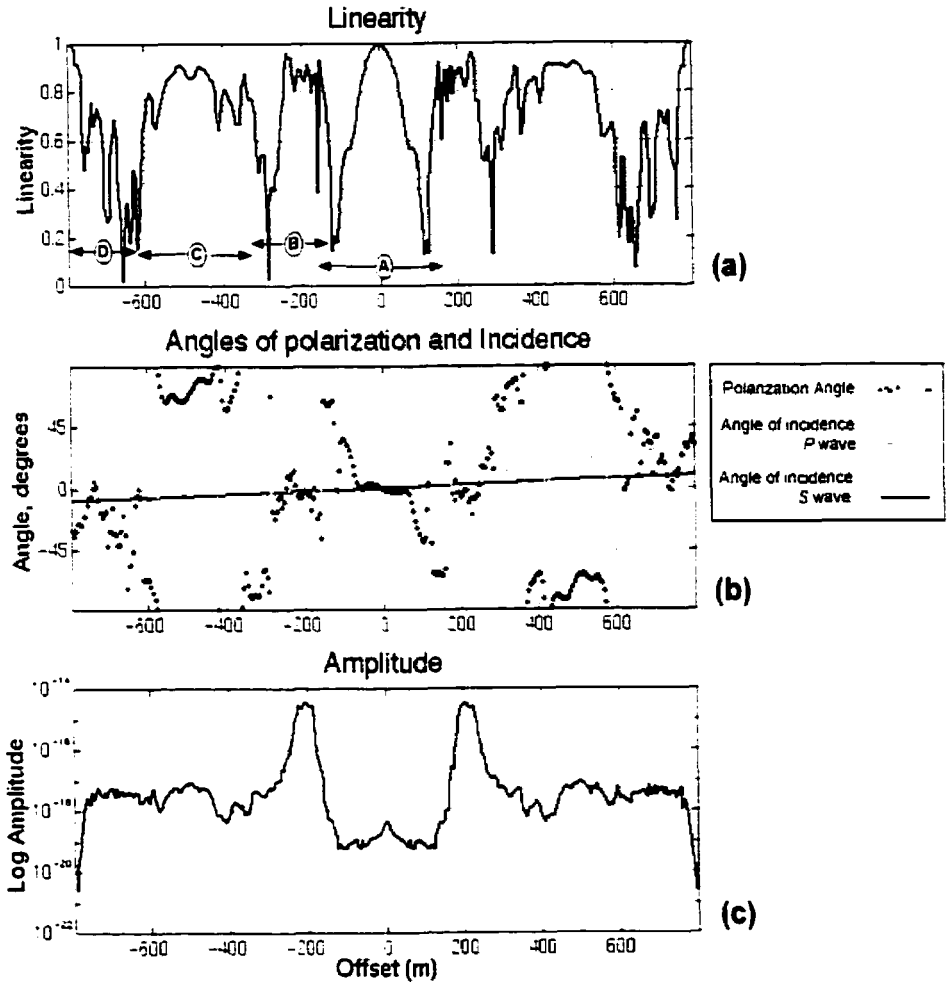

Figure 3.6. Polarization analysis of a window corresponding to *PS* and *SP* mode arrivals. Model 2: (a) Linearity: (b) angles of polarization and incidence: (c) amplitude. Four regions are identified. Region *A* corresponds to *P*-wave event: in region *B* the surface wave predominates: in region *C PS* wave reflections predominates: in region D interfering modes occur, which probably are *P*-wave multiples from the NSL.

Figure 3.6 is the polarization analysis of converted waves from the Model 2 FD results (section 2.4.2 and Figure 2.10). This event is generated at the interface 6 (see Figure 2.9). As shown in Figure 2.12, *PS*- and *SP*- modes interfere because they arrive simultaneously. Four regions can be distinguished in this case lettered in Fig. 3.6a.

Region *A* shows characteristics of a *P* wave at zero offset and interference among modes (low linearity) at larger offsets. Region *B* reveals strong effect of surface waves. In region *C* prevail converted waves, with stronger *PS* waves (after the critical angle, according Figure 2.13). In region *D* prevail other interfering events, probably *P* wave reverberations (see Figure 2.10). Notice that region *C* is the only one that predominates converted wave features.

3.5.2. Real data analysis

A real data shot gather from the Blackfoot III seismic survey is analyzed using the same methodology. This experimental 3C-2D survey was recorded in 1997 in the Blackfoot area (Alberta, Canada), by the CREWES Project (University of Calgary) in an integrated University-Industry effort. Different recording configurations were used along a 3 Km seismic line. More details can be found in Hoffe et al. 1998. A shot of this line, where the geophone spacing was 20 m, is analyzed in this section.

Figure 3.7 illustrates the vertical and radial components. Three events were selected to be analyzed. Their corresponding windows are identified numerically in Figure 3.7b. Events 1 and 2 are easier to identify on the vertical component, and event 3 can be more easily distinguished on the horizontal component.

An analysis of Window 1 (first breaks) is presented in Figure 3.8. The linearity is high along the gather and the angle of polarization is close to the angle of incidence. These characteristics correspond to a *P*-wave, which can be expected for first arrivals. At very short offset the linearity is lower and the polarization angle appears to be different from the incidence angle: these features can be related to other wave-mode interfering, such as direct arrivals and surface waves. Note that, as a difference with the synthetic data analyzed, the amplitude decreases with offset (Figure 3.8c).

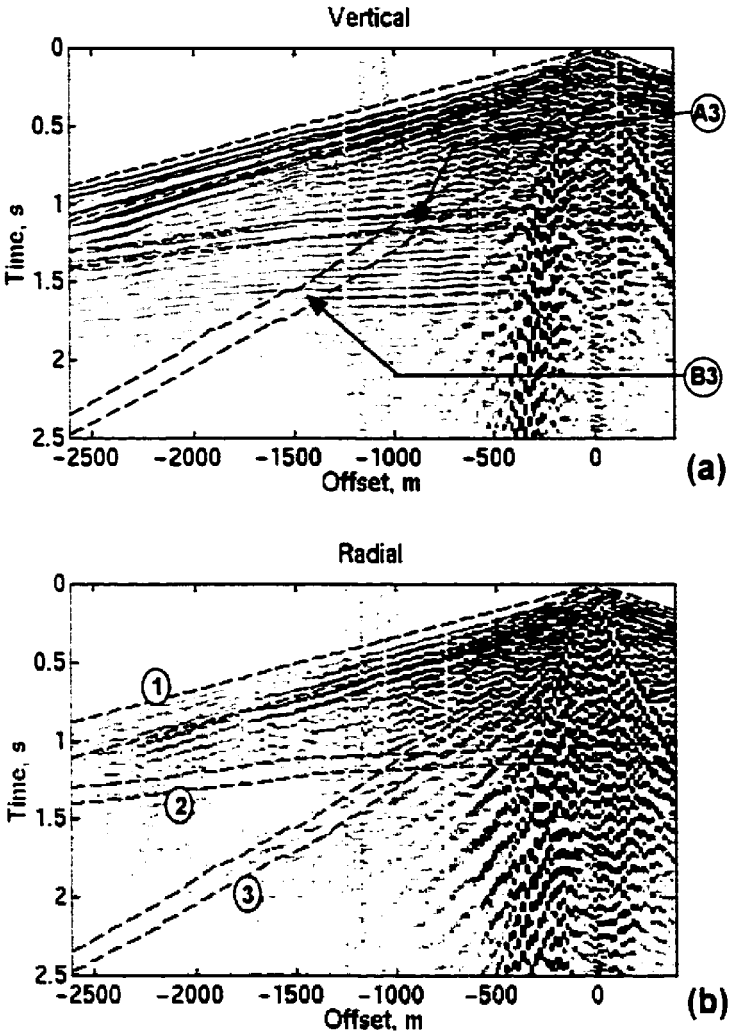

Figure 3.7. Components of the real data with analysis windows: (a) vertical component: (b) horizontal component. The analysis windows are marked with numbers in (b). The letters in (a) indicate interference between modes, as illustrated in Figure 3.9.

The analysis of window 2 is shown in Figure 3.9. Four regions can be distinguished, identified by letters in 3.9a. Region *A* shows relatively high linearity, apparent polarization close to normal to the incidence angle, and high amplitude. Region *B* shows low linearity, polarization almost in the direction of wave arrival and larger amplitude. These characteristics correspond to surface waves. Region *C* shows variable properties of

linearity and polarization angle, and low amplitude and appears to be a mix of *S* and *P* waves. In region *D* the linearity is closer to one and the polarization direction is very close to the arrival direction, which suggests a *P* wave reflection. This event acted as a guide in the selection of this window (see Figure 3.7).

Figure 3.10 is the analysis of Window 3. In this window the linearity and angle of polarization are variable, although the polarization angle tends to be perpendicular to the incidence angle. Some offsets with low linearity can be related to the interference between events that can be identified in the vertical or in the horizontal components. This is the case in the events identified as *A3* and *B3* in Figure 3.10, and in the shot components shown in Figure 3.7b, which have a polarization angle that is close to the incidence angle. The polarization angle can be considered approximately orthogonal to the incidence angle, which confirms the interpretation of this event as an *S* wave, as is suggested by the event picked on the horizontal component (Figure 3.7b).

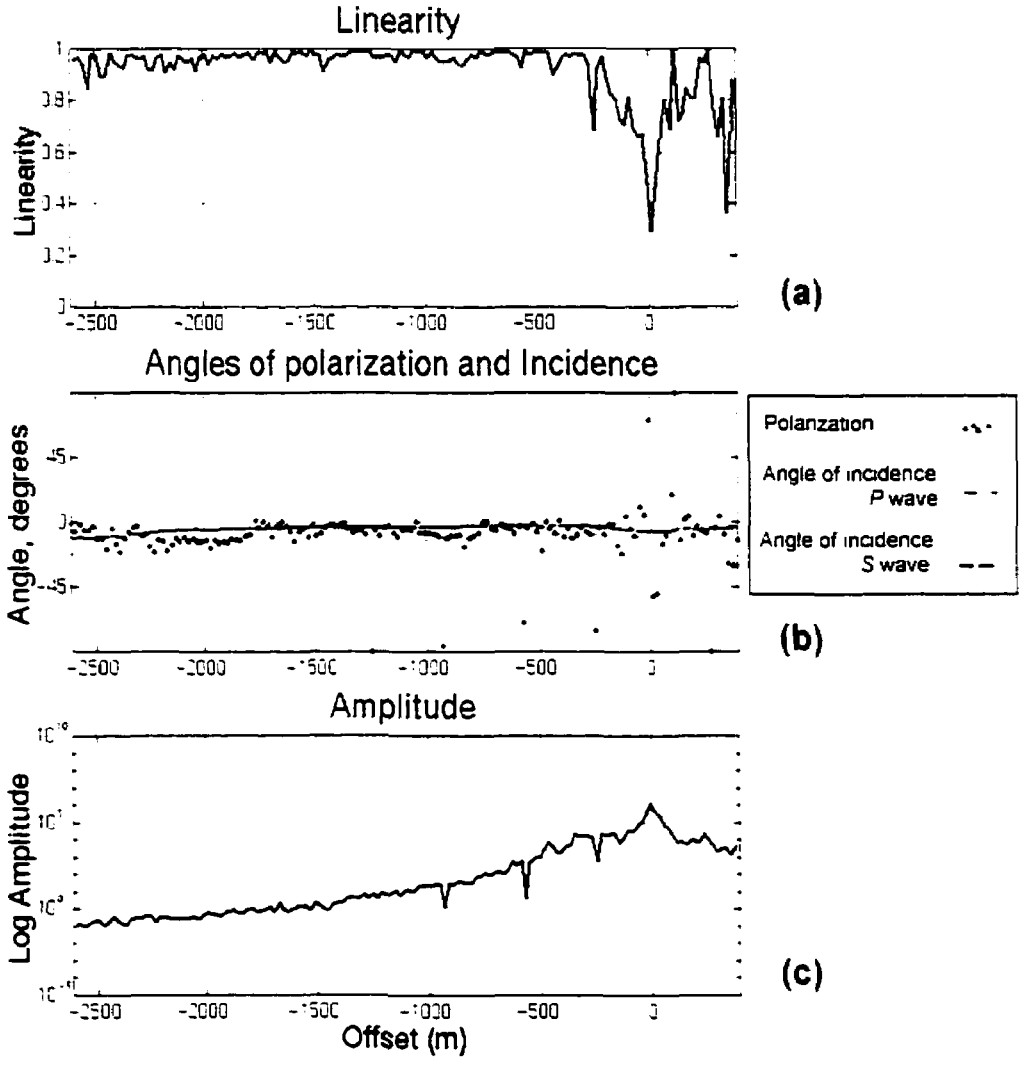

Figure 3.8. Polarization analysis of Window 1 in real data: (a) Linearity: (b) angles of polarization and incidence: (c) amplitude. The linearity is high, and the angle of polarization is close to the angle of incidence, which agrees with the identification of this event as a *P*-wave refraction.

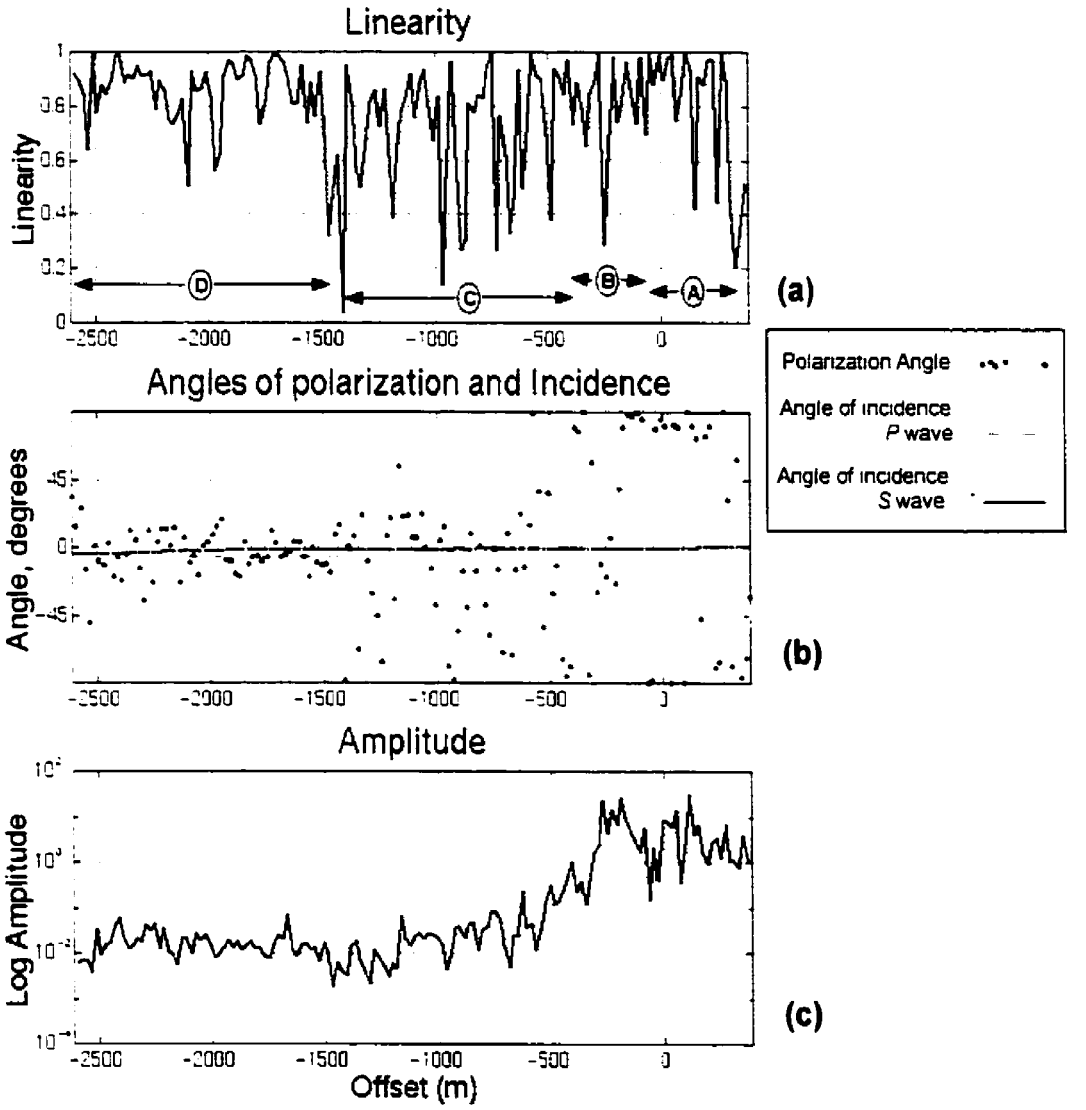

Figure 3.9. Analysis of Window 2 of the real data: (a) Linearity: (b) angles of polarization and incidence: (c) amplitude. Four regions are differentiated, labeled with letters in (a). In *A*, *S* waves seems to predominate: surface waves predominate in *B*: in *C*, mixed *P* and *S* waves: in *D*, *P*-wave reflections.

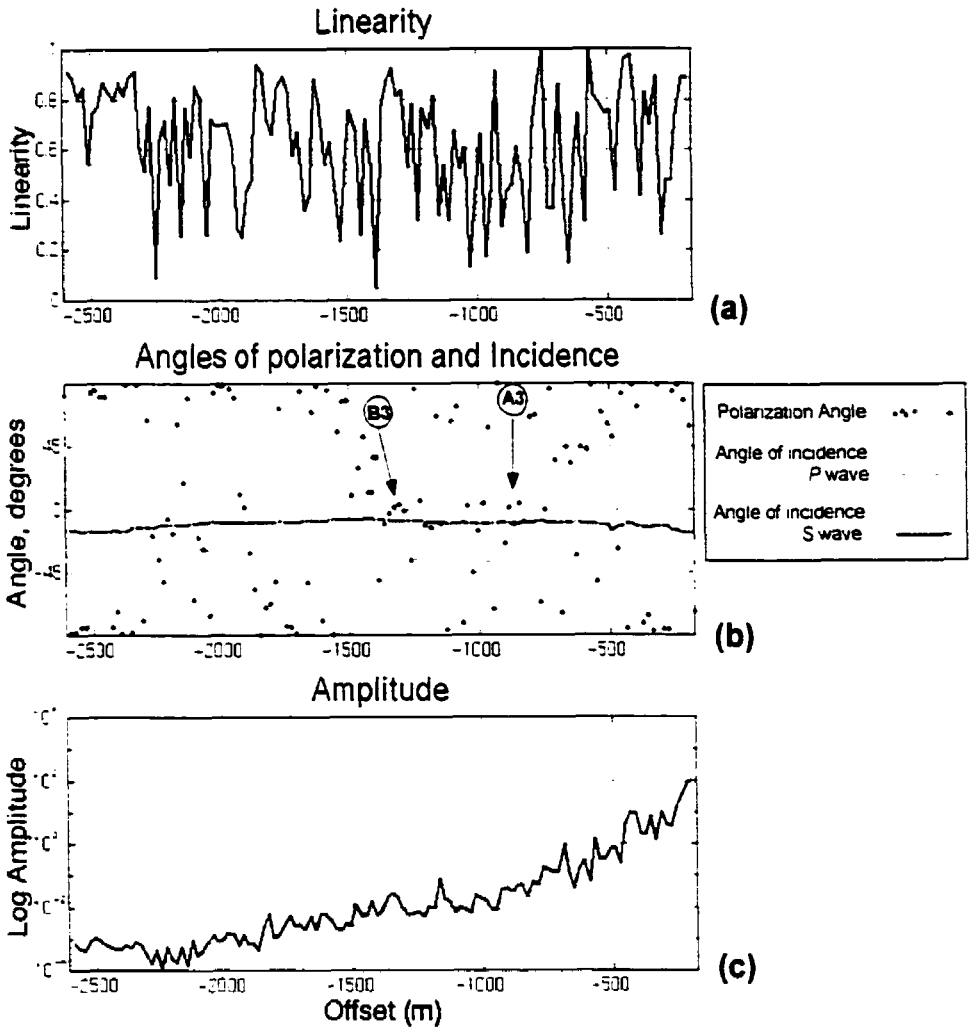

Figure 3.10. Analysis of Window 3. (a) Linearity, (b) angles of polarization and incidence, (c) amplitude. The angle of polarization shows characteristics of an *S* wave.

3.6. Polarization analysis and filtering of data gathers

The complete synthetic and real data sets are analyzed in the following section using the covariance matrix method, with a sliding window of 100 ms.

Figure 3.11 shows the analysis of the synthetic data in Figure 3.2, taken from Model 1. Figure 3.11.a shows the resulting polarization angles and Figure 3.11b shows the

linearity. Linearity values rank from 0 to 1 and polarization angles from -90° to 90°. as shown by the scale bars on the right hand side. The windows corresponding to the analysis carried out in Section 3.5.1 are also indicated. A comparison of these results with the results from Section 3.5.1 shows close similarities. Event 1 shows a linearity of one. except at the surface wave locations. and a polarization angle that is close to zero. Event 2 shows opposite polarities at each side of the shot and a polarization angle that is close to 90°.

Figure 3.12 shows the analysis of the real data gather of Figure 3.7. Blackfoot III. Figure 3.12a shows the polarization angles and Figure 3.12b the linearity. As in Figure 3.11. The scale. in the bars of the right-hand side. show linearity from 0 to 1 and a polarization angle from 0° to 90°. Event 1. corresponding to first arrivals. is well defined. with linearity close to one and a polarization angle close to zero. Event 2 has a polarization angle close to 0. linearity close to 1 in the far offset. and an angle close to 90° in the shorter offset. Event 3 has a polarization angle close to 90° and variable linearity. Labels *A3* and *B3* in Figure 3.12.a indicate the location of the interfering events (see Figures 3.7a and 3.10b). Letter *C* indicates an event with low polarization angle. which may correspond to event *B* in Figure 3.9. identified as surface waves. Letter *D* shows high linearity and polarization angle close to 90°. which would correspond to *S* waves with low velocity or *P*-direct arrivals.

Results of application of the polarization filter proposed by Flinn (1965). as described in section 3.4.3 are in Figures 3.13 to 3.15. This filter is basically an amplitude gain factor. the dot product of the desired direction with the polarization of each event. A data window on an event of interest is defined. and then the angles of incidence to the surface and the desired polarization angle are calculated.

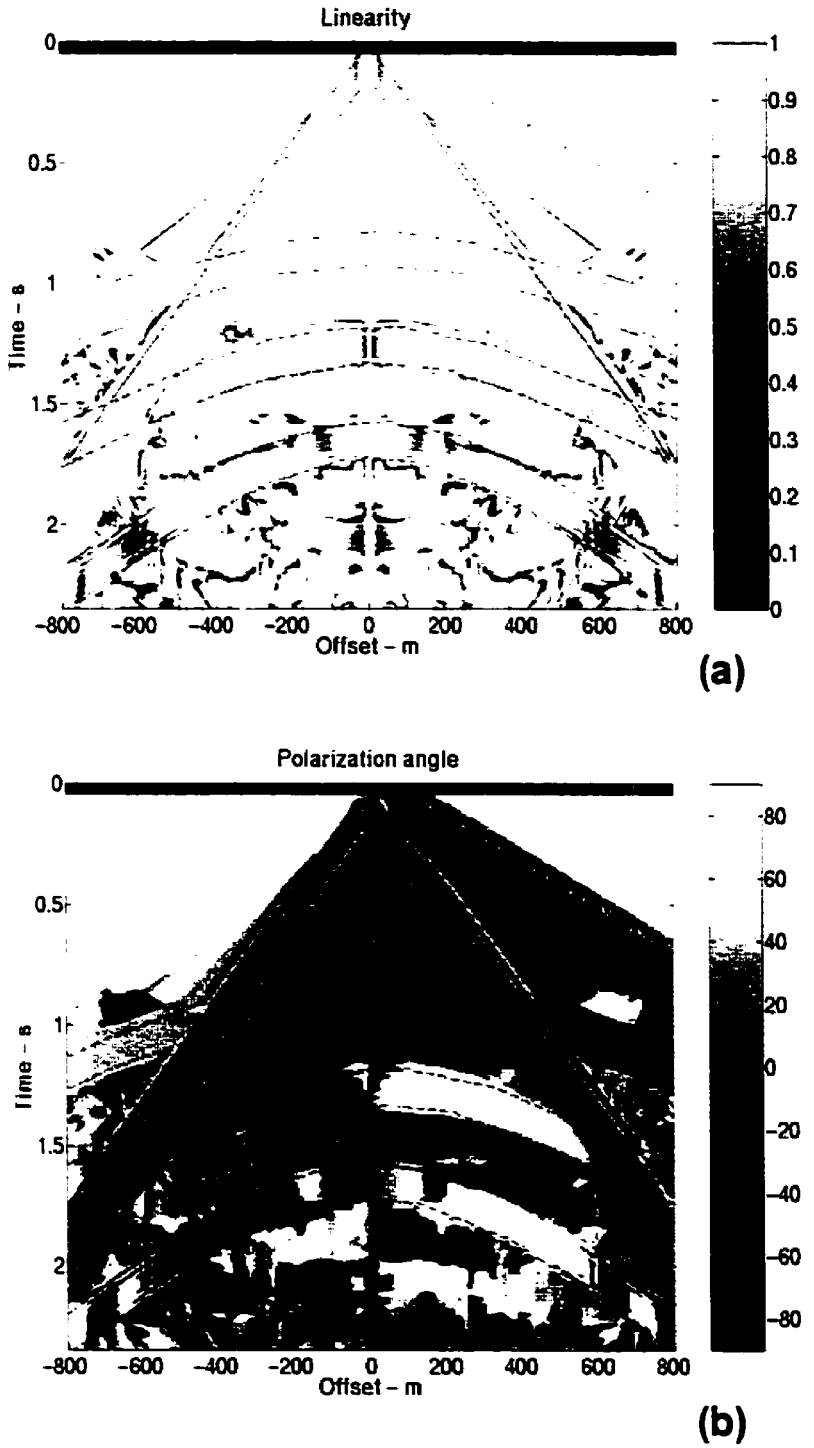

Figure 3.11. Polarization analyzes of the synthetic gather. using vertical and horizontal components. (a) linearity. (b) polarization angle. In the right side the scale bars. The windows correspond to the analyzes in Figures 3.2 to 3.5.

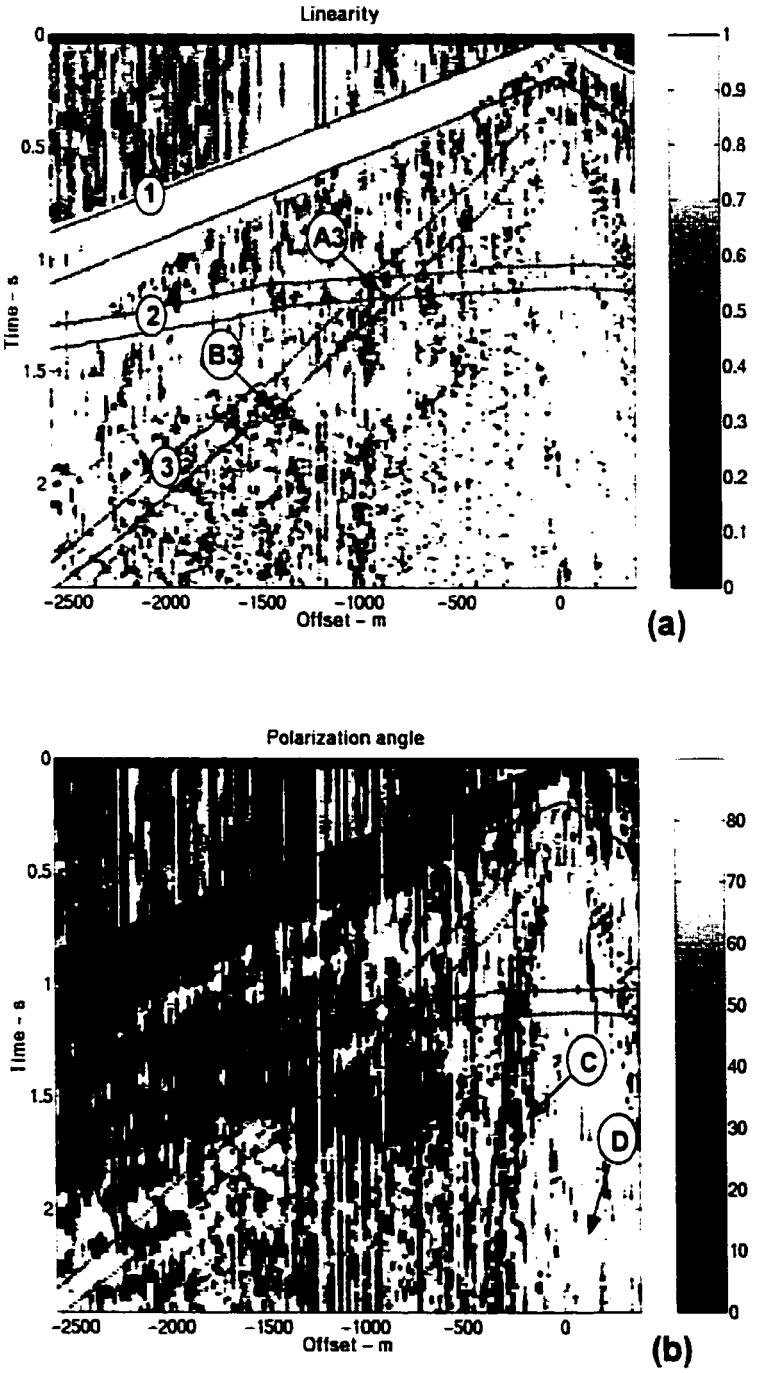

Figure 3.12. Polarization analyzes of the real data gather. In the right side the scale bars. The windows correspond to the analyzes in Figures 3.7 to 3.10. *A3* and *B3* correspond to the same events in Fig. 3.10b. *C* is an event with almost vertical polarization identified as surface waves in Fig. 3.9b.

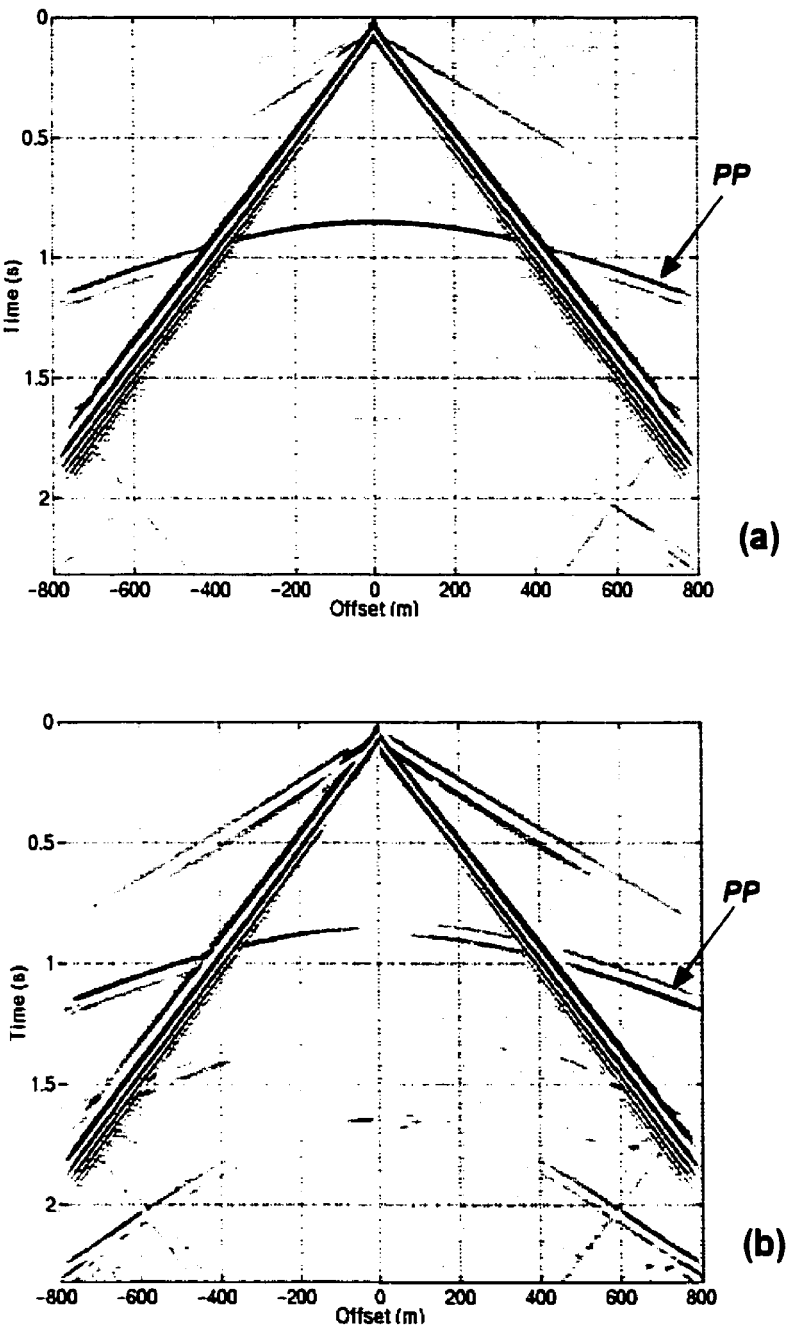

Figure 3.13. Polarization filtering of PP reflections on the synthetic data of Model 1. (a) The vertical component, (b) the horizontal component. Note enhancement of this event when compared with Figure 2.3.

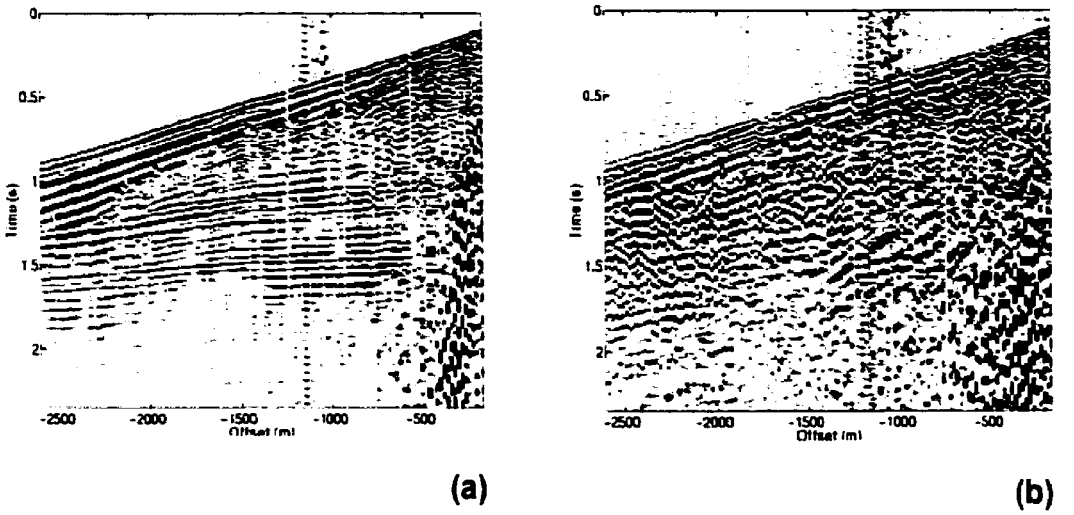

Figure 3.14. Polarization filtering of the real data from Blackfoot III. The parameters of Window 2 were selected for this filtering. (a) Vertical component. (b) Horizontal component. Compare with Figure 3.7.

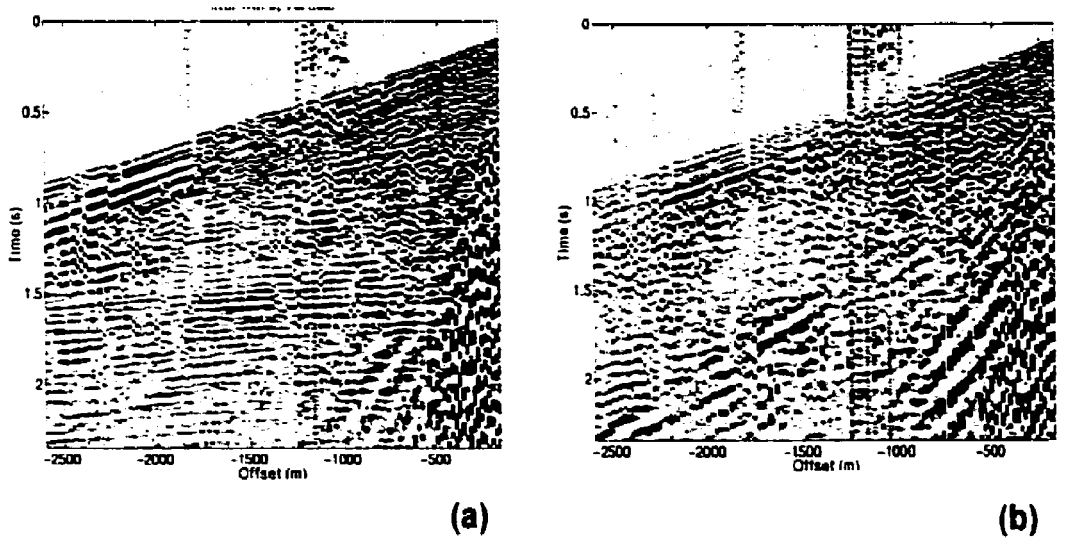

Figure 3.15. Polarization filtering of the real data from Blackfoot III. The parameters of Window 3 were selected for this filtering. (a) Vertical component. (b) Horizontal component. Compare with Figure 3.7.

In Figure 3.13 are the results of filtering applied to the event in Window 1 of Figure 3.2. with polarization in the direction of the *P*-wave incidence angle. Compare with Figure 2.3 that has the same gain. Figures 3.14 and 3.15 show the result of application of the filter to the Blackfoot III data. To calculate the wave arrival direction the plane wave approximation was used with velocities of the NSL calculated from the statics solution. Details of these velocities are shown in Chapter 5, Section 5.4.1.Figure 3.14 is the result of Window 2 filtering,. considered a *P* wave (Figure 3.7), assuming polarization in direction of the wave arrival. Figure 3.15 is the result of Window 3 (Figure 3.7) filtering with polarization perpendicular to the wave incidence.

3.7. Conclusions

In this chapter, polarization analysis using the covariance matrix method has been applied to synthetic and real multicomponent data. The method was applied to windows on the synthetic models 1 and 2 (Chapter 2), to the real data of an experimental 3C-2D survey, Blackfoot III, and to analysis and filtering of complete gathers. Some remarks are:

(1) Polarization analysis in synthetic data confirms the theoretical expectations about pure and converted wave directions. However interference between wave modes is present even in the very simple synthetic, and stronger with complex NSL (Model 2).
(2) Meaningful interpretation of polarization analysis is also obtained from real data. However stronger interference, 3-D effects or anisotropy may affect these data.
(3) It is difficult to identify more subtle details such as precise direction angles or phase changes. Consequently the results obtained are more qualitative than quantitative.
(4) Polarization parameters frequently show low linearity, especially in real data. In many cases this fact indicates interference between modes rather than real low linearity.

As mentioned above, the results from polarization analysis seem more qualitative than quantitative. The polarization filtering method applied shows some success and has potential to be used for filtering of high-energy barely mixed events. The covariance matrix method used for analysis and filtering works on independent traces. Taking into account more traces with the same information could improve the results obtained.

CHAPTER 4

GEOPHONE ORIENTATION VIA POLARIZATION ANALYSIS

4.1. Introduction

In this chapter a practical problem, geophone orientation, is investigated using the three polarization analysis methods described in Chapter 3, applied to seismic events originated at the NSL.

In multicomponent methods, a known orientation of the elements is required to properly recover the horizontally polarised events motion and, in general, the directional characteristics of the wavefield. Currently, geophone orientation is assumed to be that as per field planting instruction and checking. In 2-D multicomponent data acquisition, sources and receivers are in a line, and one of the horizontal components of the Cartesian geophone is usually oriented in the in-line direction while the other one is situated in the cross-line direction. In a 3C-3D survey, sources and receivers can lie in any relative direction to each other (see Figure 4.1), however the horizontal components are deployed in a similar way to a 2-D line, a component in the receiver line direction (*in-line*) and the other one transverse to that (*cross-line*). Later, during processing, the components are rotated in direction connecting the source to the receiver. This method implies careful fieldwork to be reliable.

On the other hand, in principle the polarization of seismic events can give us direct knowledge about the components' orientation. In fact, polarization of first arrivals has been used to obtain geophone orientation in marine data and VSP. Development of a method that uses polarization to obtain geophone orientation in surface land seismic data can contribute to more reliable and accurate data acquisition.

Near-surface events are more appropriate for this investigation, since they have relatively high-energy content and are less affected by other interfering events. The polarization of the first arrivals in the real data analysis of Chapter 3 (Figure 3.12, Window 1) is an example of these characteristics.

DiSiena et al. (1984) developed the histogram algorithm (section 3.3.2) to correct the orientation of geophones in the VSP method. This method works quite well for VSP data and has been used in practice for many years. Bland and Stewart (1996) proposed the use of the polarization data of first arrivals to correct the geophones' orientation in the land surface 3-C seismic method. They found it difficult to correlate polarization with source-geophone direction. A number of potential factors could be at play including: errors in the location of sources and receivers, inaccurate receiver orientation, coupling, incorrect wiring,, complicated near-surface propagation, and closely vertical first arrivals.

This chapter explores the relation between geophone orientation and polarization in land data from a multicomponent 2-D (3C-2D) experimental survey.

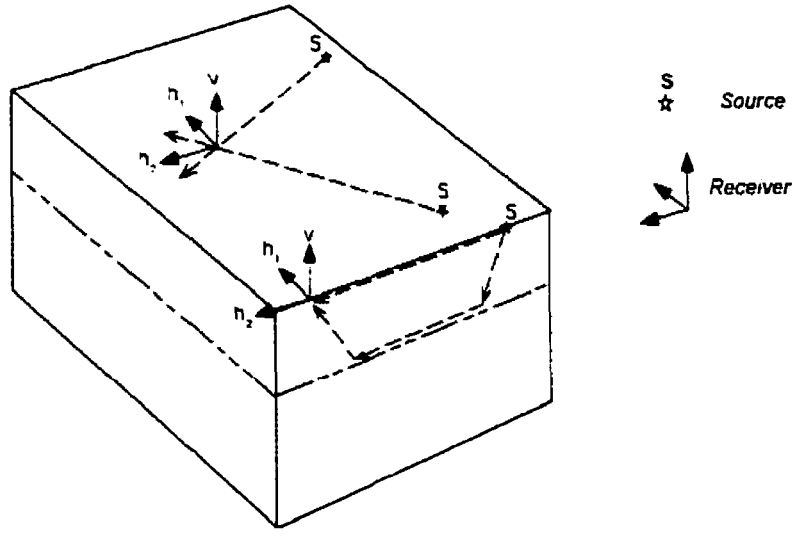

Figure 4.1. Relation between polarization and source-receiver direction in multicomponent 2-D and 3-D surveys. Receivers usually are oriented in the in-line direction. Source-receiver direction is on the line in 2-D and can have any direction in 3-D.

4.2. Method

The relationship between geophone orientation and polarization of the horizontal components is studied on prestack seismic trace gathers, in shot and receiver domains. The polarization analysis methods, explained in Chapter 3 (i.e. hodograms, the histogram and the covariance matrix methods), are used on time windows defined over a selected seismic event with no filtering or amplitude correction applied. Linear polarization can have two opposite values that are considered equivalent and, when necessary, one of them will be preferred for analysis.

A diagram with two parts, hodograms and histogram, is used to present results. Two kinds of hodograms are presented, one with a top view and the other with a lateral view (e.g. Figure 4.4). The lateral view (the vertical and the horizontal in-line components) can provide useful data about the wave mode (column *a* in Figure 4.4) and the top view hodogram (horizontal components, column *b*) has the azimuthal direction information. The linearity calculated with the covariance method is presented jointly with the histogram (the value *fl* in column *c*). Because the scale in a hodogram is determined by its maximum value, the lateral and top view hodograms can have different scales. As they have a horizontal component in common, a scale factor can be defined given by the ratio of this component sizes in the two hodograms.

Analysis of polarization direction in complete gathers, using the covariance matrix method, is also carried out. With this method, it is possible to obtain more meaningful correlations of source-receiver and polarization angles.

4.3. Polarization and geophone orientation in Blackfoot III 3C-2D

In this section, polarization and geophone orientation from data of the Blackfoot III 3C-2D seismic survey is analyzed. General information about that survey is given in section 3.5.2 and more complete information can be found in Hoffe et al. (1998). From the several types of data collected, a shot gather of a high-resolution seismic line, with 1 km length and 2 m distance between geophones, was selected.

To introduce a 3-D effect, a Shot Point 48 m offset from the geophone line was selected. One hundred seventy one receivers symmetrical in relation to the source were used, forming approximately a *split-spread* geometry (with the source in the middle). Figure 4.2 illustrates the receiver locations.

4.3.1. Description

Figure 4.3 illustrates the data recorded and the four events selected with the corresponding analysis windows. Event 1 corresponds to first arrivals, with an apparent velocity of 2300 m/s. Event 2, picked in the radial component, is parallel to the first arrivals. Event 3, selected in the radial component, has an apparent velocity close to 800 m/s. Event 4 has an approximate apparent velocity of 360 m/s.

Two type of analyzes were carried out, the first one using the three methods with five receivers, and the second one using the covariance matrix method and including all the receivers. The five receivers for analysis are shown in Figure 4.2. Table 4.1 shows their source-receiver azimuth according to the acquisition geometry, including the two angles corresponding to opposite azimuths in directions source-receiver and receiver-source.

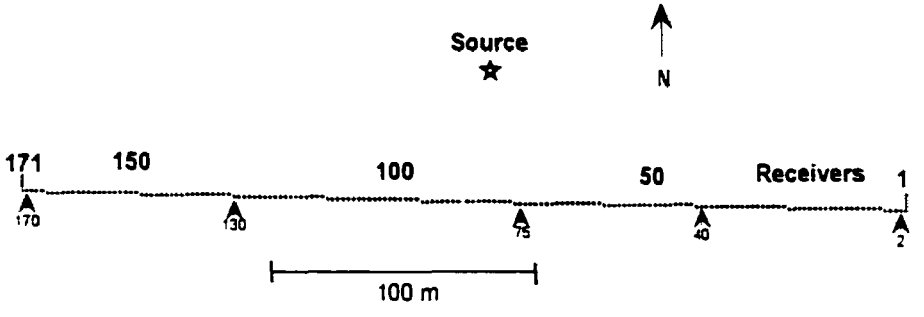

Figure 4.2. Field layout of the Blackfoot III 3C-2D test data. The source is 48 m offset from the line of receivers. Numbers on the line identify receivers and the receivers selected for testing are indicated with arrows.

Table 4.1. Azimuth from the acquisition geometry in Blackfoot III

Receiver Number	*Offset (m)*	*Azimuth*
2	166.7	163.27°
40	96.6	150.21°
75	50.4	107.75°
130	108.3	26.31°
170	183.1	15.2°

The analyzes of the four events are illustrated in Figures 4.4 to 4.7 in a matrix-like form, where each row corresponds to a receiver, column *a* corresponds to the hodogram of the lateral view horizontal *in-line* and vertical components, column *b* to the top view hodogram, and column *c* to the histogram of the horizontal components.

In the hodograms the horizontal components are labeled with *R* (radial or *in-line*), *T* (transverse or *cross-line*), and *V* (vertical). The head arrows in column *c* indicate the theoretical azimuth according to the field geometry. According to the field layout, the radial (*R*) or in-line component corresponds to the component H2 of the geophone (Figure 1.2), and defines the positive direction oriented toward the East (Figure 4.2). The azimuth is calculated counter-clockwise from the direction *R*.

Table 4.2 shows a comparison of the source-receiver azimuth with polarization angle for each one of the four events, using the covariance matrix method. Figures 4.8 to 4.11 illustrate the second type of analysis, all traces of the four events using the covariance matrix method.

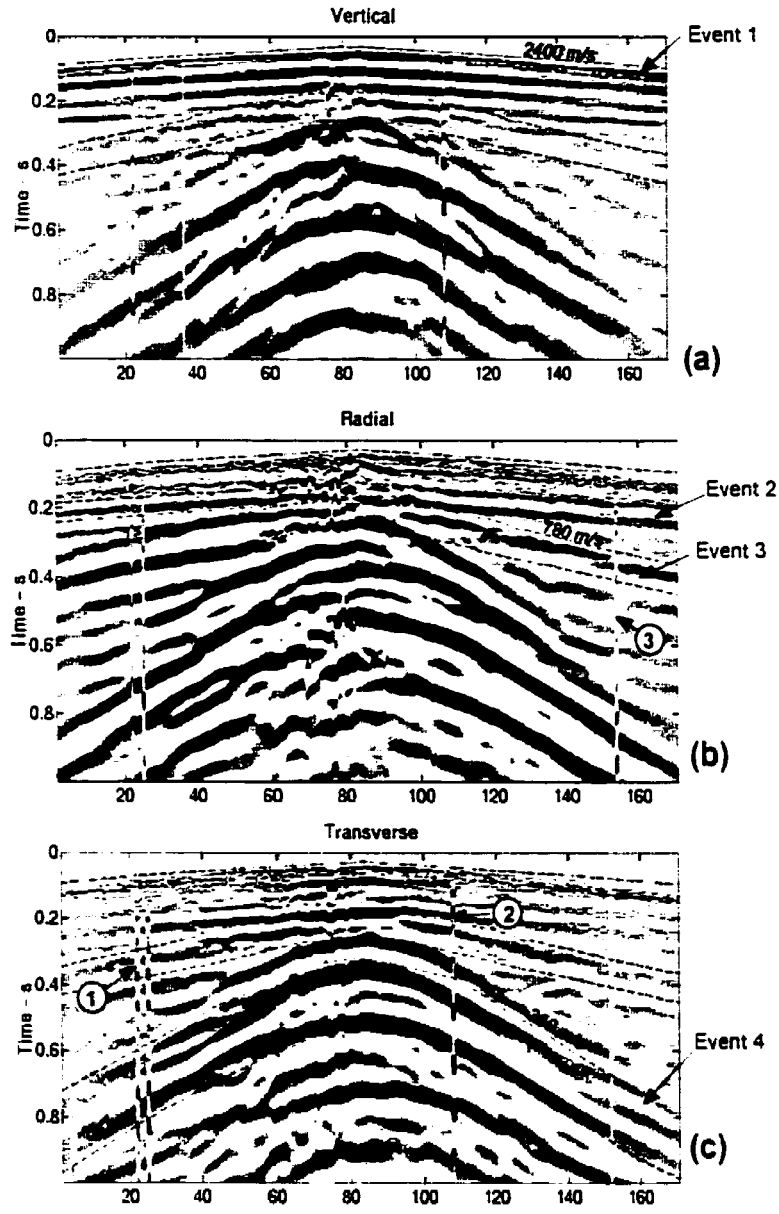

Figure 4.3. Components from Blackfoot III 3C-3D used in the test. (a) Vertical component. (b) Radial (*in-line*) component. (c) Transverse (*Cross-line*) component. The events selected and the corresponding analysis window are indicated. The numbers inside circles identify polarity inversions.

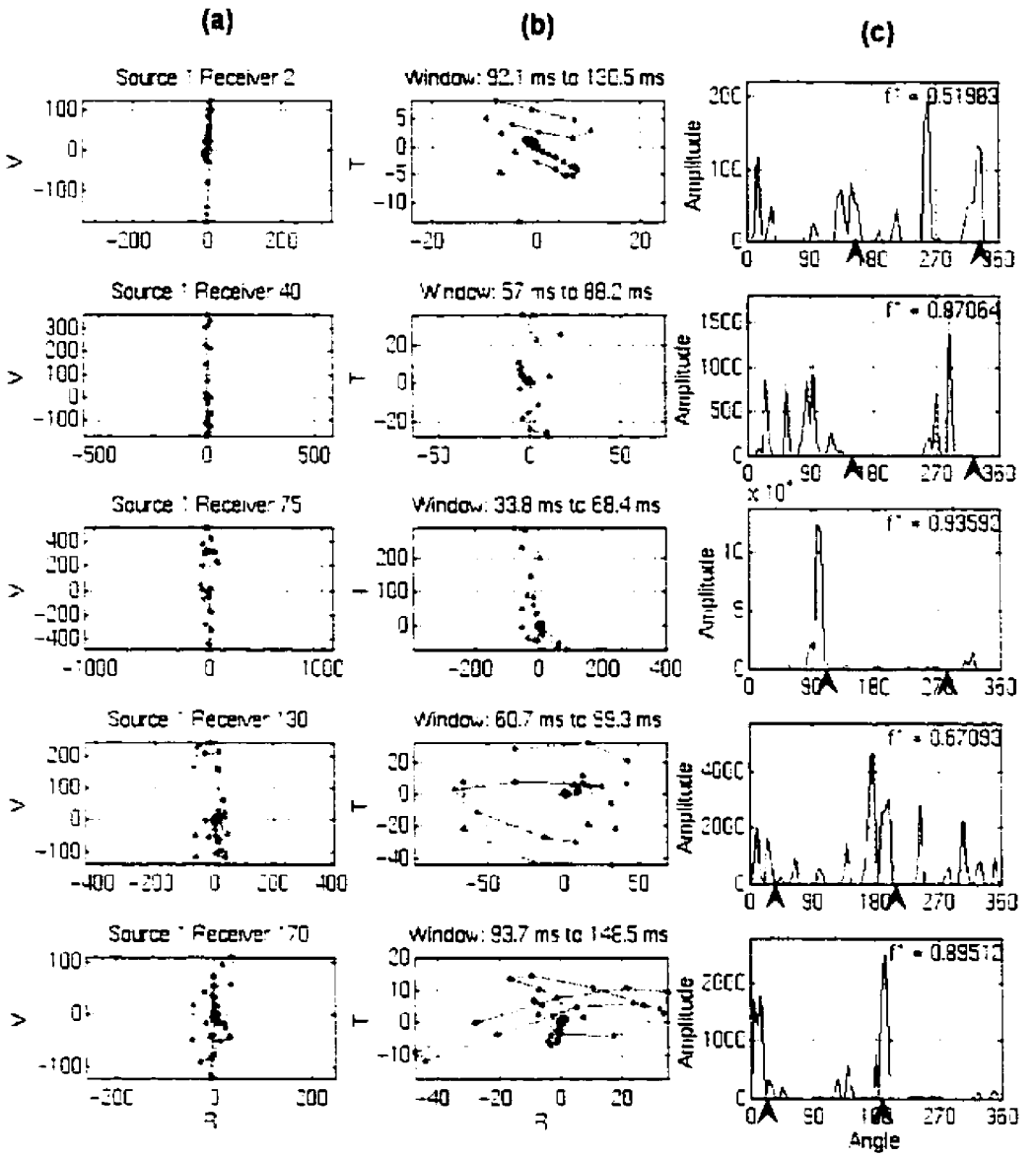

Figure 4.4. Event 1 analysis. (a) Lateral-view hodogram. (b) Top-view hodogram. (c) Histogram and linearity *fl* from the covariance matrix method. The arrows indicate the source-receiver azimuth from field data.

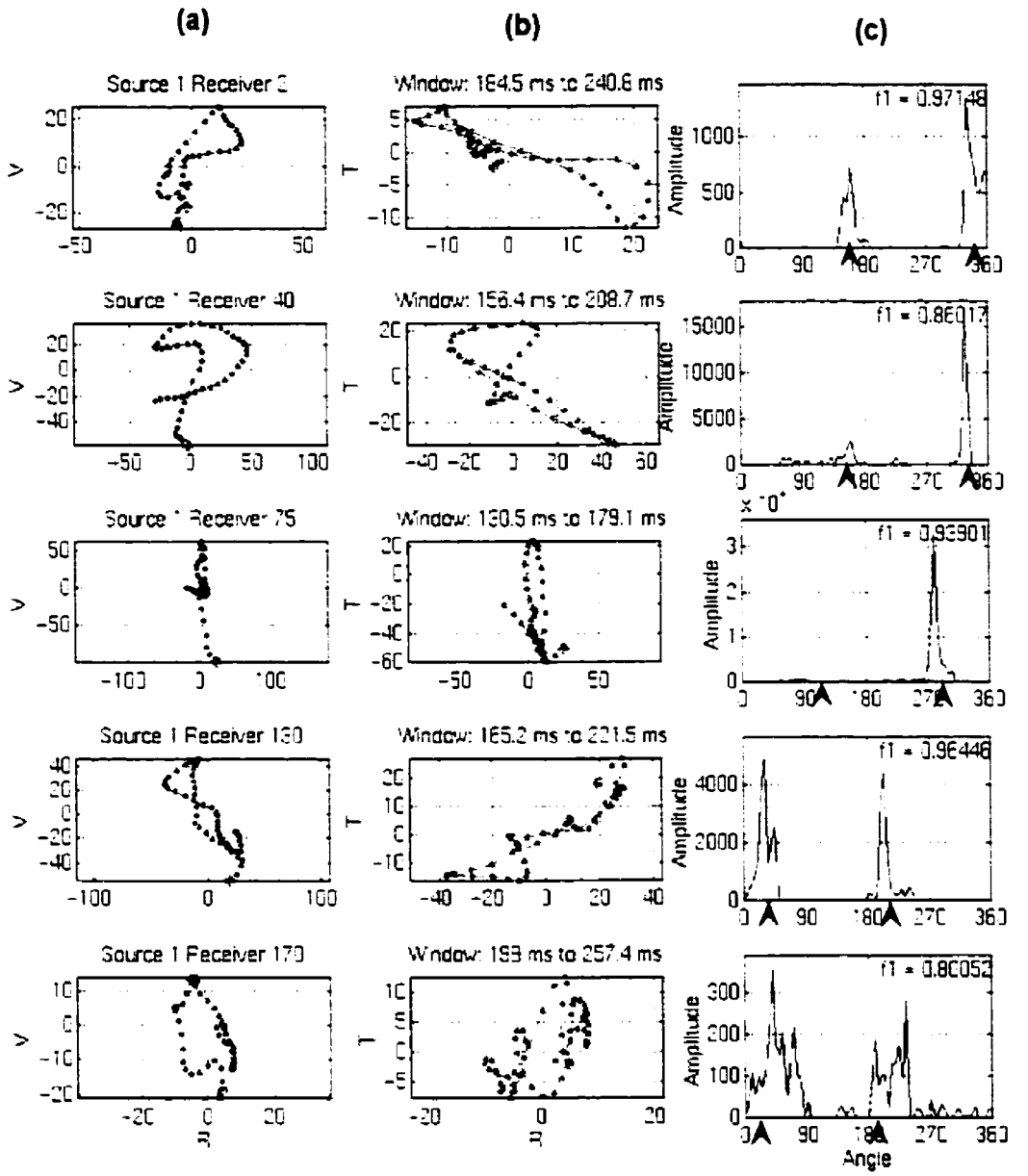

Figure 4.5. Event 2 analysis. (a) Lateral-view hodogram. (b) Top-view hodogram. (c) Histogram and linearity *f1* from the covariance matrix method. The arrows indicate the source-receiver azimuth from field data.

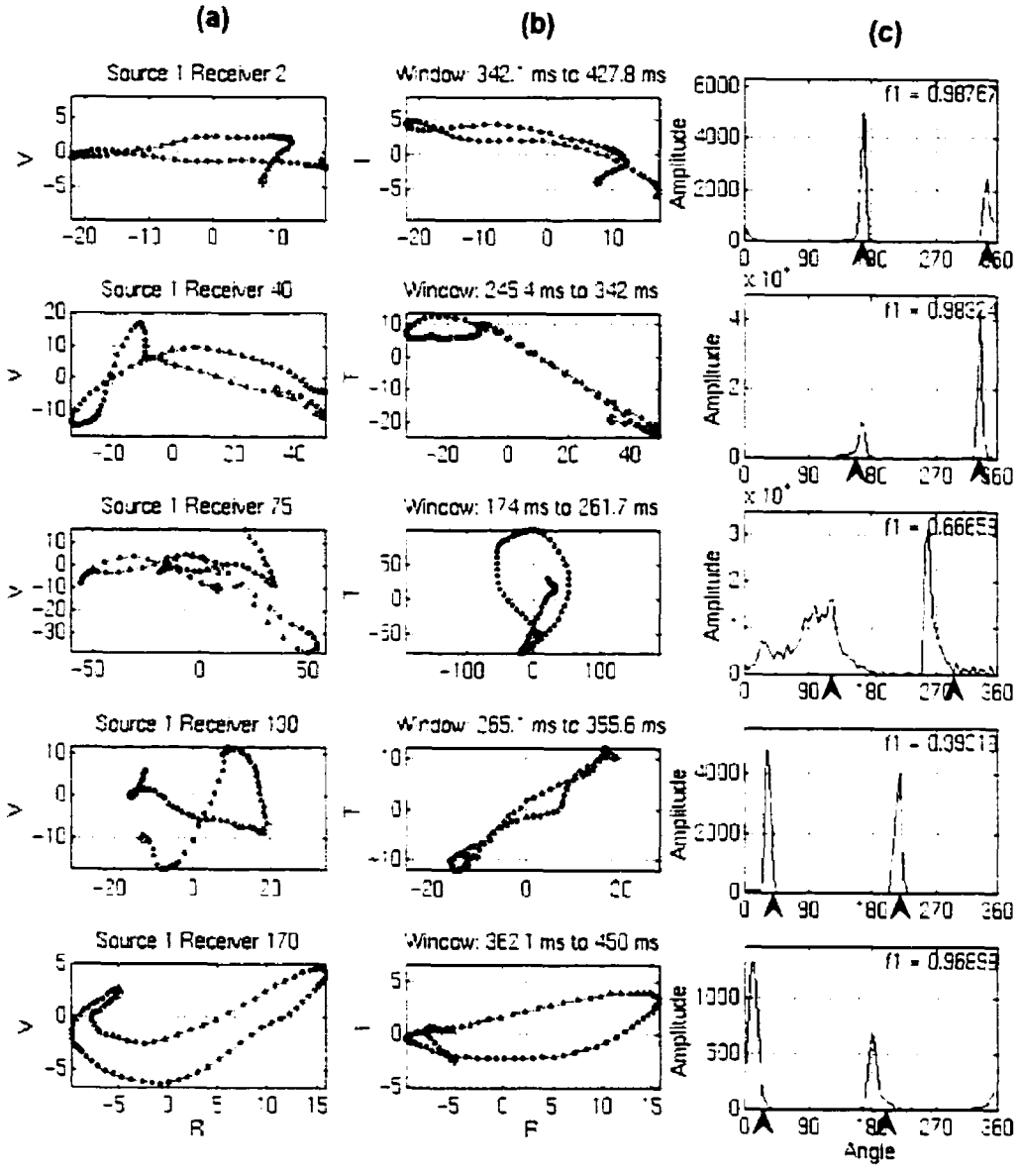

Figure 4.6. Event 3 analysis. (a) Lateral-view hodogram. (b) Top-view hodogram. (c) Histogram and linearity *f1* from the covariance matrix method. The arrows indicate the source-receiver azimuth from field data.

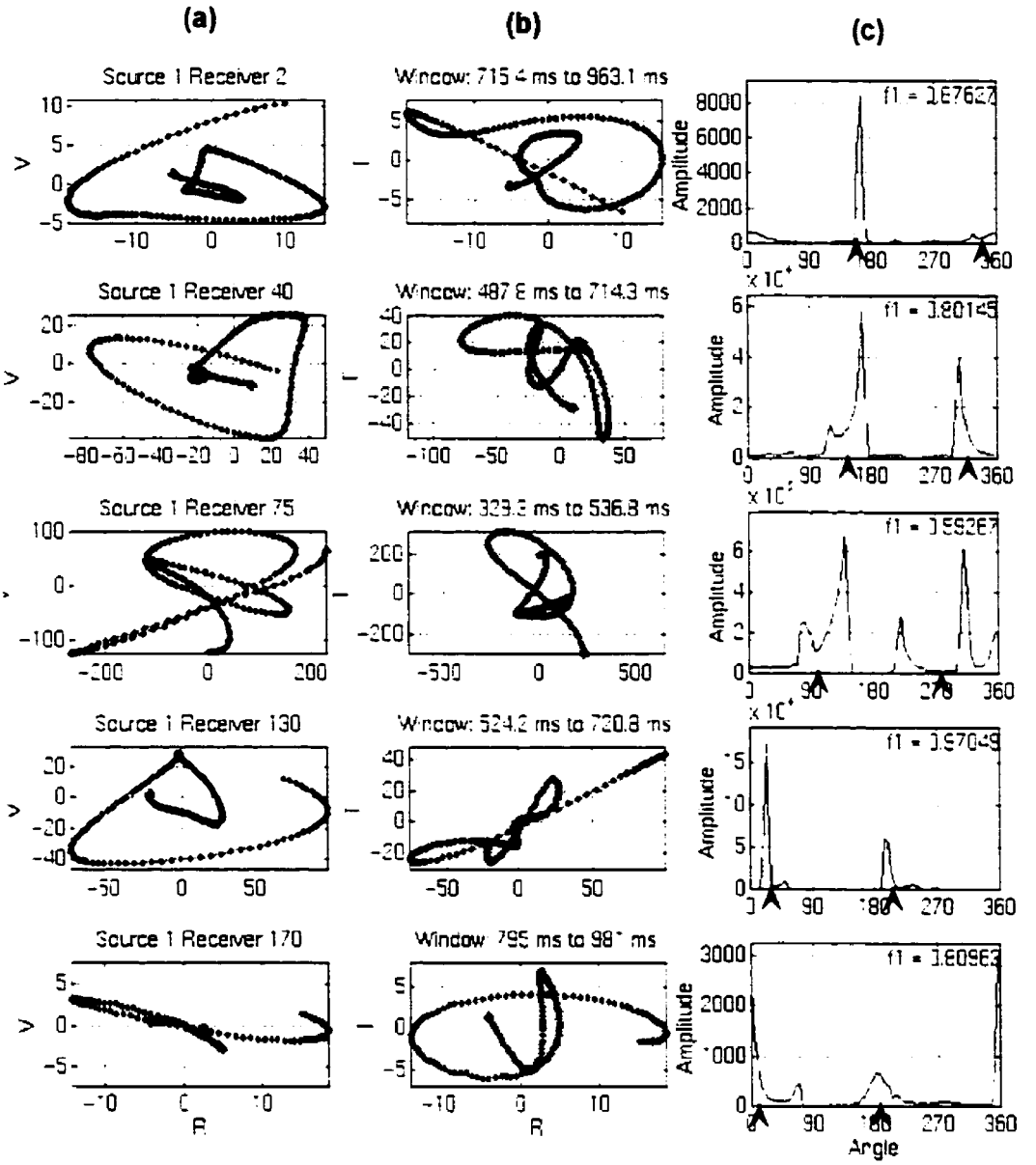

Figure 4.7. Event 4 analysis. (a) Lateral-view hodogram. (b) Top-view hodogram. (c) Histogram and linearity *f* from the covariance matrix method. The arrows indicate the source-receiver azimuth from field data.

Table 4.2: Azimuth S-R versus polarization angle

Receiver Number	*Azimuth*	*Polarization angle*			
	S-R	Event 1	Event 2	Event 3	Event 4
2	163°	152°	159°	168°	168°
40	150°	92°	146°	157°	145°
75	108°	104°	96°	94°	124°
130	26°	2°	29°	34°	25°
170	15°	9°	41°	8°	6°

4.3.2. Results

Event 1 is analyzed in Figure 4.4. The side hodogram (column *a* in Figure 4.4) shows high linearity and more energy than the top view hodogram (column *b* in Figure 4.4). These characteristics, together with the apparent velocity, correspond to a *P* refracted wave. From the top view hodogram the linearity is low and there is little correlation with the source-receiver direction. Also there is a weak correlation with the azimuth of maximum energy of the second event (column *c* in Fig. 4.4).

The second event (Figure 4.5) shows high energy content in the horizontal components, high linearity and good correlation of the polarization angle with the azimuth source-receiver. The arrowheads in column *c* indicate the theoretical azimuth from field data (Table 4.1), which shows near correlation with the direction obtained from the histogram. The second event apparent velocity corresponds to the *P*-wave refraction velocity (first event), however its polarization has a strong horizontal component. It might correspond to converted *S*-wave created by the *P*-wave refraction.

As for the analysis of the third event (Figure 4.6), its more marked feature is a highly linear polarization in the horizontal components, shown in columns *b* and *c* of Figure 4.6. The third event has characteristics of shear wave refraction, because of its horizontal polarization and its apparent velocity. This interpretation agrees with a result of Dufour

and Lawton (1996). Receiver 75 show lower linearity, which can be related with interference of ground-roll or other wave modes, since this receiver is close to the source (see location in Figure 4.2).

Event 4 (Figure 4.7) can correspond to surface waves since it trends to elliptical polarization instead of linear and high energy content. It shows also good correlation between the angle source-receiver and the polarization angle.

Figures 4.8 to 4.11 illustrate the results of the second analysis, using the covariance matrix method along all the traces of each event selected. To carry out this comparison, the source-receiver azimuths, measured clockwise from the North, were translated to the two feasible values in the reference system of the receivers, namely counter clockwise from the radial positive component (R). The azimuthally opposite two values of polarization are considered equivalent, then when one of them is present the other one is calculated.

In all of the events a correlation exists between the calculated source-receiver angle and the horizontal polarization direction. This correlation however is low in the case of event 1, first arrivals (Figure 4.8), and is high in events 2 to 4 (Figures 4.9 to 4.11). Some polarization anomalies, marked with numbers in Figure 4.10 and identifiable in Figures 4.9 and 4.11, can be related to the trace inversions (i. e. polarity reversals) indicated in the shot gather, Figure 4.3.

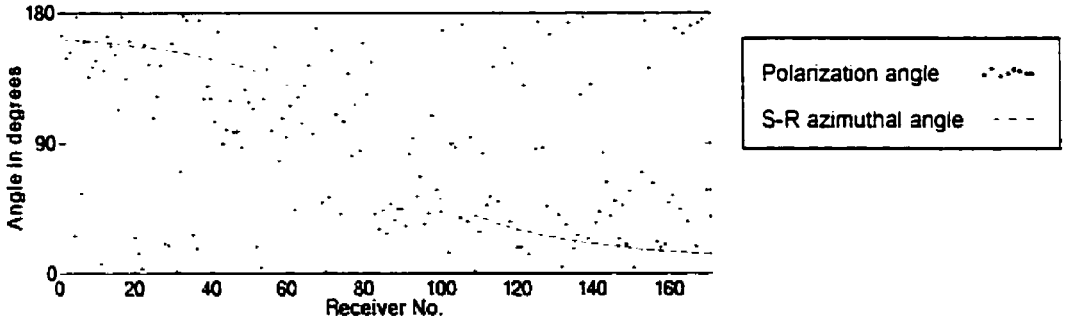

Figure 4.8. Event 1 polarization angles and Source-Receiver angles comparison using the covariance matrix method. Note the low correlation.

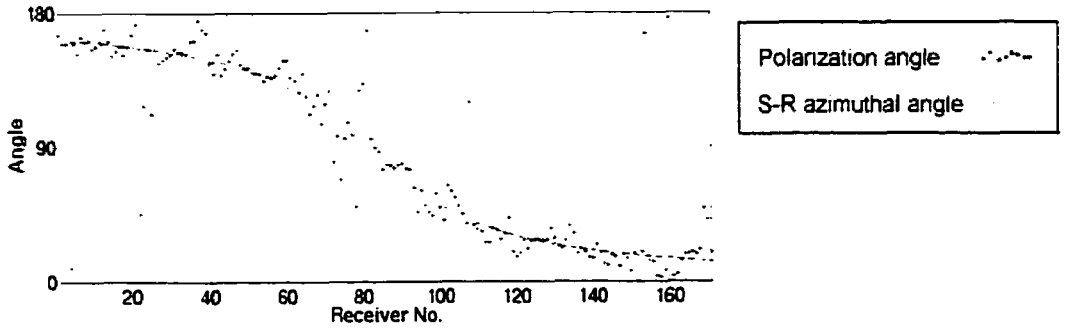

Figure 4.9. Second event polarization angles and Source-Receiver angles comparison using the covariance matrix method.

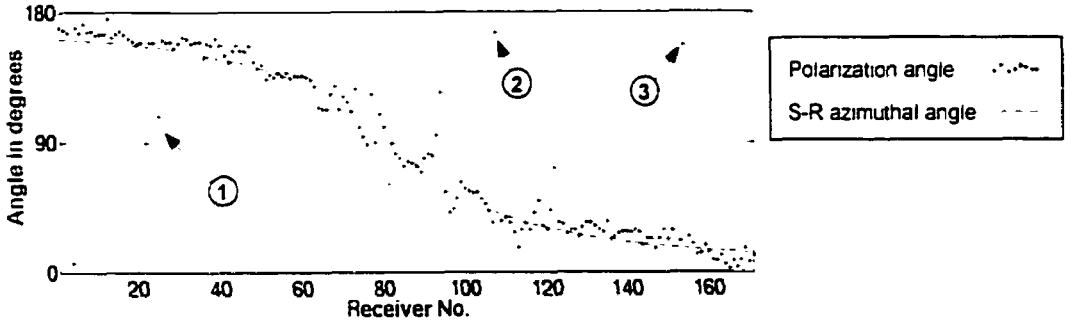

Figure 4.10. Third event polarization angles and Source-Receiver angles comparison using the covariance matrix method. Numbers inside circles show polarization anomalies corresponding to polarization inversions in the data of Figure 4.3.

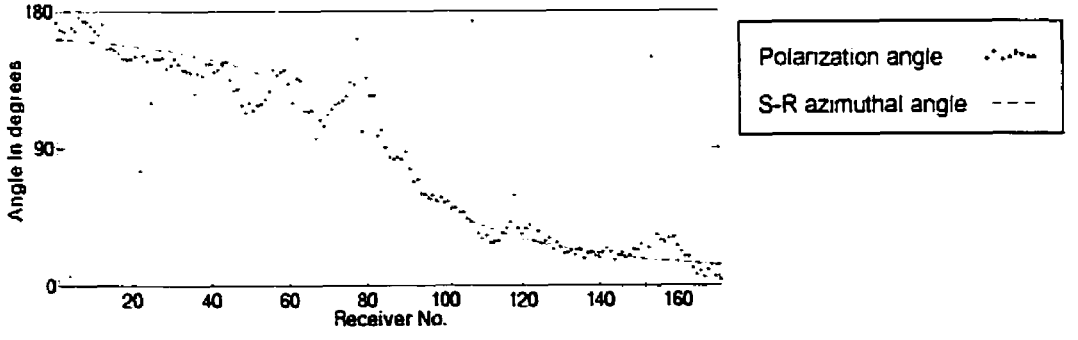

Figure 4.11. Fourth event (Ground roll) polarization angles and Source-Receiver angles comparison using the covariance matrix method.

4.4. Discussion and conclusions

In this chapter, the polarization of events originating at the NSL has been used to study the source-receiver direction in an experimental 3C-3D seismic survey. The three methods of analysis described in chapter 3 were applied to four data windows on high-energy seismic events. A summary of the results follows.

(1) In the first break window, the linearity and the correlation of the polarization angle with the azimuth source-receiver are low. This event shows almost vertical polarization, and the energy of the horizontal components is only a fraction of the energy of the vertical components.

(2) The individual trace analyzes of the other events (identified as Events 2, 3 and 4 in Figure 4.5) show a polarization angle nearly correlated to the azimuth source-receiver. This is confirmed by complete gather analyzes using the covariance matrix method (Figures 4.8, 4.9 and 4.10).

Event 1 is interpreted as *P*-wave refraction. These results agree with those of Bland and Stewart (1996), who noted difficulties in obtaining geophone direction from first arrivals. Events 2, 3 and 4 are interpreted as converted-wave refraction, *S*-wave refraction and Ground Roll, respectively.

The following observations are based on these analyzes.

(1) The results of the three polarization analysis methods agree with each other. This agreement supports the reliability of the analysis; it is independent of the method.

(2) The information obtained from polarization depends on the seismic event selected.

Many factors can affect the polarization measurements. Some factors are related to the source of energy and to the receiver, such as coupling, type of source or receiver, and location. Other factors are related to the wave trajectory and the elastic properties of the terrain, such as lithology, geologic structures. Additional factors are associated with the acquisition method or the environment; these include wiring, polarity of connections, environmental noise and feasible errors in deployment or mislocations (Bland and Stewart, 1996).

The geophone characteristics relate to electronic features of the instrument and to an issue in multicomponent acquisition, known as the *vector fidelity*. According to Tree (1999), "a seismic acquisition system exhibits vector fidelity when it accurately records the magnitude and direction of a seismic wave in 3 dimensions". This means that the response to equivalent inputs should be the same for each component. Currently, this is not guaranteed in surface land acquisition, since the vector fidelity is usually not tested. On the other hand, the geophone response for the 2-D case, as described in section 1.3 and in Appendix C, is really a 3-D effect, as shown by Kähler and Meissner, 1983. It can affect the polarization characteristics of 3C-3D seismic data, and is worthy of investigation.

A method to obtain information about geophone orientation based on horizontally polarized events can likely be developed, using events generated at the NSL. Such a method can take advantage of the different domains and the redundancy of the polarization information to obtain a reliable and robust estimation of the orientation.

CHAPTER 5

A METHOD FOR MODE SEPARATION INCLUDING STATICS

5.1. Introduction

An objective in multicomponent data processing is to obtain two independent seismic sections, one using *P* wave and the other using *S* wave (see 1.2.5). Usually it is assumed that the vertical component records *P* waves and the horizontal component *S* waves and with such an assumption, good seismic information have been obtained. However, as shown by the synthetics in chapter 2, there is *mode leakage* or *mode cross-talk*, since both wave modes can be observed in both vertical and horizontal components. Examples of this phenomenon in real data are also documented in the literature (e. g. Tatham and Goldsbee, 1984; Lu and Margrave, 1999).

Mode leakage is partially explained by the *free-surface effect* described in Chapter 1 section 1.3. From the free-surface condition, it can be shown how the vertical and horizontal components detect both wave modes, depending on the incident wave and on the near surface elastic properties.

A number of methods have been proposed to separate wave modes (e.g. Tatham and Goldsbee 1984; Dankbaar 1985; Devaney and Oristaglio, 1986; Esmersoy, 1990; Donati, 1996). Dankbaar (1985) uses the free-surface response equations to perform the separation in the *f-k* domain. Donati (1996) applies similar principles to land and marine data in the τ-p domain.

Mode-separation methods do not consider *statics*, an effect of the NSL on reflections from deeper interfaces (Section 1.3.5). As introduced in Chapter 1, a static is a relative delay of the seismic energy caused by heterogeneity of the NSL and has to be corrected to reconstruct properly the information from geologic targets. It was also shown that the *S* wave statics are usually much larger and do not correlate with *P* wave statics. Usually statics correction is separated into two parts: source statics and receiver statics. In the

converted *P-S* wave method, source statics corresponds to *P* waves and receiver statics to *S* waves.

The current mode separation methods, as they do not take into account statics, are more properly applied in the receiver domain, because there is little relative shifting among the traces, since they are affected by the same *S*-wave statics. However, land data usually have large separation between sources, often several times greater than the receiver separation, then the receiver gathers are often affected by *aliasing*. On the other hand, although shot gathers are probably not aliased, each trace is affected by a different *S*-wave receiver static. Besides that, *P* and *S* wave modes are affected by different statics, then a mixed wavefield would imply two statics corrections.

A method that takes into account the statics problem while separating modes has been proposed by Cary (1998). This method uses the free-surface response and the statics correction, and thus in principle, can be applied advantageously to land *P-S* converted waves in the shot domain.

In this chapter, the method proposed by Cary (1998) is applied to synthetic and real data. The method showed good results with synthetic data and was robust with respect to errors in the near-surface velocities. From the results on real data, an improvement in the stacked section was observed.

5.2. Theory

The method is based in the free-surface effect theory, examined in section 1.3.3. Taking into account the free-surface effect the geophone response in each direction can be expressed as the free-surface effect coefficient times the amplitude of the corresponding incident seismic event. For example, if a *S*-wave event U_S arrives with angle of incidence ϕ and with near-surface velocities V_P and V_S, the vertical component response D_S^v would be

$$D_S^v = R_S^v(\phi, V_S, V_P) U_S(\phi) \,. \qquad (5.1)$$

where $R_S^v(\phi, V_S, V_P)$ is the coefficient of the vertical component for incident S wave, calculated from the free-surface effect.

Then decomposing the wavefield according to angles of incidence would allow to apply equation 5.1. The τ-p transform is a method that allows the decomposition of the wavefield according to angles of incidence (e. g., Dunne and Beresford, 1995; Stoffa et al., 1981). According to this transform, the amplitude $f(x,t)$ of the seismic wavefield, which is detected in the space location x with arrival time t, is mapped onto the amplitude $F(\tau,p)$ in the domain of intercept time τ and event slope p, according to the relation

$$F(\tau, p) = \int_{-\infty}^{\infty} f(\tau + px, x)dx \ .$$

The slope p is the *ray parameter* or *apparent slowness*, defined as

$$p = \frac{\Delta t}{\Delta x} = \frac{\sin\theta}{V}. \qquad (5.2)$$

where for a specific seismic event, Δt is the time change corresponding to an space change Δx, θ is the angle of incidence and V is the velocity of the wave (see Appendix A and Figure A.1).

If the complete wave-field is represented using the τ-p transform, and the coefficients R are represented as a function of the apparent slowness or ray parameter p, the vertical (D^v) and horizontal (D^h) geophone responses are

$$D^v(\tau, p) = R_S^v(p, V_S, V_P)U_S(\tau, p) + R_P^v(p, V_S, V_P)U_P(\tau, p) \quad (5.3a),$$

$$D^h(\tau, p) = R_S^h(p, V_S, V_P)U_S(\tau, p) + R_P^h(p, V_S, V_P)U_P(\tau, p) \quad (5.3b),$$

which are the basic relations of the mode separation method developed by Dankbaar (1985).

To perform mode separation including statics, a constant NSL thickness is assumed; then the time shifts are caused by horizontal velocity variations in the NSL. From the static corrections, which are assumed previously resolved in the processing flow, the NSL

velocities can be calculated. and then the geophone response can be defined at each receiver location.

For an apparent slowness p_j the plane wave that arrives as $U(\tau, p_j)$ to the near-surface layer. becomes $R(p_j, V_S^i, V_P^i)U(\tau - \Delta\tau_i, p_j)$ at the surface geophone in the location i. where $\Delta\tau_i$ is the static correction related to that location and wave mode. Thus. a seismogram at the location x_i can be defined as an inverse discrete τ-p transform.

$$D(t, x_i) = \sum_{j=1}^{n_p} R(p_j, V_P^{x_i}, V_S^{x_i})U(t - p_j x_i - \Delta\tau_i, p_j) \,. \qquad (5.4).$$

The τ-p transform can be implemented in the frequency domain (Margrave. 1998). since $F(\omega, p) = \int f(\omega, x)\exp(i\omega p x)dx$. where ω is the angular frequency and $i = \sqrt{-1}$.

The corresponding discrete expression is $F_j(\omega, p_j) = \sum_i f(\omega, x_i)\exp(i\omega p_j x_i)$. and the inverse discrete τ-p transform is

$$f_i(\omega, x_i) = \sum_j F(\omega, p_j)\exp(-i\omega p_j x_i) \,. \qquad (5.5).$$

In the case of the Frequency domain implementation. the statics correction $\Delta\tau_i$ is equivalent to a phase rotation. $\exp(-i\omega\Delta\tau_i)$. Then. from (5.4) and (5.5). the geophone response to an incident wave U at a location x_i is

$$D(\omega, x_i) = \sum_{j=1}^{M} R(p_j, V_P^{x_i}, V_S^{x_i})U(\omega, p_j)\exp(-i\omega(p_j x_i - \Delta\tau_i)) \,. \qquad (5.6).$$

Therefore. the frequency component ω of the *P*-*S* wavefield present on the vertical component (with N receivers and M slowness) is:

$$\begin{bmatrix} D_S^1(\omega, x_1) \\ D_S^2(\omega, x_2) \\ D_S^3(\omega, x_3) \\ \vdots \\ D_S^N(\omega, x_N) \end{bmatrix} = \begin{pmatrix} R_S^1(p_1, V_1) e^{(-i\omega(p_1 x_1 + \Delta\tau_S^{x_1}))} & R_S^1(p_2, V_1) e^{(-i\omega(p_2 x_1 + \Delta\tau_S^{x_1}))} & \cdots \\ R_S^2(p_1, V_2) e^{(-i\omega(p_1 x_2 + \Delta\tau_S^{x_2}))} & R_S^2(p_2, V_2) e^{(-i\omega(p_2 x_2 + \Delta\tau_S^{x_2}))} & \cdots \\ & & \\ \vdots & \vdots & \\ R_S^N(p_1, V_N) e^{(-i\omega(p_1 x_N + \Delta\tau_S^{x_N}))} & & \cdots \end{pmatrix} \begin{pmatrix} U_S(\omega, p_1) \\ U_S(\omega, p_2) \\ U_S(\omega, p_3) \\ \vdots \\ U_S(\omega, p_M) \end{pmatrix}$$

(5.7)

which can be represented in abbreviated form as

$$\underline{D}_S^v(\omega,\underline{x}) = \underline{\underline{B}}_S^v(\omega,\underline{p},\Delta\tau_S^{\underline{x}},V_P^{\underline{x}},V_S^{\underline{x}})\underline{U}_S(\omega,\underline{p}) \ .$$

or

$$\underline{D}_S^v = \underline{\underline{B}}_S^v \underline{U}_S \ .$$

where a single underline means a vector and a double underline means a matrix.

Similar equations can be obtained for the horizontal component and for the incident *P* wavefield. Therefore the wavefield as recorded by each component is

$$\underline{D^v} = \underline{D_S^v} + \underline{D_P^v} = \underline{\underline{B}_S^v}\underline{U_S} + \underline{\underline{B}_P^v}\underline{U_P} \ . \qquad (5.8.a)$$

and

$$\underline{D^h} = \underline{D_S^h} + \underline{D_P^h} = \underline{\underline{B}_S^h}\underline{U_S} + \underline{\underline{B}_P^h}\underline{U_P} \ . \qquad (5.8.b)$$

which can be represented in matrix form as

$$\begin{pmatrix} \underline{D^v} \\ \underline{D^h} \end{pmatrix} = \begin{pmatrix} \underline{\underline{B}_S^v} & \underline{\underline{B}_P^v} \\ \underline{\underline{B}_S^h} & \underline{\underline{B}_P^h} \end{pmatrix} \begin{pmatrix} \underline{U_S} \\ \underline{U_P} \end{pmatrix} .$$

or, more abbreviated,

$$\underline{D} = \underline{\underline{B}}\,\underline{U} \qquad (5.9).$$

This equation can be solved for $\underline{U}$ using the least-squares inversion formalism

$$\underline{U} = \left(\underline{\underline{B}}^H \underline{\underline{B}}\right)^{-1} \underline{\underline{B}}^H \underline{D} \qquad (5.10),$$

where the super-index ***H*** represents a Hermitian matrix, and the super-index -1 represents matrix inversion (Lines and Treitel, 1984).

The method is illustrated in the flow chart of Figure 5.1. The least-square inversion (equation 5.10) is the basic procedure and the most demanding in terms of computer time. The implementation presented in this thesis was coded in Matlab™.

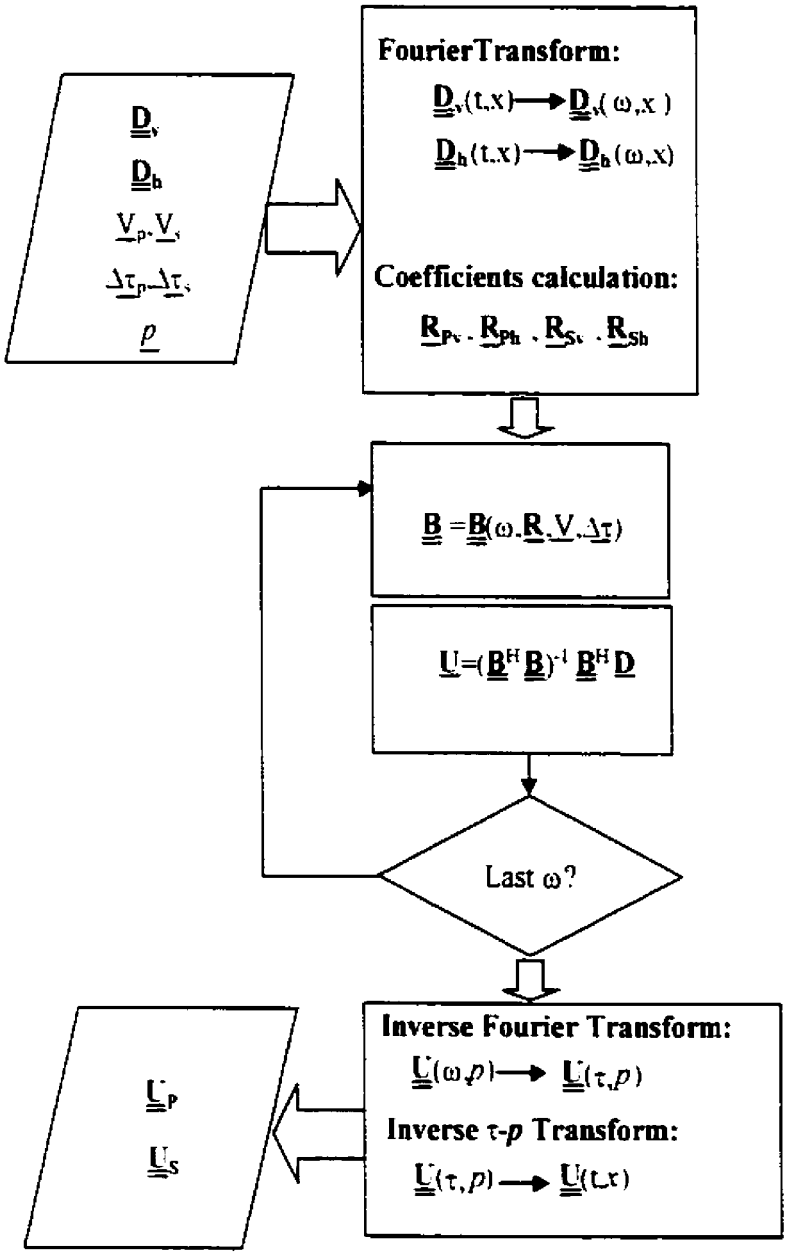

Figure 5.1. Flow chart of algorithm for mode separation in the presence of statics. The input are the wavefields recorded in the vertical and horizontal components, $\underline{\underline{D}}_v$ and $\underline{\underline{D}}_h$, the P and S waves near-surface velocities, V_P and V_S, the source and receiver statics $\Delta\tau_P$ and $\Delta\tau_S$, and the slowness, p. The output are the separated wavefields $\underline{\underline{U}}_P$ and $\underline{\underline{U}}_S$.

5.3. Application to Synthetic data

A geological model from Chapter 2, Model 1, is used to test the method. Figure 5.2 shows the vertical components resulting from the application of the finite-difference method. From the analysis in Sections 3.5.1 and 2.4.1, the events in Figure 5.2 are

(1) Direct wave

(2) Surface waves

(3) *P*-wave reflection

(4) Converted wave reflections (*P* to *S* and *S* to *P*) and

(5) *S*-wave reflection.

Events (3), (4) and (5) are the body waves, which are the target of the mode separation algorithm.

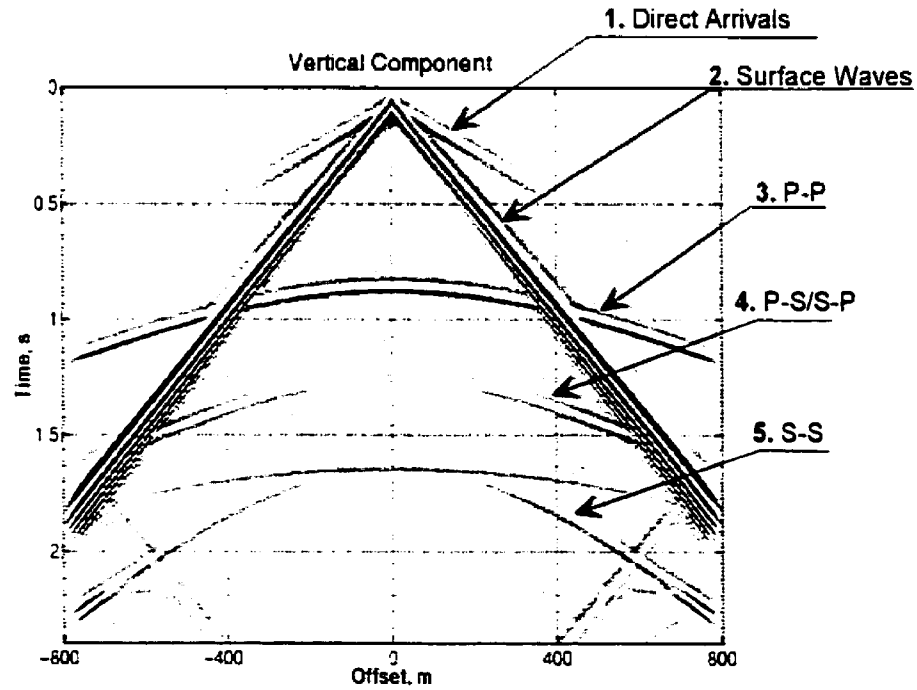

Figure 5.2. Seismic events of the synthetic data used to test the method. This is the FDM resulting vertical component from Model 1 in Chapter 2.

Since events dipping in only one direction are sufficient for test purposes, and the method assumes body waves, only the right-hand half of the spread was used, and interfering

effects of the near surface, such as direct waves and ground roll, were removed. To remove the former synthetic data were created using the Osiris[TD] modelling software, a computationally efficient method that allows that option.

As a first example, a simple statics model was assumed in which two arrival-time delays divide the wavefield in three segments. The data affected by the statics are illustrated in Figure 5.3, where the arrows indicate the time delays. The near-surface velocities were calculated from those delays, assuming a constant thickness of 20 m.

The results of the application of the mode separation method are shown in Figure 5.4. In the *P* wave field, Figure 5.4a, the events are the *P*-wave reflection and the *S* to *P* converted wave. In the *S* wave field the events are the *P* to *S* converted wave and the pure *S* wave. These results agree with the analysis illustrated in Figure 5.2.

Given that values of the near-surface velocities are not readily available in multicomponent data, a second example was used to test the effect of errors in these velocities. Random statics were applied to the same data referred to above, as illustrated in Figure 5.5a. The wave-modes were separated, the statics applied to each one independently and then they were combined again. The velocities were calculated assuming a near-surface layer of 20 m (Figure 5.5b). Input data are illustrated in Figure 5.5c and 5.5d. To carry out the mode separation testing error in velocities, a rough estimate of the velocities, namely the average value, was assumed. Then the *P*-wave velocity assumed is 850 m/s and the *S*-wave velocity 240 m/s. Results after the application of the method are shown in Figure 5.6. Although some mode leakage remains, it is shown that the algorithm behaves reasonably well to velocities error, comparing Figure 5.6 with Figure 5.4.

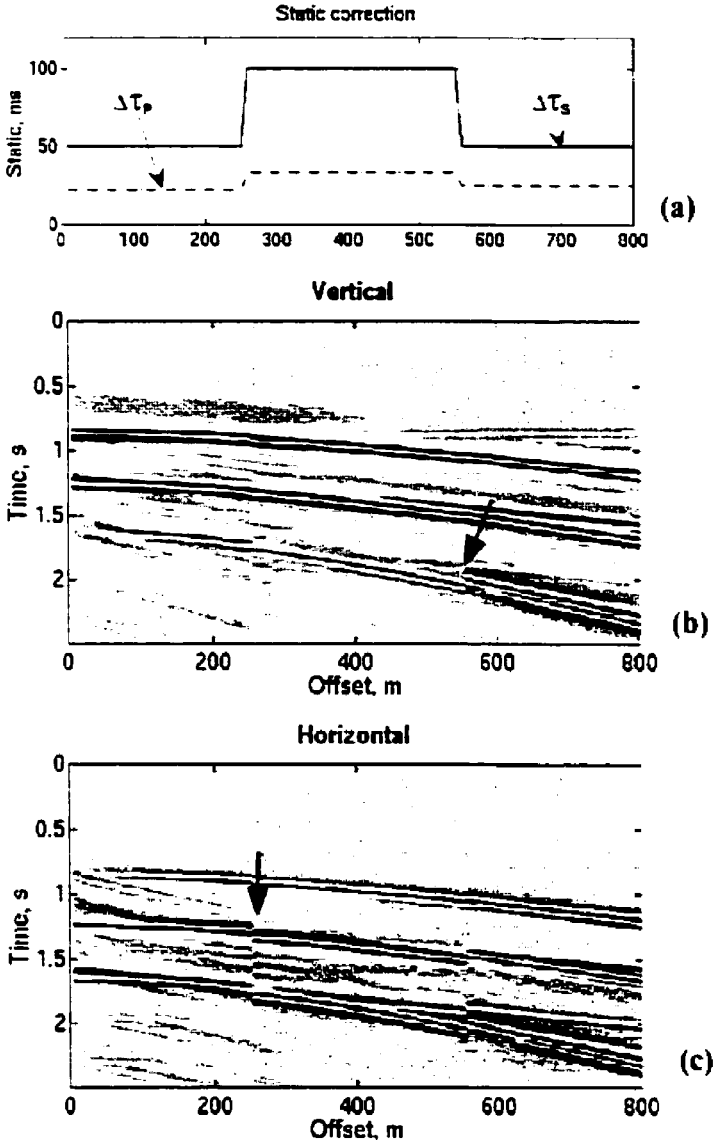

Figure 5.3. First test synthetic data: statics is assumed as a simple trace shifting. (a) The statics corrections applied. $\Delta\tau_P$ for *P* wave and $\Delta\tau_S$ for *S* wave. (b) vertical component. (c) horizontal component. Static shifts are indicated by arrows in (b) and (c).

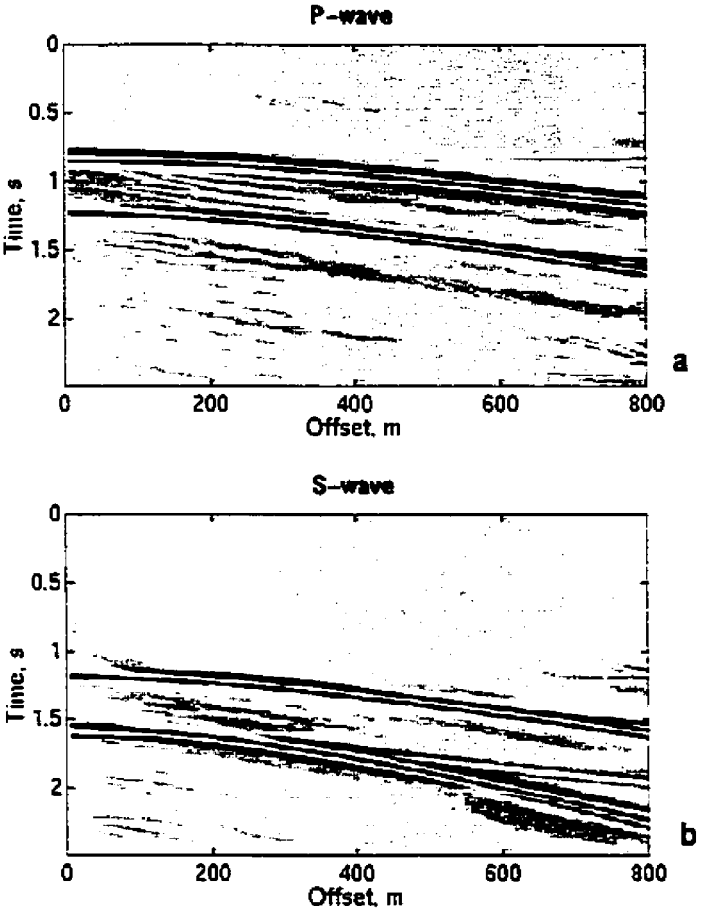

Figure 5.4. Results of the first test with synthetic data. The separated events agree with the interpretation of Figure 5.2.

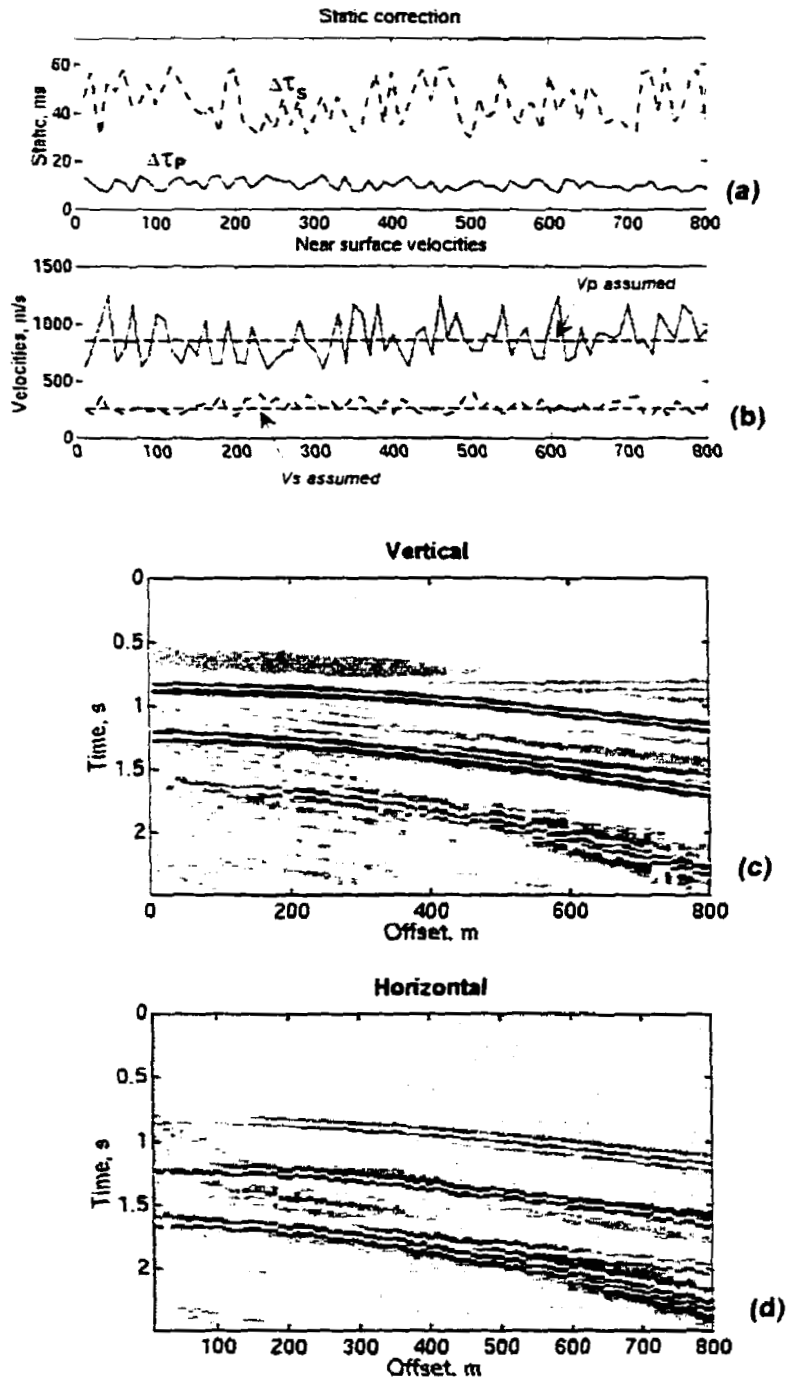

Figure 5.5. Synthetic data used in the second test: statics are random. (a) Statics of P and S wave. (b) velocities calculated from statics and mean value assumed to apply the algorithm. (c) vertical component. (d) horizontal component.

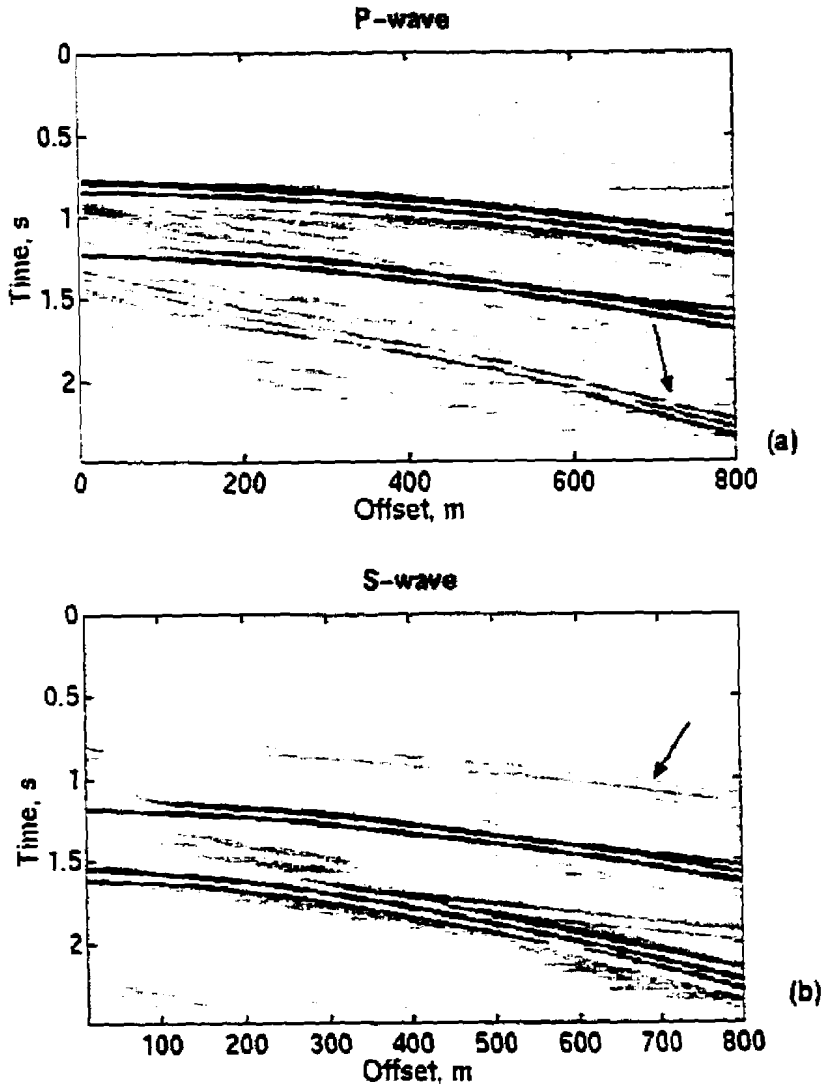

Figure 5.6. Results of the second test with synthetic-data. (a) *P* wave. (b) *S* wave. The arrows show remaining effects of mode leakage.

5.4. Application to Real data

5.4.1. The real data set

Real data from the seismic survey Blackfoot III (used in Chapters 3 and 4), was used to test the method. Some aspects of this survey are described in Section 3.6.2. A more complete description can be found in Hoffe et al. (1998).

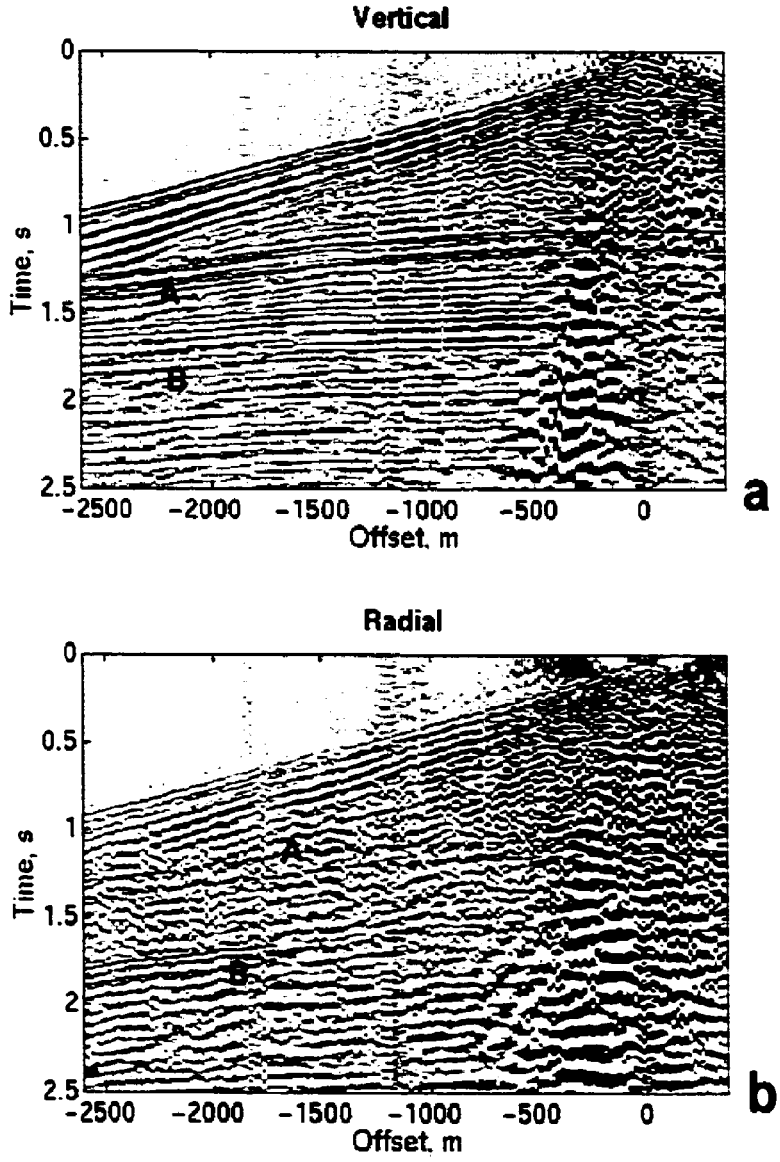

Figure 5.7. Real data used to test the method: a shot from Blackfoot III. (a) Vertical component. (b) radial component. The windows labeled *A* and *B* are used for analysis of the angle of incidence.

The test was performed on the surface seismic line acquired there. This line has 3 km length, with shots and receivers separated by 20 m to one another. The nominal charge

depth was 18 m. the total record length was 2.5 s with 1 ms sampling interval. Shots separated by 100 m to each other were selected to obtain a more typical land multicomponent survey line. since the distance between sources is five times larger than the distance between receivers. The data was resampled to 4 ms. which is appropriate to the frequency content and reduces the computational cost. Raw data for the vertical and radial components are illustrated in Fig. 5.7.

To calculate the NSL velocities statics information was used and a thickness of 20 m was assumed. The resulting velocities are shown in Fig. 5.8. These velocities were compared with the results from two other sources of information. namely the work of Cieslewicz (1999) and the drilling report. Cieslewicz (1999) calculated the near-surface velocities using buried geophones in the central kilometer of the same seismic line. with depths 6. 12 and 18 m. The resulting velocities for the 18 m geophones are shown with asterisks (V_P) and crosses (V_S) in Figure 5.8. with good correlation. The records of the acquisition crew report sandstone in the place indicated with an arrow in Figure 5.8. which could explain the high near-surface velocities found in that place. particularly for *S* waves. and the high V_P/V_S ratio. more appropriate for consolidated rocks than for weathering layers.

To estimate how much cross-talk may be expected. an analysis based on the free-surface effect is carried out. The two data windows in Figure 5.7 were selected to make that analysis. the window '*A*' corresponds to a *P* wave and the window '*B*' to an *S* wave. As shown in the free-surface effect description (Section 1.3.3). the amount of cross-talk energy depends on the angle of incidence to the surface and on the near-surface elastic parameters (or V_P/V_S ratio). From the velocities in Figure 5.8. the V_P/V_S ratios of 3.75 and 2 of Figure 1.4. correspond to typical values in the study area. The incidence angles can be calculated using the plane wave approximation (equation 5.2). The resulting angles for the two windows are shown in Figure 5.9. For the farther offsets the incidence angle appears to be 4° for *P* wave and 9° for *S* wave. Assuming these values as the maximum incidence angle that may be expected. the maximum amplitude in the horizontal component due to a *P* wave could be 10% of the *P*-wave amplitude on the vertical component (Figure 1.4). Similarly for an incident *S* wave in relation to the vertical

component. a cross-talk of 10% or less might be expected. Therefore. in the maximum case (farther offsets). less than 10% mode leakage is to be expected.

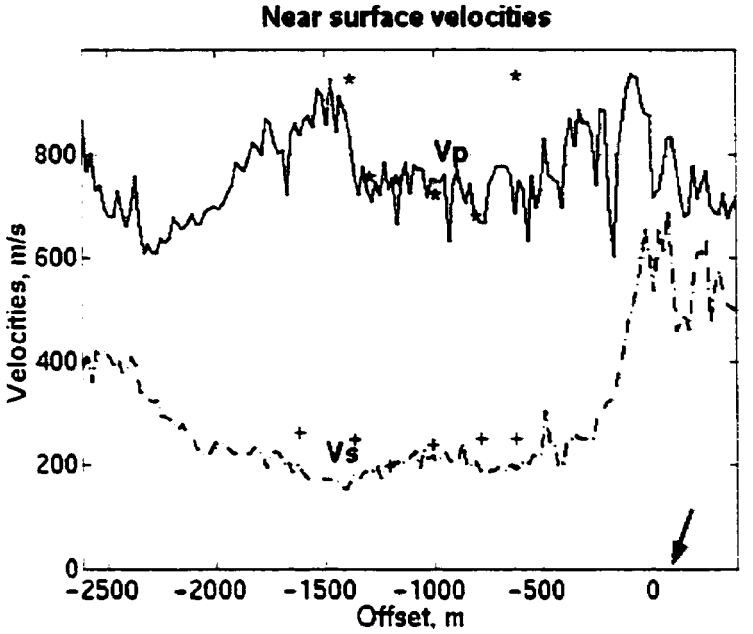

Figure 5.8. Estimated near-surface velocities V_P and V_S in the Blackfoot III survey. These velocities were calculated from the statics correction assuming a constant layer thickness of 20 m. To compare. velocities from another source Cieslewitz (1999). are indicated: V_S by crosses (+) and V_P by asterisks (*). An arrow indicates the location of a sandstone outcrop on the terrain.

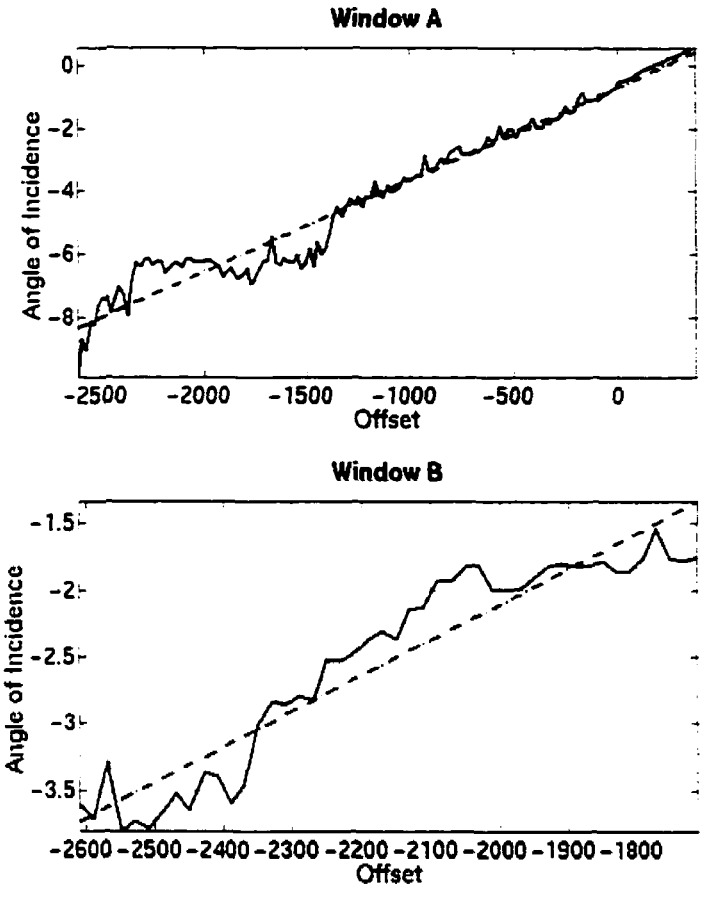

Figure 5.9: Incidence angle of two events from Figure 5.7 as a function of offset. The angle of incidence θ was calculated from the plane wave approximation applied to the windows of Figure 5.7. From the plane wave approximation $\sin\theta$ is $V\Delta t/\Delta x$. The event in window *A* is assumed a *P* wave and the event in window ***B*** as a *S* wave. (a) Angle from P-wave window. (b) angle from S-wave window. The dashed line is a linear approximation.

5.4.2. Mode separation applied to prestack data

The p values in the τ-p transform have a strong effect on the computational efficiency of the algorithm and on the potential to generate numerical artefacts. The apparent slowness p, therefore has to be selected using two criteria: sampling interval appropriate to control

the aliasing effect (Turner, 1990) and a range of values that includes the apparent slowness of the events of interest.

According to Turner (1990), aliasing in the p-domain can be avoided choosing the sampling interval Δp to be

$$\Delta p < \frac{1}{x_r f_{max}} \quad . \qquad (5.11)$$

where x_r is the maximum offset, and f_{max} is the maximum frequency.

From the spectral analysis shown in Figure 5.10, 50 Hz can be considered a reasonable maximum frequency with information for the S event.

Substituing x_r = 3000 m

and f_{max} = 50 Hz in (5.11)

the sampling interval would be 0.666 ms/100 m

A data window in the radial component was analyzed for its frequency content and its apparent slowness (Figure 5.10). The apparent slowness of the events of interest shows values between 33 and 45 ms/100 m. The maximum p value chosen was 50 ms/100 m.

A value of Δp = 0.5 ms/100 m = 5×10^{-6} s/m was selected.

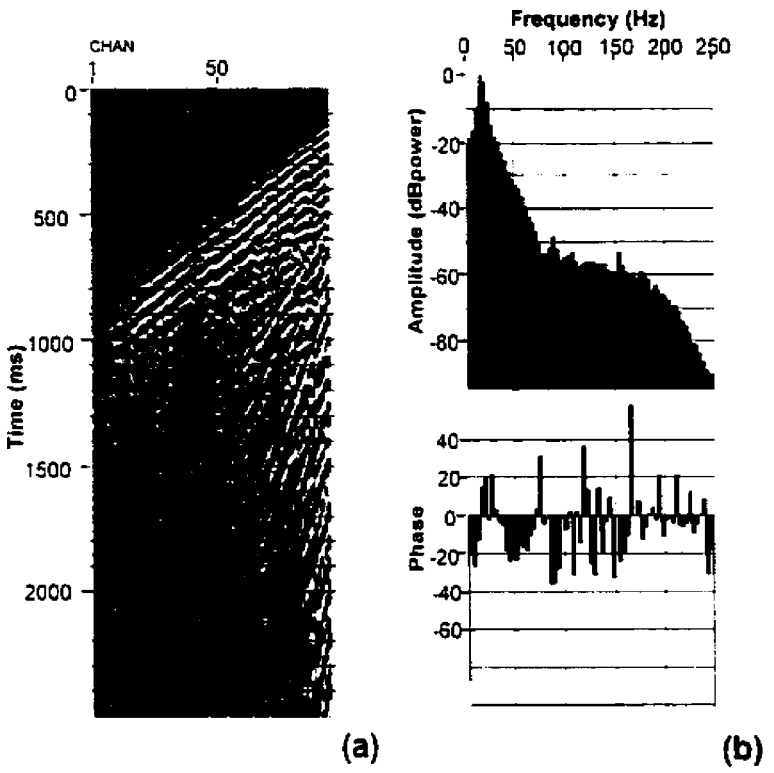

Figure 5.10. Spectral analysis for a window on an event in the Radial component. (a) Seismic data radial component and the analysis window: (b) spectral analysis. Note that most of the energy is under 35 Hz.

The key step of the method is to use the free-surface response for mode separation. Since the algorithm corrects statics and the τ-p transform has filtering effects, a way to test only the mode separation is to compare the results with the application of the method excluding the free-surface effect. To that end, constant coefficients $R_P^v = R_S^h = 1$, and $R_P^h = R_S^v = 0$, were assumed. This assumption is equivalent to consider that the vertical component has only P waves and the horizontal component only S waves, which is the usual assumption in converted wave processing. In other words, equations (5.8) transform to $\underline{D}^v = \underline{\underline{B}}_P^v \underline{U}_P$ and $\underline{D}^h = \underline{\underline{B}}_S^h \underline{U}_S$, where the matrices $\underline{\underline{B}}_P^v$ and $\underline{\underline{B}}_S^h$ do not include the free-surface effect.

The results of the application of the method including the free-surface effect to the shot gather on Figure 5.8 are shown in Figure 5.11. The results obtained after application without the free-surface effect and mode separation are shown in Figure 5.12. Differences between Figures 5.11 and 5.12 are hardly noticed. As stacking is an enhancement procedure for seismic data, is also a way to evaluate the method performance and will be used ahead.

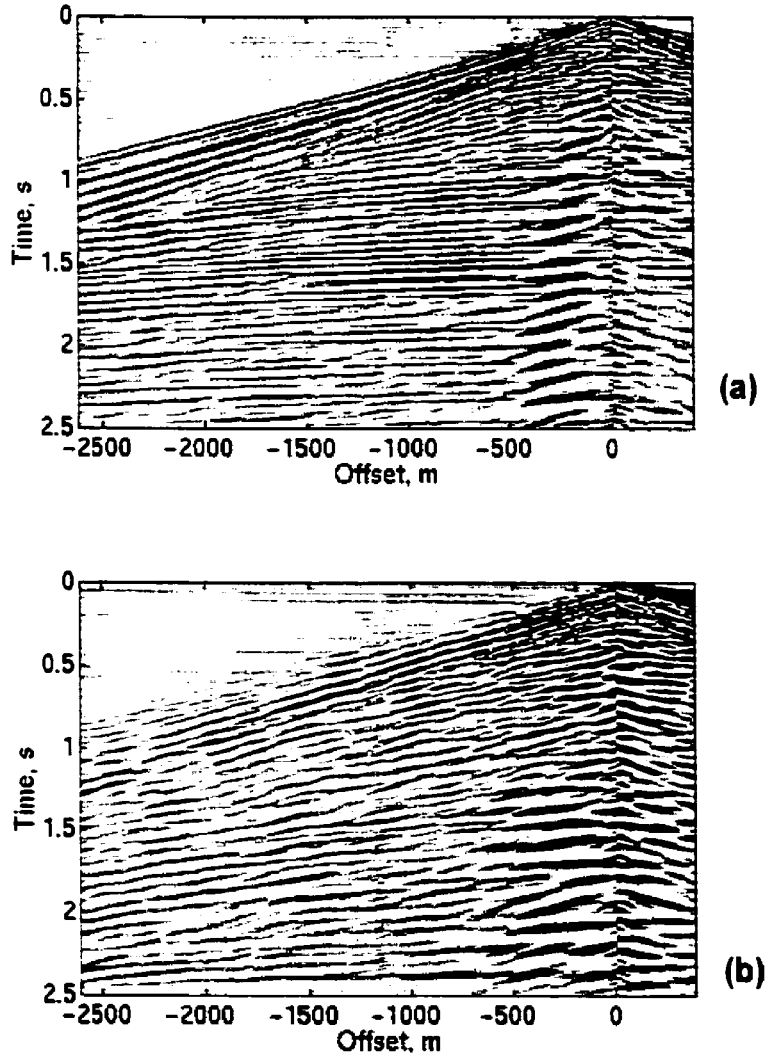

Figure 5.11. Shot after application of mode separation with statics. (a) P-wave, (b) S-wave.

The τ-p transform has a filtering effect, as can be observed comparing Figures 5.7 and 5.12, since the inverse τ-p transform reconstructs events only in the slowness range selected. Also noise and numerical artefacts can be observed in Figures 5.11 and 5.12.

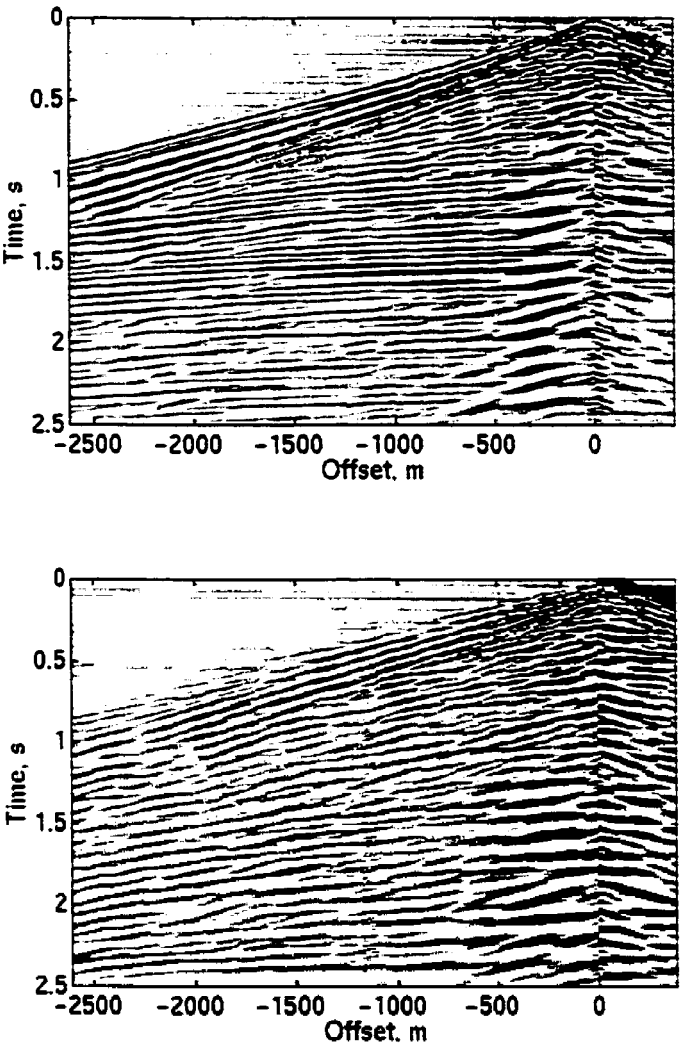

Figure 5.12. Shot after application of the algorithm without mode separation. (a) P-wave, (b) S-wave.

5.4.3. Application of the method to poststack data

As long as the stacking process enhances the information content of seismic data, poststack data was considered to be useful in evaluating the performance of the algorithm. The separation method was applied two times to the 29 shots selected, one time without the free-surface coefficients and the other time with them, as explained in section 5.4.2. Then two data sets were obtained. After that the same processing flow, summarised in Figure 5.13 for *PS* waves, was applied to both data sets. This processing flow is a simplified version of the flow used at CREWES for research purposes (Lu and Margrave, 1999). The software ProMAX™ was used for processing.

Processing Sequence for S-wave:

1. Input Filtered data SEG-Y.
2. Receiver statics substraction.
3. Surface consistent Deconvolution.
4. Asymptotic binning.
5. Rotation of rear component.
6. Application of elevation statics.
7. Application of Source and Receiver Refraction Statics.
8. Application of Hand statics and
9. Application of Residual statics.
10. NMO correction.
11. Time Variant Scaling.
12. Trace Muting.
13. Stack
14. Poststack enhancement
15. Poststack filtering.

Figure 5.13. Processing sequence for *PS* wave.

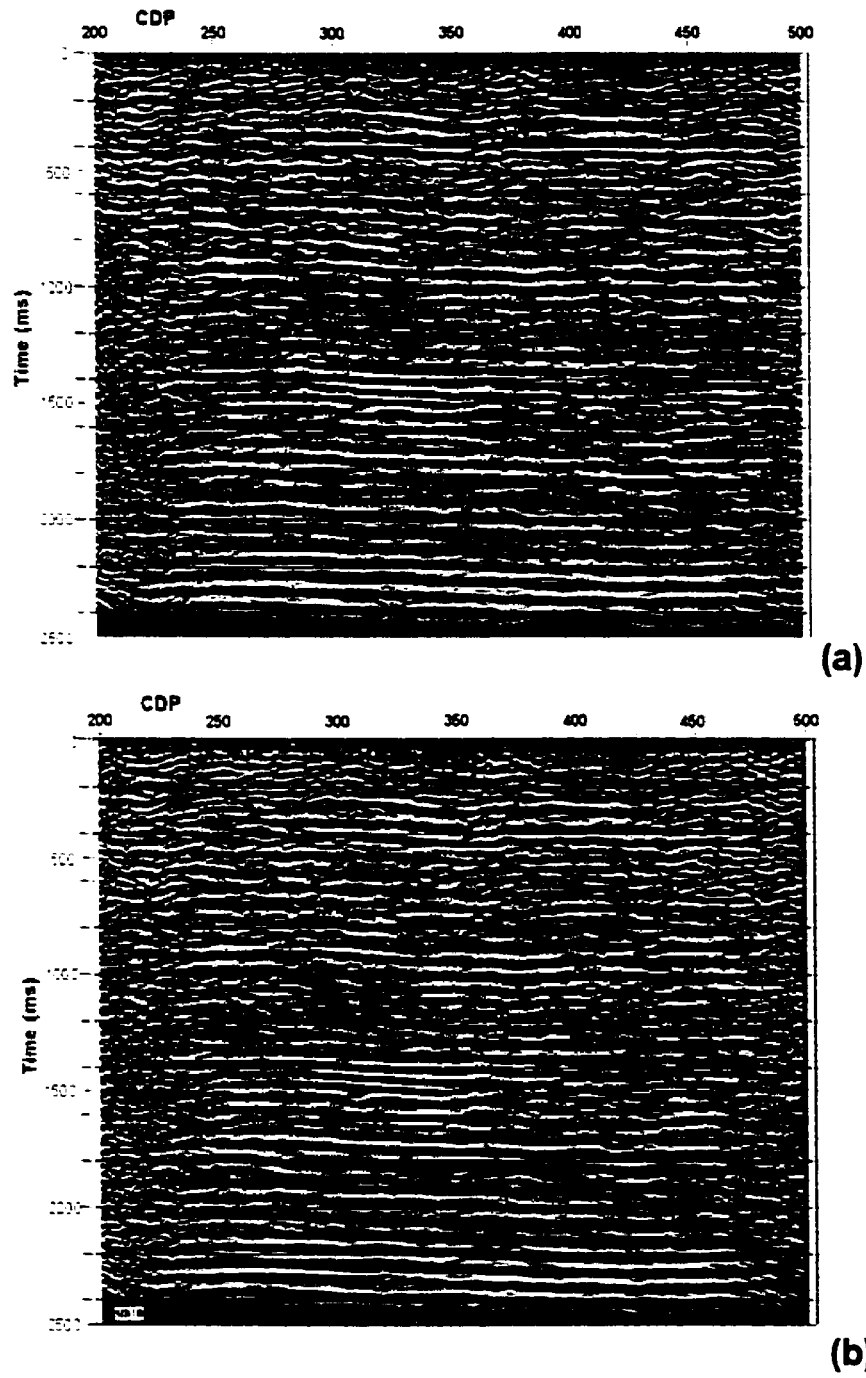

Figure 5.14: Comparison of *PS* stacked section after the application of the method. (a) without mode separation, and (b) with mode separation.

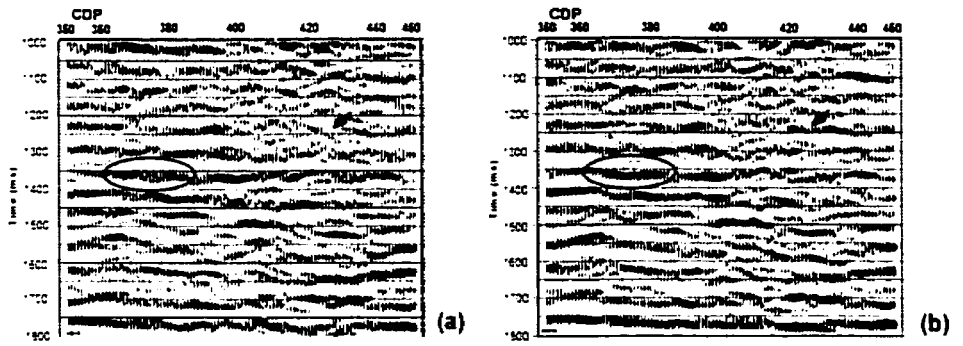

Figure 5.15. Close-up of the *PS* stacked section. (a) without mode separation. (b) with mode separation. Two examples of improvement are indicated.

The resulting *S*-wave sections are compared in Figures 5.14 and 5.15. Figure 5.15 is a close-up of Figure 5.14. Figures 5.14a and 5.15a show the result without mode separation and Figures 5.14b and 5.15b show the result with mode separation. Although the quality of the data is not homogeneous along the section, more continuity can be observed on some reflections after separation, as illustrated by the arrows in Figures 5.15a and 5.15b. These processing parameters are not designed over this data set, and the result could change for a more specific processing flow, e.g. with a new velocity field.

5.5. Discussion and Conclusions

A method to separate wave modes in the presence of statics proposed by Cary (1998) is tested in this chapter. *P* and *S*-wave statics corrections are used to obtain the NSL velocities, which are applied to calculate the free-surface response. With the free-surface response and the *P* and *S* waves statics corrections, least-squares inversion is applied in the τ-p domain to obtain the separate wave modes in frequency-space. The method is applied to synthetic and real data.

The following observations were noted:

(1) Application of the method to synthetic data show good results and appears to be robust with respect to errors in the velocity field.

(2) In real data, improvement can be observed in the stacked section. This improvement is attributable basically to the mode separation using the free-surface effect, which supports the benefits of this approach.

(3) Basic assumptions of the method are the plane wave approximation, the velocity field estimation (based on statics correction and an assumed NSL thickness), and the vertical angle of incidence to the surface.

(4) This method appears expensive in terms of computer resources; however, different calculation approaches can be tried to make it more efficient computationally.

(5) This approach establishes a relation between a number of parameters, namely, statics, free-surface response and the angle of incidence, which can be useful in overcoming other problems of multicomponent processing such as *S*-wave statics.

(6) More research can be done to obtain a more accurate NSL-velocities model. Additional extensions could be to include the NSL lateral thickness and topographic variations, as well as the 3-D free-surface response.

CHAPTER 6

CONCLUSIONS

6.1. Summary

In this thesis, effects of the near-surface layer (NSL) on land multicomponent seismic data are studied. The free-surface effect, phase changes of incident waves, angle of incidence, statics and wave mode cross-talk are considered, specially in relation with *PS* (converted) waves. Methods such as elastic modelling, polarization and least-squares inversion are applied.

Elastic-wave modelling was used to analyze a number of geologic models with and without a NSL. Variations in the models include horizontal reflectors, complex low-velocity NSL (LV-NSL), high-velocity NSL (HV-NSL), and dipping reflectors. From the results, the following observations are made:

(1) Phase change is associated more with the critical angle at the reflector than with the free-surface effect. The LV-NSL helps to reduce the offset at which these phase changes can occur and the angle of incidence with the surface can be almost vertical in cases where an LV-NSL exists. Phase changes caused by the free-surface effect may be possible at larger offsets, on events coming from steeply dipping layers, and in cases of high near-surface V_P/V_S values.

(2) In addition to ground-roll, other high-energy events can be generated at the NSL, e. g. reverberations, dispersive S waves and guided waves. These events depend on the elastic and geometrical properties of the layer, and also on the frequency spectrum of the incident wave.

Synthetic and real data are analyzed using polarization. Some observations are:

(1) The results obtained from the polarization analysis of FD modelling with one reflector are coherent and consistent, confirming theoretical expectations. On real data, high-

energy arrivals provide clearer polarization characteristics. These high-energy events are frequently generated at the NSL.

(2) Polarization analysis and filtering of complete gathers provided reasonable results. However, these results appear more qualitative than quantitative, since is difficult to evaluate specific details, such as phase changes and accurate polarization direction. These low accuracy results may be related to interference between seismic events, mainly generated at the NSL.

The relation between polarization direction of events generated at the NSL and the source-receiver azimuth was investigated. Horizontally polarized events are found to correlate fairly well with the geophone orientation as determined from the field geometry. It might be possible to develop a geophone orientation method based on these results.

Finally, a method for wave-mode separation in the presence of statics was tested. This method establishes a relation between *P*- and *S*- static corrections and the free-surface effect in a solution that uses least-squares inversion. The result obtained for the separation on a *PS*-wave section shows improved signal-to-noise ratio. This means that mode separation is a useful step that can help to improve information in multicomponent data. The velocity model of the NSL, which is needed for this method, was derived from the static corrections.

6.2. Discussion

As shown in this thesis, the effects of the NSL in multicomponent data (especially in the converted-wave method) are more complex than in the conventional *P*-wave method. In addition to the P-wave static corrections, used in the conventional processing method, the *S*-wave statics must also be accounted for in the multicomponent method. Furthermore, both the free- surface and the NSL affect the polarization of incident waves and the free-surface effect generates mode-leakage. Thus the NSL affects travel times, the signal-to-noise ratio and polarization information, all of which can diminish the quality of information that can be obtained.

An example of how the NSL can affect multicomponent information is shown in the use of land surface multicomponent data to evaluate anisotropy created by fractures. As pointed out by Crampin (1985), "...shear-wave polarizations carry much more information about the nature of the raypath (and the source) than is possible with the (nearly scalar) polarizations of *P*-waves" (p.142), and "..the surface imposes its own anomalies on the polarizations of the incident shear wave. This makes analysis of anisotropy-induced polarization anomalies particularly difficult at the free surface" (p. 143).

An improved method to obtain a more accurate model of the NSL would be instrumental in overcoming its deteriorating effects and obtaining a corrected wavefield. Some of the results of this thesis indicate that a more integrated approach, using different events and properties, may be beneficial. High-energy events generated in the NSL and detected with multicomponent geophones can provide useful information about the NSL. On the other hand, polarization methods, even qualitatively, allow analysis and filtering of that type of event. Also, in spite of uncertainties in the NSL velocity model and in the approximated wave propagation model, the mode-separation method in the presence of statics using least-squares inversion yields improved seismic sections. An integrated approach, possibly using inversion or imaging tools, would give a model of the NSL effect in time delays (statics) as in polarization change.

6.3. Future work

Additional work may be undertaken based on the results of this thesis. A number of areas for potential future work are identified below.

(1) The relation between geophone orientation and polarization could be investigated using multicomponent 3-D data. Seismic 3C-3D surveys with good field control and data from specifically designed experiments could be used to that end. Filtering of horizontally polarized events would facilitate this analysis. Use of different domains and events may help develop a practical method for geophone orientation using polarization.

(2) Some aspects have to be considered in polarization analysis. Vector fidelity (independence of polarization on geophone characteristics) should be taken into account to obtain reliable results. Interference between events is a drawback for polarization analysis: some methods that take this interference into account have been developed for VSP and could be the basis for methods applied to surface data (e.g. Cho and Spencer, 1992). Finally, the power of stacking can help to enhance polarization information.

(3) Other inversion algorithms can be tested with the method for mode separation in the presence of statics proposed by Cary (1998), to improve its computational performance. A method to obtain a more accurate velocity and thickness NSL model would be also beneficial. The algorithm could also be extended to obtain information on the receiver (*PS*) statics. Mode separation in 3-D would be also a useful extension, as proposed by Cary (1998).

(4) More detailed studies of the NSL could be done to understand its behaviour. It may include modeling with rough topography and variable NSL velocity, as well as field tests. A method to obtain a velocity model for the NSL is required, since it would benefit mode separation in the presence of statics, statics and free-surface effect analysis. (There is work on that area using inversion, e.g. Gabriels et al., 1987).

(5) Application of inversion methods (maybe least-squares inversion) might be a fruitful approach to obtain a more complete image of the NSL.

(6) Anelastic and anisotropic models would complete a theoretical framework for more advanced investigations.

REFERENCES

Achenbach, J. D., 1984, Wave propagation in elastic solids: Elsevier, 2nd edition (First edition: 1973).

Alford, R. M., 1986, Shear data in the presence of azimuthal anisotropy: Dilley, Texas: SEG 56th Ann. Internat. Mtg. Expanded Abstracts, 476-479.

Anno, P. D., 1987, Two critical aspects of shear-wave analysis: statics solutions and reflection correlations, *in* Danbom, S. H. and Domenico, S. N., Editors, Shear wave exploration: SEG Geophysical development series, Vol. 1.

Bates, R. L. and Jackson, J. A., 1984, Dictionary of geological terms: Doubleday, 3rd Edition. (American Geological Institute).

Bland, H. C., Lu, H. X., Stewart R. R. and Hoffe, B., 1998, The Shaganappi 3C-3D survey: CREWES research report, Vol. 10, 34.1.

Bland, H. C. and Stewart R. R., 1996, Geophone orientation, location, and polarity checking for 3-C seismic surveys: CREWES Research Report, Vol. 8, 3-1.

Boas, M. L.,1983, Mathematical methods in the physical sciences: John Wiley and Sons, 2nd edition (First edition: 1966).

Boore, D. M., 1972, Finite difference methods for seismic wave propagation in heterogeneous materials, *in* Bolt, B. A., *Ed.*, Methods in computational physics: Vol. 11, Seismology: surface waves and earth oscillations, Academic Press, 1972.

Born, M. and Wolf, E., 1965, Principles of optics: Pergamon Press Inc., New York.

Buchen, P., 1971, Plane waves in viscoelastic media: Geophys. J. R. astr. soc., **23**, 531-542.

Cary, P. W., 1994, 3D converted-wave seismic processing: CREWES research report, Vol. 6, 31.1-3.10

Cary, P. W., 1998, P/S wavefield separation in the presence of statics: CREWES research report, Vol. 10, 30.1 – 30.8.

Cary, P. W. and Eaton, D. W. S., 1993, A simple method for resolving large converted wave (P-SV) statics: Geophysics, **58**, 429-433.

Cieslewicz, D., 1999, Near surface seismic characterization using three-component buried geophones: M. Sc. Thesis, Department of Geology and Geophysics, University of Calgary.

Cho. W. H. and Spencer. T. W.. 1992. Estimation of polarization and slowness in mixed wavefields: Geophysics. **57**. 805-814.

Cox. M.. 1999. Static corrections for seismic reflection surveys: SEG Geophysical references Series. Vol. 9.

Crampin. S.. 1985. Evaluation of anisotropy by shear-wave splitting: Geophysics. **50**. 142-152.

Dankbaar. J. W. M.. 1985. Separation of P- and S- waves: Geophysical Prospecting. **33**. 970-986.

Dasios. A.. McCann. C.. Astin. T. R.. McCann. D. M.. and Fenning. P.. 1999. Seismic imaging of the shallow subsurface: shear-wave case histories: Geophysical Prospecting. Vol. 47. 565-591.

Devaney. A. J. and Oristaglio. M. L.. 1986. A plane-wave decomposition for elastic wave fields applied to the separation of *P*-waves and *S*-waves in vector seismic data: Geophysics. **51**. 419–423.

DiSiena. J. P.. Gaiser. J. E. and Corrigan. D.. 1984. Horizontal components and shear wave analysis of three-component VSP data. *in* Toksoz. N. and Stewart R. R.. Editors. Vertical seismic profiling: advanced concepts: Geophysical Press. Vol. 15 B.

Donati. M.. 1996. P- and S- wave separation using three component modal filters: M. Sc. Thesis. The University of Calgary. Department of Geology and Geophysics.

Donati. M. S. and Stewart. R. R.. 1996. P- and S-wave separation at a liquid-solid interface: Journal of seismic exploration. **5**. 113-127.

Douma. J. and Helbig. K.. 1987. What can the polarization of shear waves tell us?: First Break. **5**. 95-104.

Dufour. J. and Lawton. D.. 1996. Refraction analysis of the Blackfoot 2D-3C data: CREWES Research Report. Vol. 8. 14.1 – 14.32.

Dunne. J. and Beresford. G.. 1995. A review of the τ-p transform. its implementation and its application in seismic processing: Exploration Geophysics. **26**. 19-36.

Eaton. D. W. S.. 1989. The free surface effect: implications for amplitude-versus-offset inversion: Canadian Journal of Exploration Geophysics. **25**. 97-103.

Esmersoy. C.. 1990. Inversion of P and SV waves from multicomponent offset vertical seismic profiles: Geophysics. **55**. 39-50.

Evans. R.. 1984. Effects of the free surface on shear wavetrains. Geophysical Journal of the Royal Astronomical Society. **76**. 165-172.

Flinn. E. A.. 1965. Signal analysis using rectilinearity and direction of particle motion: Proceed. IEEE. **53**. 1874-1876.

Gabriels. P.. Snieder. R. and Nolet.G.. 1987. In situ measurements of shear-wave velocity in sediments with higher-mode Rayleigh waves: Geophysical Prospecting. **35**. 187-196.

Galperin. E. I.. 1974. Vertical seismic profiling: SEG Special publication No. 12. (Originally published in Russian by Nedra. Moscow. 1971)

Galperin. E. I.. 1984. The polarization method of seismic exploration: D. Reidel Publishing Company. (Originally published in Russian by Nedra. Moscow. 1977)

Hamarbitan. N. S. and Margrave. G. F.. 1996. An investigation of the free surface effect: CREWES Research Report. Vol. 8. 16.1-16.20.

Hearn. S. and Hendrick. N.. 1999. A review of single-station time-domain polarisation analysis techniques: Journal of Seismic Exploration. **8**. 181-202.

Helbig. K.. 1987. Shear waves–what they are and how can they be used. *in* Danbom. S. H. and Domenico. S. N.. *Editors*. Shear wave exploration: SEG Geophysical development series. Vol. 1.

Hoffe. B.. Stewart. R. R.. Bland. H. C.. Gallant E. V. and Bertram. M.. 1998. The Blackfoot high-resolution seismic survey: design and initial results: SEG 68th Annual Meeting Expanded Abstracts. 103-106.

Kanasewich. E. R.. 1975. Time sequences analysis in geophysics: The University of Alberta Press. Edmonton.

Kähler. S. and Meissner. R.. 1983. Radiation and receiver pattern of shear and compressional waves as a function of Poisson's Ratio: Geophysical Prospecting. **31**. 421-435.

Karl. J. H.. 1989. An introduction to digital signal processing: Academic Press.

Knopoff. L.. Fredricks. R. W.. Gangi. A. F. and Porter. L. D.. 1957. Surface amplitudes of reflected body waves: Geophysics. **22**. 842-847.

Krebes. E.. 1989. Seismic theory and methods: Course notes. University of Calgary.

Lawton. D. and Bertram M.. 1993. Field test of 3-component geophones: Canadian Journal of Exploration Geophysics. **29**. 125-131.

Levander, A., 1988, Fourth-order finite-difference P-SV seismograms: Geophysics, **53**, 1425-1436.

Lines, L. R. and Treitel, S., 1984, Tutorial: a review of least-squares inversion and its application to geophysical problems: Geophysical Prospecting, **32**, 159-186.

Lu, H. and Margrave, G. F., 1999, Study of the multiple mode conversion of the Blackfoot 3C seismic data: CREWES Research Report, Vol. 11.

MacBeth, C. and Crampin, S., 1991, Comparison of signal processing techniques for estimating the effects of anisotropy: Geophysical Prospecting, **39**, 357-385.

Macelwane, J. B. and Sohon, P. W., 1936, Introduction to theoretical seismology: John Wiley and Sons.

Margrave, G. F., 1998, Seismic processing course notes: University of Calgary, Dept. of Geology and Geophysics.

Meissner, R., 1965, P- and SV- waves from uphole shooting: Geophysical Prospecting **13**, 433-459.

Mercado, E. J., 1968, Linear phase filtering of multicomponent seismic data: Geophysics, **33**, 926-935.

Molotova, L. V. and Vassil'ev, Y. I., 1960, Velocity ratio of longitudinal and transverse waves in rocks, II: Bulletin of the Academy of Sciences USSR - Geophysics Series, 731-743 (Translated by AGU).

Montalbetti, J. and Kanasewich E., 1970, Enhancement of teleseismic body waves with a polarization filter: Geophys. J. R. Astr. Soc., **21**, 119-129.

Mueller, M. C., Barkved, O. I. and Thomsen, L., 1999, A strategy for vector interpretation of multicomponent ocean bottom seismic data: 61st EAGE conference Extended Abstracts, Vol. 1, No. P-067.

Nuttli, O., 1961, The effect of the earth surface on the *S* wave particle motion: Bulletin of the Seismological Society of America, **51**, 227-246.

Perelberg, A.I. and Hornbostel, S.C., 1994, Applications of seismic polarization analysis: Geophysics, **59**, 119-130.

Samson, J. C., 1977, Matrix and Stokes vector representations of detectors of polarized waveforms: theory, with some applications to teleseismic waves: Geophys. J. R. astr. Soc., **51**, 583-603.

Sheriff, R. E., 1991, Encyclopedic dictionary of exploration geophysics: SEG Geophysical Reference Series 1, 3rd edition.

Sheriff. R. E. and Geldart. L. P.. 1995. Exploration seismology: Cambridge University Press. 2nd edition.

Shieh. C. F.. and Herrmann. R. B.. 1990. Ground roll: rejection using polarization filters: Geophysics. **55**. 1216-1222.

Smith. B. D. and Ward. S. H.. 1974. On the computation of polarization ellipse parameters: Geophysics. **39**. 867-869.

Stewart. R. R. and Lawton D. C. 1996. P-S seismic exploration: a midterm overview: CREWES research report. Vol. 8. 1.1-1.33.

Stoffa. P. L.. Buhl. P.. Diebold. J. and Wenzel. F.. 1981. Direct mapping of seismic data to the domain of intercept time and ray parameter – a plane-wave decomposition: Geophysics. **46**. 255-267.

Stümpel. H.. Kähler. S.. Meissner. R. and Milkereit. B.. 1984. The use of seismic shear waves and compressional waves for lithological problems of shallow sediments: Geophysical Prospecting. **32**. 663-675.

Tatham. R. H and Goolsbee. D. V.. 1984. Separation of *S*-wave and *P*-wave reflections offshore western Florida: Geophysics. **49**. 493-508.

Tatham. R. H. and McCormack. M. D.. 1991. Multicomponent seismology in petroleum exploration: SEG. Investigations in Geophysics. Vol. 6.

Tree. E. L.. 1999. The vector infidelity of the ocean bottom multicomponent seismic acquisition system: EAGE 61st Conference Extended Abstracts. No. 6-19.

Turner. G.. 1990. Aliasing in the tau-*p* transform and the removal of spatially aliased coherent noise: Geophysics. **55**. 1496-1503.

Vidale. J. E.. 1986. Complex polarization analysis of particle motion: Bulletin of the Seismological Society of America. **76**. 1393-1405.

Wiest. B. and Edelmann. H. A. K.. 1984. Static corrections for shear wave sections: Geophysical Prospecting. **32**. 1091-1102.

Winterstein. D. F.. 1990. Velocity anisotropy terminology for geophysicists: Geophysics. **55**. 1070-1088.

Zheng. Y.. 1995. Seismic polarization filtering: noise reduction and off-line imaging: M. Sc. Thesis. The University of Calgary. Department of Geology and Geophysics.

APPENDIX A

OVERVIEW AND NOMENCLATURE FOR ELASTIC WAVE PROPAGATION.

This appendix is intended to give a basic overview of the theoretical framework of the elastic waves theory and term definition, useful for many of the topics developed in the thesis. General references Macelwane and Sohon (1936), Achenbach (1984), Krebes (1989), and Sheriff and Geldart (1995). A reference for the basic mathematics involved is Boas (1965).

Elastic wave propagation theory is a part of continuum mechanics. The model of the medium where the elastic phenomena occur is the "continuum". We divide the "continuum" into infinitesimally small cubes such that each side is orthogonal to one of the orthogonal Cartesian axis. Then the equation that describes wave propagation in elastic solids is inferred from the Second Newton's law and the Hooke's law.

Let

x_1, x_2, x_3 , the Cartesian coordinate axes.

ρ , the mass density (mass per volume unit).

τ_{ij} , the stress in direction j over the face normal to axis x_i.

u_i , the strain in direction x_i .

f_i , the component in direction x_i of the external force.

Then, applying the second Newton's Law, $F=ma$, where m is the mass and a the acceleration, it results the *Cauchy's Equation of Motion*:

$$\rho \frac{\partial^2 u_i}{\partial t^2} = f_i + \left(\frac{\partial \tau_{1i}}{\partial x_1} + \frac{\partial \tau_{2i}}{\partial x_2} + \frac{\partial \tau_{3i}}{\partial x_3} \right) \qquad i=1,2,3 \qquad \text{(A.1)}$$

The Hooke's Law assumes a linear relation between force and deformation (or stress and strain in this case), which implies *elastic constants*, properties of the material that relate stress and strain. If the medium is assumed homogeneous and isotropic two independent elastic constants are required, and the relations are

$$\tau_{ij} = \mu\left(\frac{\partial u_i}{\partial x_j} + \frac{\partial u_j}{\partial x_i}\right) \qquad \text{(A.2.a)}$$

if $i \neq j$ (that is to say if the stress is tangent to the face), and

$$\tau_{ii} = \lambda\left(\frac{\partial u_1}{\partial x_1} + \frac{\partial u_2}{\partial x_2} + \frac{\partial u_3}{\partial x_3}\right) + 2\mu\frac{\partial u_i}{\partial x_i} \qquad \text{(A.2.b)}$$

if $i = j$ (that is to say, if the stress is normal to the face)

From (A.1) and (A.2), the wave equation in an elastic homogeneous isotropic results:

$$(\lambda+\mu)\frac{\partial}{\partial x_i}\left(\frac{\partial u_1}{\partial x_1} + \frac{\partial u_2}{\partial x_2} + \frac{\partial u_3}{\partial x_3}\right) + \mu\left(\frac{\partial^2 u_i}{\partial x_1^2} + \frac{\partial^2 u_i}{\partial x_2^2} + \frac{\partial^2 u_i}{\partial x_3^2}\right) = \rho\frac{\partial^2 u_i}{\partial t^2} \qquad \text{(A.3)}$$

where i = 1, 2, 3.

A particular solution of the wave equation (A.3) is a plane wave:

$$\vec{u} = f(\vec{x}\cdot\vec{n} - Vt)\vec{d} \qquad \text{(A.4)}$$

where V is the velocity, and

$\vec{u}$ = displacement of the particle.

$\vec{x}$ = position vector

$\vec{n}$ = unit vector in the direction of the wave propagation (*propagation vector*). This is the Director Cosines vector with respect to the axes.

$\vec{d}$ = unit vector in the direction of the particle displacement (*polarization vector*).

In plane waves for a time t the displacement is the same at all the points with $\vec{x}\cdot\vec{n}$ constant, which corresponds to a plane normal to the wave direction of propagation (Achenbach, 1973, p. 122). Although wave fronts are more or less spherical in principle,

in the far field they may assume to be plane. Also other waveforms can be considered a synthesis of plane waves.

Replacing (A.4) in (A.3) two solutions are possible. which implies

$$V = \sqrt{\frac{\lambda + 2\mu}{\rho}} \equiv V_P \qquad \text{(A.5).}$$

or

$$V = \sqrt{\frac{\mu}{\rho}} \equiv V_S \qquad \text{(A.6).}$$

Equation A.4 corresponds to the velocity of a *P* (Primary) wave. also known as pressure. longitudinal or irrotational wave. whose direction of polarization is the same as the direction of propagation.

Equation A.6 corresponds to an *S* (Secondary) wave. also known as shear. transverse or equivoluminal wave. whose direction of polarization is perpendicular to the direction of propagation.

According to the Fourier Theory. a transient signal is a composite of harmonic sinusoids (Boas. 1965). The analysis of simple a sinusoid is the basis for the analysis of almost any signal. using Fourier methods.

An harmonic sinusoid is represented by:

$$\vec{u} = A\cos[k(\vec{x}\cdot\vec{n} - Vt)]\vec{d} \qquad \text{(A.7)}$$

where $i = \sqrt{-1}$

$\vec{n}$ = direction of propagation

A = amplitude

k = wavenumber (spatial frequency).

Harmonic waves are a particular case of plane waves. then equations A.5 and A.6 can be applyied

It is possible to define the *temporal frequency* $\equiv \omega = kV$. such that $k = \frac{\omega}{V}$. then an alternative representation of harmonic waves is

$$\vec{u} = A\cos\left[\omega\left(\frac{\vec{n}}{V}\cdot\vec{x} - t\right)\right]\vec{d} = A\cos[\omega(\vec{s}\cdot\vec{x} - t)]\vec{d}\,.$$

The ratio $\frac{\vec{n}}{V}$ is known as the *slowness vector*, represented by $\vec{s}$.

In the 2-D case, assuming x_1 the horizontal axis and x_2 the vertical one (see Fig. A.2),

$$\vec{s}\cdot\vec{x} = \frac{\cos(90-\theta_2)}{V}x_1 + \frac{\cos\theta_2}{V}x_2 = \frac{\sin\theta_2}{V}x_1 + \frac{\cos\theta_2}{V}x_2\,.$$

According to the Euler's Formula (Boas, 1965, Ch. 2.):

$e^{i\theta} = \cos\theta + i\sin\theta$, where $i = \sqrt{-1}$, then

For mathematical convenience, equation A.7 can be represented in complex form as:

$$\vec{u} = A\exp[ik(\vec{x}\cdot\vec{n} - Vt)]\vec{d} = A\exp[i\omega(\vec{s}\cdot\vec{x} - t)]\vec{d}\,. \qquad \text{(A.8)}$$

Incidence of a plane wave to the surface of the earth is illustrated in Figure A.1.

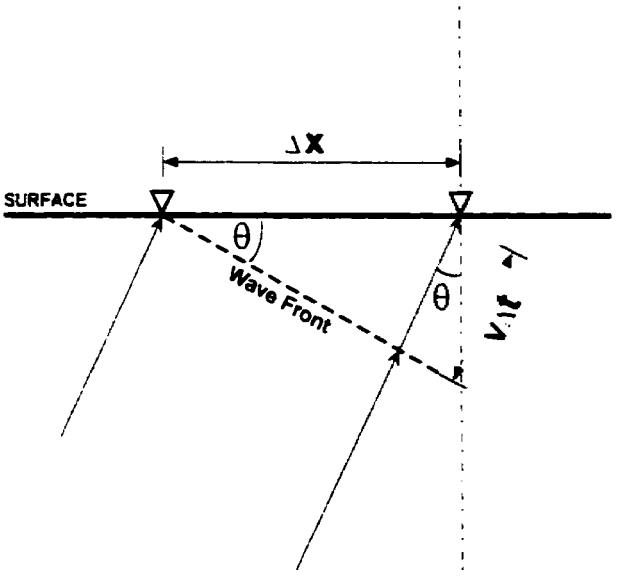

Figure A.1. The plane wave approximation.

Plane waves can be defined in terms of the *ray parameter* or *apparent slowness*, p, which is the component of the slowness vector $\vec{s}$ in the axis perpendicular to the earth surface. This parameter is used to describe plane waves, and is defined as

$$p = \frac{\sin\theta}{V}, \qquad \text{(A.9)}$$

where θ is the incidence angle and V the wave velocity, or, equivalently,

$$p = \frac{\Delta t}{\Delta x}. \qquad \text{(A.10)}$$

where, for a specific event, Δt is the time change corresponding to an space change Δx.

APPENDIX B

MATHEMATICAL ASPECTS OF POLARIZATION ANALYSIS

As defined by Sheriff (1991), polarization is the preferential direction of motion involved in seismic wave passage. Theoretical concepts for polarization analysis have been developed in association with electromagnetic waves propagation (e. g. Born and Wolf, 1965). This Appendix follows partially Kanasewich (1975), however the physical meaning is emphasised instead of following rigorous details.

In the following, the vibration of a particle or point in the 2-D space is described. In general, the motion of a particle under the action of a wave can be approximated to an ellipse. A description of the polarization ellipse parameters is in Smith and Ward, 1974. The components of the two-dimensional wave shape are considered harmonic sinusoids in time (monochromatic wave). The wave can be represented by

$$\vec{u} = A\cos[k(\vec{x}\cdot\vec{n} - Vt)]\vec{d}\,.$$

The shape of the ellipse is controlled by the phase difference between the components. Supposing that there is a phase shifting in the two components, δ_i, and if we define

$$\tau = k(\vec{x}\cdot\vec{n} - Vt)$$

then the two components are

$$u_1 = A_1\cos(\tau + \delta_1) \qquad \text{(B.1.a)}$$

and $$u_2 = A_2\cos(\tau + \delta_2) \qquad \text{(B.1.b).}$$

Making use of the trigonometric identities

$$\cos(\tau \pm \delta_i) = \cos\tau\cos\delta_i \mp \sin\tau\sin\delta_i$$

$$\sin(\tau - \delta_i) = \sin\tau\cos\delta_i - \cos\tau\sin\delta_i$$

and after some algebra, an equation independent of time results:

$$\frac{u_1^2}{A_1^2} + \frac{u_2^2}{A_2^2} - 2\frac{u_1u_2}{A_1A_2}\cos(\delta_2 - \delta_1) = \sin^2(\delta_2 - \delta_1) \qquad \text{(B.2)}$$

This is the equation of an ellipse, illustrated in Figure B.1.

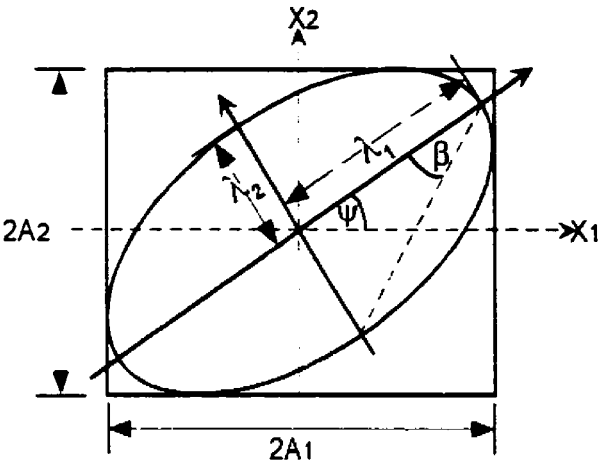

Figure B.1. Polarization ellipse. The components are x_1 and x_2, the corresponding amplitudes are A_1 and A_2, and λ_1 and λ_2 are the semi-major and semi-minor axes.

Representing the phase difference as:

$$\delta = \delta_2 - \delta_1$$

Equation B.2 can be written in matrix form as:

$$\begin{bmatrix} u_2 & u_1 \end{bmatrix} \begin{bmatrix} A_1^2 & -A_1 A_2 \cos\delta \\ -A_1 A_2 \cos\delta & A_2^2 \end{bmatrix} \begin{bmatrix} u_2 \\ u_1 \end{bmatrix} = A_1 A_2 \sin^2 \delta \qquad \text{(B.3)}$$

The phase difference δ defines the ellipticity. The relation between phase difference and ellipticity is illustrated in figure B.2.

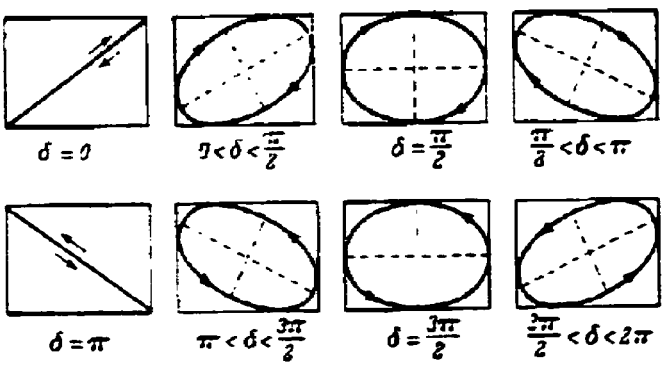

Figure B.2. Phase differences and ellipticity. The phase difference in radians is δ. (from Born and Wolf, 1965)

We can define:

$$\underline{\underline{S}} = \begin{bmatrix} A_1^2 & -A_1 A_2 \cos\delta \\ -A_1 A_2 \cos\delta & A_2^2 \end{bmatrix} \quad \text{and} \quad \underline{\underline{E}} = \begin{bmatrix} u_2 \\ u_1 \end{bmatrix}$$

Then equation B.3 can be represented as:

$$\underline{\underline{E}}^T \underline{\underline{S}} \underline{\underline{E}} = A_1 A_2 \sin^2\delta$$

It can be shown (e.g. Boas, 1965, Chapter 10) that the matrix $\underline{\underline{S}}$ can be diagonalized using eigenvalues and eigenvectors.

Defining

$\lambda_1, \lambda_2 \equiv$ the eigenvalues, and

$$\underline{t}_1 = \begin{bmatrix} t_{11} \\ t_{21} \end{bmatrix} \quad \text{and} \quad \underline{t}_2 = \begin{bmatrix} t_{12} \\ t_{22} \end{bmatrix} \equiv \text{the corresponding eigenvectors, thus}$$

$$\underline{\underline{T}} = \begin{bmatrix} t_{11} & t_{12} \\ t_{21} & t_{22} \end{bmatrix} \quad \text{and} \quad \underline{\underline{\lambda}} = \begin{bmatrix} \lambda_1 & 0 \\ 0 & \lambda_2 \end{bmatrix}.$$

So the diagonalization procedure is symbolized by:

$$\underline{\underline{T}}^T \underline{\underline{S}} \underline{\underline{T}} = \underline{\underline{\lambda}}$$

The eigenvalues are the semi-major and semi-minor axes of the ellipse (Fig. B.1). This procedure is equivalent to a rotation of the ellipse to its principal axis, according to the angles defined by the eigenvectors.

The polarization parameters, that is to say the ellipticity and the angle of direction, are defined as a function of the amplitudes and the phase difference of the components (Born and Wolf, 1965).

The direction angle ψ (Fig. B.1) is given by

$$\tan 2\psi = \frac{2A_1 A_2}{A_1^2 - A_2^2} \cos\delta \qquad \text{(B.4)}$$

The ratio of the minor axis to the major axis or ellipticity (Fig. B.1) is given by:

$$\tan\beta = \pm\frac{\lambda_1}{\lambda_2} \qquad \text{(B.5)}$$

where β is given by:

$$\sin 2\beta = \frac{2A_1A_2}{A_1^2 + A_2^2}\sin\delta \qquad \text{(B.6)}$$

The sign in (B.5) defines the direction of the particle motion (clockwise if positive or counter-clockwise if negative.)

If the wave is not harmonic amplitude and phase can vary with time, then a statistical method is applied. Instead of the matrix $\underline{\underline{S}}$ is used the so-called *coherence matrix*, which relates amplitudes along a data window. In the time domain this matrix is the *covariance matrix* (Montalbetti and Kanasewich, 1971).

$$\underline{\underline{C}} = \begin{bmatrix} \text{var}(u_1) & \text{cov}(u_1, u_2) \\ \text{cov}(u_2, u_1) & \text{var}(u_2) \end{bmatrix} \qquad \text{(B.7)}$$

where

$$\text{cov}(u_i, u_j) = \frac{1}{N}\sum_{n=1}^{N}[u_i(n) - \mu_i][u_j(n) - \mu_j]$$

being $N \equiv$ the number of samples.

$\mu_i \equiv$ the mean of the variable i.

and:

$$\text{var}(u_i) = \text{cov}(u_i, u_i)$$

In the frequency domain is known as the spectral matrix (e. g. Shieh and Herrmann, 1990; Born and Wolf, 1965).

In three dimensions the matrix B.7 becomes:

$$\text{cov} = \begin{pmatrix} \text{var}[H1] & \text{cov}[H1, H2] & \text{cov}[H1, H3] \\ \text{cov}[H1, H2] & \text{var}[H2] & \text{cov}[H2, H3] \\ \text{cov}[H1, H3] & \text{cov}[H2, H3] & \text{var}[H3] \end{pmatrix} \qquad \text{(B.8)}$$

from which corresponding 3-D equations can be derived. This coherence matrix generates an approximation, in the least-squares sense, to an ellipse.

APPENDIX C

THE FREE-SURFACE EFFECT

The solution of the 2-D free-surface conditions for plane incident *P* and *S* waves, supposing isotropic homogeneous medium, is presented. This is a particular case of the Zoeppritz equations, and is known as the *free-surface effect* or *geophone response*. References about the free-surface effect can be found in Knopoff et al. (1957); Nuttli, (1961); Meissner, (1965); and Evans, (1984). A 3-D solution can be found in Kähler and Meissner, (1983).

P or *S* waves incident to the earth's surface from deeper reflectors originate reflected and converted waves, depending on the arrival direction and the elastic properties of the near surface. These seismic events, when detected by seismometers or geophones generate a response on them. The analysis of the free-surface response considering the 2-D case (horizontal and vertical response directions) and plane wave incidence, assuming an isotropic homogeneous medium, is presented in the following.

Incident *P* wave generates reflections of *P* wave and converted *S* wave. Similarly incident *S* wave generates reflections of *S* waves and converted *P* waves. The two conditions to be satisfied are stress and displacement equilibrium, namely

1. The displacement caused by the incidence of a plane wave is the result of the incident and the reflected waves displacements.

2. The resulting stresses at the free surface are zero.

Figures C.1 illustrates the geometry and the terms for incident *P*- and *S*- wave.

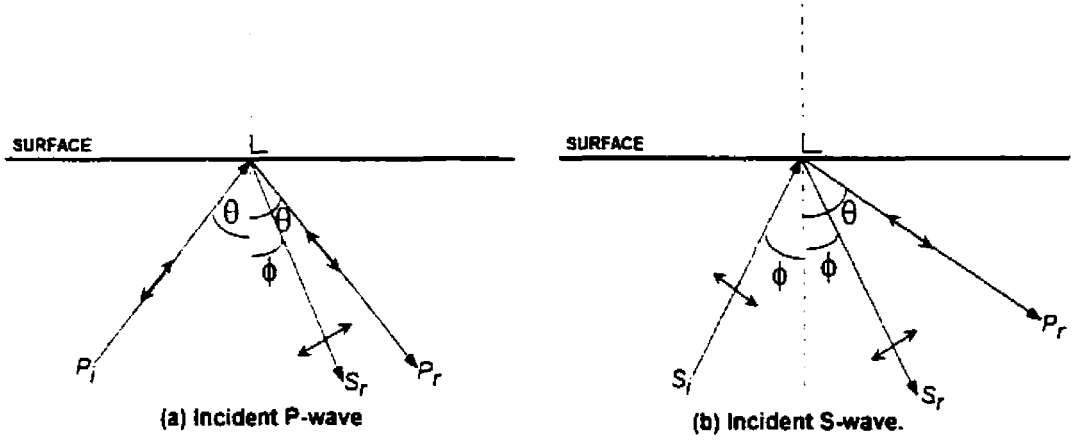

Figure C.1. Free-surface events response nomenclature in the case of (a) incident P-wave and (b) incident S-wave. Each one of them generates converted waves of the other type.

The two coordinate axes are x and z. The x-axis is positive to the right and the z axis is positive down into the earth. Without losing generality, the incidence point is assumed to be at the origin of coordinates (x=0 and z=0). When convenient the axes are identified by sub-indexed numbers.

$[x,z]=[x_1,x_2]$ or in general, x_i with i=1,2

Assuming a harmonic plane wave, the displacement is represented by:

$$\vec{u} = A\exp(i\omega(\vec{s}\cdot\vec{x}-t))\vec{d} \qquad \text{(C.1)},$$

where $A \equiv$ Amplitude, $\omega \equiv$angular frequency, $t \equiv$time, $i = \sqrt{-1}$, $\vec{s}=[s_x,s_z] \equiv$the slowness vector, $\vec{x}=[x,z] \equiv$the position vector, and $\vec{d}=[d_x,d_z] \equiv$the polarization vector.

The slowness vector is defined by

$$\vec{s} = \frac{1}{V}\vec{n},$$

where V is the wave velocity and $\vec{n}=[n_x,n_z]$ is the unitary vector of the propagation direction, with n_x, n_z the director cosines in the x and z directions.

In the case of the x-axis, $s_x = \frac{n_x}{V} = p$, that is, the *ray parameter* or *apparent slowness*, also defined as

$$p = \frac{\sin\theta}{V_P} = \frac{\sin\phi}{V_S} \qquad \text{(Snell's law)} \qquad \text{(C.2).}$$

For 2-D incidence and reflection of *P*- and *S*- waves (see Fig. 2), the vectors $\vec{n}$ and $\vec{d}$ are in table C.1

Table C.1. Angles of propagation and particles displacement

	n_x	n_z	d_x	D_z
Incident P	sin θ	-cos θ	sin θ	-cos θ
Reflected P	sin θ	cos θ	sin θ	cos θ
Incident S	sin ϕ	-cos ϕ	cos ϕ	sin ϕ
Reflected S	sin ϕ	cos ϕ	cos ϕ	-sin ϕ

Case 1: Incident P-wave:

From the condition 1 (displacements).

$$u_z = u_{IP}(-\cos\theta) + u_{RP}\cos\theta + u_{RS}(-\sin\phi) \qquad \text{(C.3.a)}$$

and

$$u_x = u_{IP}\sin\theta + u_{RP}\sin\theta + u_{RS}\cos\phi \qquad \text{(C.3.b)}$$

where

$u_{PI} = A_{PI}\exp(i\omega(\vec{s}\cdot\vec{x} - t))$. incident P-wave (= *PI*).

$u_{PR} = A_{PR}\exp(i\omega(\vec{s}\cdot\vec{x} - t))$. reflected P-wave (= *PR*).

$u_{SR} = A_{SR}\exp(i\omega(\vec{s}\cdot\vec{x} - t))$. reflected S-wave (= *SR*).

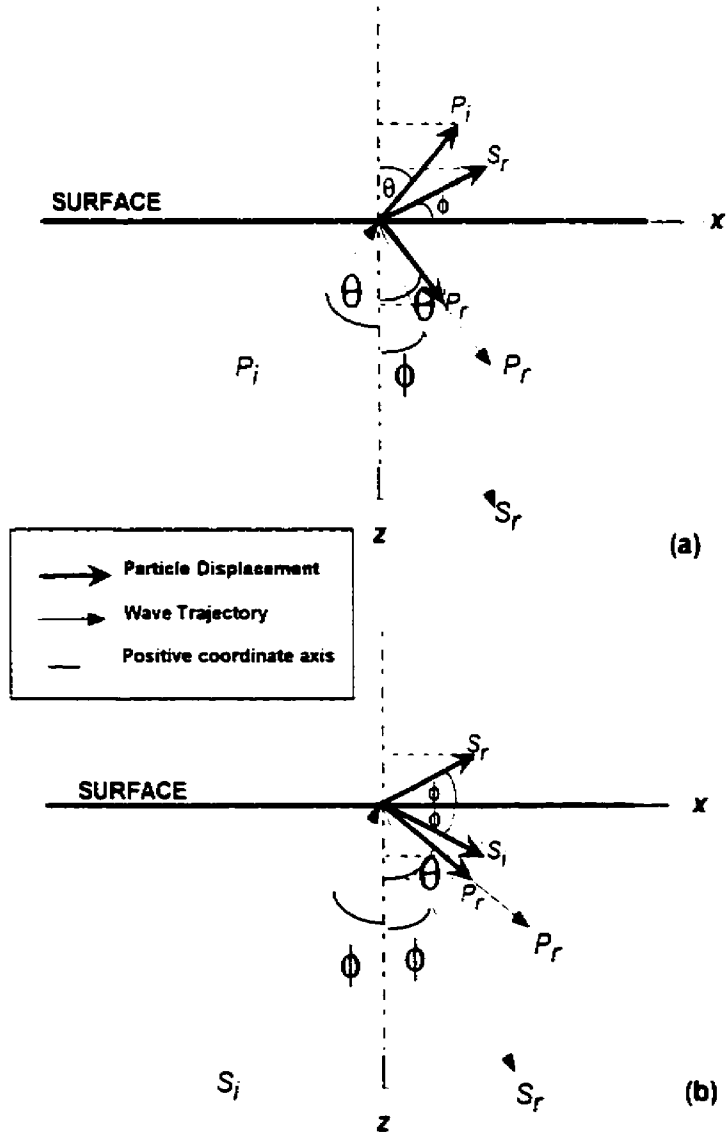

Figure C.2. Free-surface displacement and wave propagation vectors. (a) Incident *P* wave (b) Incident *S* wave. The particle displacement is $u\vec{d}$ where $\vec{d}$ is the displacement direction: the wave trajectory is illustrated by the slowness $\vec{s} = \vec{n}_{V}$. The sub-index *i* corresponds to incident wave and the sub-index *r* to reflected wave.

From the stresses condition (condition 2):

$$\sum \tau_{\sqsubset} = 0 = \tau_{\sqsubset}^{IP} + \tau_{\sqsubset}^{RP} + \tau_{\sqsubset}^{RS} \qquad \text{(C.4.a)}$$

$$\sum \tau_{zz} = 0 = \tau_{zz}^{IP} + \tau_{zz}^{RP} + \tau_{zz}^{RS} \qquad \text{(C.4.b)}$$

From the equation A.2 . Appendix A.

$$\tau_{xz} = \mu\left(\frac{\partial u_x}{\partial z} + \frac{\partial u_z}{\partial x}\right)$$

$$\tau_{zz} = \lambda\left(\frac{\partial u_x}{\partial x} + \frac{\partial u_z}{\partial z}\right) + 2\mu\frac{\partial u_z}{\partial z}$$

then

$$\sum \tau_{xz} = \mu\left\{\left[\frac{\partial u_x}{\partial x} + \frac{\partial u_z}{\partial x}\right]_{PI} + \left[\frac{\partial u_x}{\partial x} + \frac{\partial u_z}{\partial x}\right]_{PR} + \left[\frac{\partial u_x}{\partial x} + \frac{\partial u_z}{\partial x}\right]_{SR}\right\}=0. \qquad \text{(C.5.a)}$$

and

$$\sum \tau_{zz} = \lambda\left\{\left[\frac{\partial u_x}{\partial z} + \frac{\partial u_z}{\partial x}\right]_{PI} + \left[\frac{\partial u_x}{\partial z} + \frac{\partial u_z}{\partial x}\right]_{PR} + \left[\frac{\partial u_x}{\partial z} + \frac{\partial u_z}{\partial x}\right]_{SR}\right\}$$

$$+ 2\mu\left\{\left[\frac{\partial u_z}{\partial z}\right]_{PI} + \left[\frac{\partial u_z}{\partial z}\right]_{PR} + \left[\frac{\partial u_z}{\partial z}\right]_{SR}\right\} = 0 \qquad \text{(C.5.b)}$$

As in general. from Eq. C.1.

$\frac{\partial u_i}{\partial x_i} = i\omega s_i A \exp[i\omega(s_x x + s_z z - t)]d_{x_i}$. and

$\frac{\partial u_i}{\partial x_j} = i\omega s_j A \exp[i\omega(s_x x + s_z z - t)]d_{x_i}$

As the incidence point is assumed the origin of coordinates. $i\omega\exp[i\omega(s_x x + s_z z - t)]$ is a common factor. then the equations C.5 become.

$$\sum \tau_{xz} = \mu\{[(s_z d_x + s_x d_z)A]_{PI} + [(s_z d_x + s_x d_z)A]_{PR} + [(s_z d_x + s_x d_z)A]_{SR}\}=0 \qquad \text{(C.6.a)}$$

$$\sum \tau_{zz} = \lambda\{[(s_x d_x + s_z d_z)A]_{PI} + [(s_x d_x + s_z d_z)A]_{PR} + [(s_x d_x + s_z d_z)A]_{SR}\}$$

$$+ 2\mu\{[s_z d_z A]_{PI} + [s_z d_z A]_{PR} + [s_z d_z A]_{SR}\} = 0 \qquad \text{(C.6.b)}$$

In isotropic homogeneous elastic waves

$$V_S = \sqrt{\frac{\mu}{\rho}} \text{ and } V_P = \sqrt{\frac{\lambda + 2\mu}{\rho}} \text{. then } \mu = V_S^{\,2}\rho \text{ and } \lambda = V_P^{\,2}\rho - 2V_S^{\,2}\rho \text{ .} \qquad \text{(C.7)}$$

From the ray parameter (Eq. C.2), the following identities for *P* waves are inferred:

$$\sin\theta = pV_P . \qquad \text{(C.8)}$$

$$\cos^2\theta = 1-(pV_P)^2 .$$

$$\cos\theta = \left(1-(pV_P)^2\right)^{1/2} .$$

Equivalently for *S* waves:

$$\sin\phi = pV_S . \qquad \text{(C.9)}$$

$$\cos^2\phi = 1-(pV_S)^2 .$$

$$\cos\phi = \left(1-(pV_S)^2\right)^{1/2} .$$

From Table C.1, equations C.6 becomes

$$\sum\tau_{xz} = \mu\left(\left(2\frac{\sin\theta}{V_P}\cos\theta\right)(A_{PR}-A_{PI})+\left(\frac{\cos^2\phi-\sin^2\phi}{V_S}\right)A_{SR}\right) = 0 . \text{(C.10.a)}$$

and

$$\sum\tau_{zz} = \left(\frac{\lambda+2\mu\cos^2\theta}{V_P}\right)(A_{PR}+A_{PI})-2\mu\frac{\sin\phi}{V_S}\cos\phi A_{SR} = 0 . \qquad \text{(C.10.b)}$$

or equivalently, using equations C.7, C.8 and C.9,

$$\sum\tau_{xz} = 2V_S^2\rho p\cos\theta(A_{PR}-A_{PI})+V_S\rho(1-2p^2V_S^2)A_{SR} = 0 \qquad \text{(C.11.a)}$$

$$\sum\tau_{zz} = \rho V_P(1-2V_S^2p)(A_{PR}+A_{PI})-2\rho V_S^2pA_{SR}\cos\phi = 0 \qquad \text{(C.11.b).}$$

which is the form presented by Krebes (1989).

From the Condition 1 (displacements), equation C.3.a, the ratio between each component amplitude and the incident *P*-wave amplitude are

$$\frac{u_z}{u_{IP}} = (-\cos\theta) + \frac{u_{RP}}{u_{IP}}\cos\theta + \frac{u_{RS}}{u_{IP}}(-\sin\phi) \qquad \text{(C.12.a)}$$

$$\frac{u_x}{u_{IP}} = \sin\theta + \frac{u_{RP}}{u_{IP}}\sin\theta + \frac{u_{RS}}{u_{IP}}\cos\phi \qquad \text{(C.12.b)}$$

The ratios $\frac{u_{RP}}{u_{IP}}$ and $\frac{u_{RS}}{u_{IP}}$ can be expressed as $\frac{A_{RP}}{A_{IP}}$ and $\frac{A_{RS}}{A_{IP}}$, and calculated from Eqtns. C.10.a and C.10.b:

$$\frac{A_{RP}}{A_{IP}} = \frac{4\mu\sin\theta\cos\theta\sin\phi\cos\phi - (2\cos^2\phi - 1)(\lambda + 2\mu\cos^2\theta)}{4\mu\sin\theta\cos\theta\sin\phi\cos\phi + (2\cos^2\phi - 1)(\lambda + 2\mu\cos^2\theta)} \qquad \text{(C.13.a)}$$

and

$$\frac{A_{RS}}{A_{IP}} = 4\frac{V_S}{V_P}\frac{\sin\theta\cos\theta(\lambda + 2\mu\cos^2\theta)}{4\mu\sin\theta\cos\theta\sin\phi\cos\phi + (2\cos^2\phi - 1)(\lambda + 2\mu\cos^2\theta)} \qquad \text{(C.13.b)}$$

Replacing C.13.a and C.13b in C.12a and C.12.b.

$$R_P^v \equiv \frac{u_z}{u_P} = \frac{\left(\lambda + 2\mu\cos^2\theta\right)\left(-2\cos\theta\left(2\cos^2\phi - 1\right) - 4\left(\frac{V_S}{V_P}\right)\sin\theta\cos\theta\sin\phi\right)}{4\mu\sin\theta\cos\theta\cos\phi + \left(2\cos^2\phi - 1\right)\left(\lambda + 2\mu\cos^2\theta\right)}$$

$$R_P^h \equiv \frac{u_x}{u_P} = \frac{4\sin\theta\cos\theta\cos\phi\left(2\mu\sin\theta\sin\phi + \left(\frac{V_S}{V_P}\right)\left(\lambda + 2\mu\cos^2\theta\right)\right)}{4\mu\sin\theta\cos\theta\cos\phi + \left(2\cos^2\phi - 1\right)\left(\lambda + 2\mu\cos^2\theta\right)}$$

and using Equations C.7. C.8 and C.9 the next relations. result

$$R_P^v \equiv \frac{u_z}{u_P} = \frac{2\left(\frac{V_P}{V_S}\right)\left(\left(\frac{V_S}{V_P}\right)^2 - V_S^2 p^2\right)^{1/2}\left(2V_S^2 p^2 - 1\right)}{\left(1 - 2V_S^2 p^2\right)^2 + 4p^2 V_S^2 \cdot \left(\left(\frac{V_S}{V_P}\right)^2 - V_S^2 p^2\right)^{1/2} \cdot \left(1 - V_S^2 p^2\right)^{1/2}} \qquad \text{(C.14.a)}$$

and

$$R_P^h \equiv \frac{u_x}{u_P} = \frac{4V_P \cdot p \cdot \left(\left(V_S / V_P\right)^2 - V_S^2 p^2\right)^{1/2} \left(1 - V_S^2 p^2\right)^{1/2}}{\left(1 - 2V_S^2 p^2\right)^2 + 4p^2 V_S^2 \cdot \left(\left(V_S / V_P\right)^2 - V_S^2 p^2\right)^{1/2} \cdot \left(1 - V_S^2 p^2\right)^{1/2}} \qquad \text{(C.14.b)}$$

which are the expressions presented by Dankbaar (1985).

Case 2: Incident *S* wave

A similar derivation can be performed for incident S wave. from the condition 1 (displacements).

$$u_z = u_{IS} \sin\phi + u_{RP} \cos\theta + u_{RS}(-\sin\phi)$$

and

$$u_x = u_{IS} \cos\phi + u_{RP} \sin\theta + u_{RS} \cos\phi$$

and from the condition 2 (stresses):

$$\sum \tau_{xz} = \mu\left\{\left[(s_z d_x + s_x d_z)A\right]_{SI} + \left[(s_z d_x + s_x d_z)A\right]_{PR} + \left[(s_z d_x + s_x d_z)A\right]_{SR}\right\}$$

$$\sum \tau_{zz} = \lambda\left\{\left[(s_x d_x + s_z d_z)A\right]_{SI} + \left[(s_x d_x + s_z d_z)A\right]_{PR} + \left[(s_x d_x + s_z d_z)A\right]_{SR}\right\}$$

$$+ 2\mu\left\{\left[s_z d_z A\right]_{SI} + \left[s_z d_z A\right]_{PR} + \left[s_z d_z A\right]_{SR}\right\} = 0$$

resulting in the expressions presented by Dankbaar, 1985:

$$R_S^v \equiv \frac{u_z}{u_S} = \frac{4V_S p \left(\left(V_S / V_P\right)^2 - V_S^2 p^2\right)^{1/2} \left(1 - V_S^2 p^2\right)^{1/2}}{\left(1 - 2V_S^2 p^2\right)^2 + 4p^2 V_S^2 \cdot \left(\left(V_S / V_P\right)^2 - V_S^2 p^2\right)^{1/2} \cdot \left(1 - V_S^2 p^2\right)^{1/2}} \qquad \text{(C.15.a)}$$

and

$$R_S^h \equiv \frac{u_x}{u_S} = \frac{2 \cdot \left(1 - V_S{}^2 p^2\right)^{\frac{1}{2}} \cdot \left(1 - 2V_S{}^2 p^2\right)}{\left(1 - 2V_S{}^2 p^2\right)^2 + 4p^2 V_S{}^2 \cdot \left(\left(\frac{V_S}{V_P}\right)^2 - V_S{}^2 p^2\right)^{\frac{1}{2}} \cdot \left(1 - V_S{}^2 p^2\right)^{\frac{1}{2}}} \quad \text{(C.15.b)}$$